

NOTE TO USERS

The original manuscript received by UMI contains pages with slanted print. Pages were microfilmed as received.

This reproduction is the best copy available

UMI

**A THERMODYNAMIC ANALYSIS OF EVAPORATION WAVES
IN AN EXPANDING JET**

by

Warren Heino Vesik

A thesis submitted in conformity with the requirements
for the degree of Master of Applied Science
Graduate Department of Mechanical and Industrial Engineering
University of Toronto

© Copyright by Warren Heino Vesik, 1997.



National Library
of Canada

Acquisitions and
Bibliographic Services

395 Wellington Street
Ottawa ON K1A 0N4
Canada

Bibliothèque nationale
du Canada

Acquisitions et
services bibliographiques

395, rue Wellington
Ottawa ON K1A 0N4
Canada

Your file Votre référence

Our file Notre référence

The author has granted a non-exclusive licence allowing the National Library of Canada to reproduce, loan, distribute or sell copies of this thesis in microform, paper or electronic formats.

The author retains ownership of the copyright in this thesis. Neither the thesis nor substantial extracts from it may be printed or otherwise reproduced without the author's permission.

L'auteur a accordé une licence non exclusive permettant à la Bibliothèque nationale du Canada de reproduire, prêter, distribuer ou vendre des copies de cette thèse sous la forme de microfiche/film, de reproduction sur papier ou sur format électronique.

L'auteur conserve la propriété du droit d'auteur qui protège cette thèse. Ni la thèse ni des extraits substantiels de celle-ci ne doivent être imprimés ou autrement reproduits sans son autorisation.

0-612-29435-8

Abstract

A THERMODYNAMIC ANALYSIS OF EVAPORATION WAVES IN AN EXPANDING JET

by

Warren Heino Vesik

Master of Applied Science
Graduate Department of Mechanical and Industrial Engineering
University of Toronto 1997

In this work, a thermodynamic analysis of flashing evaporation waves was performed. Specifically, the analysis focused on the expansion of dodecane through a converging nozzle. Properties of the fluid were calculated using the modified Simonet-Behar-Rauzy equation of state. The flow model consisted of an isentropic expansion to a superheated liquid state, followed by evaporation across a cylindrical discontinuity. Sonic and subsonic flow conditions were alternately considered for the downstream, equilibrium state of the discontinuity. The outward flow from the discontinuity was modeled as radial and isentropic. In the sonic case, the model predicts overexpansion of the fluid to a normal shock wave and subsequent stagnation to the injection chamber pressure. Simple stagnation was proposed for the subsonic case. Model predictions for the mass flow rate, extent of evaporation across the discontinuity and shock location are compared to experimental evidence.

Acknowledgments

I would like to express my gratitude to Professor Susan McCahan for her helpful advice and direction regarding my thesis work. I would also like to thank my family for their support throughout my studies.

Table of Contents

ABSTRACT.....	ii
ACKNOWLEDGMENTS	iii
TABLE OF CONTENTS.....	iv
LIST OF TABLES.....	vi
LIST OF FIGURES	vii
LIST OF APPENDICES.....	x
NOMENCLATURE	xi
1. INTRODUCTION	1
1.1. CONTEXT AND OBJECTIVES	1
2. THEORY	4
2.1. NUCLEATION AND METASTABLE STATES	4
2.2. HYDROCARBON EQUATIONS OF STATE.....	9
2.2.1. Method of Comparison	10
2.2.2. The Equations of State	13
2.2.3. Comparison Results	25
2.2.4. Discussion and Equation Selection.....	31
2.3. RESIDUAL PROPERTIES OF THE MSBR EQUATION OF STATE	33
2.4. RETROGRADE FLUIDS	38
3. EVAPORATION WAVES.....	44
3.1. PREVIOUS OBSERVATIONS OF EVAPORATION WAVES	44
3.1.1. Internal Flows	44
3.1.2. External Flows	48
3.2. BASIS OF PRESENT ANALYSIS.....	50
3.2.1. Overview of Experimental Conditions and Apparatus	50
3.2.2. Instrumentation	51
3.2.3. Experimental Procedure.....	52
3.2.4. Experimental Results	52

3.3. FLOW MODEL	56
3.3.1. Nozzle Flow	56
3.3.2. Evaporation Discontinuity	57
3.3.3. External Flow	63
3.3.4. Comments on Computational Procedure	72
4. RESULTS	73
4.1. SOLUTION DOMAIN	73
4.2. MODEL OF EXPERIMENTAL INJECTIONS.....	80
5. DISCUSSION	87
5.1. MODEL COMPARISON WITH EXPERIMENT	87
5.1.1. Mass Flow Rate Comparison.....	87
5.1.2. Qualitative Comparison	88
5.2. EVAPORATION DISCONTINUITY STRUCTURE.....	94
5.2.1. Growing Bubble Layer	96
5.2.2. Single Interface	99
6. CONCLUSIONS.....	102
6.1. SUMMARY.....	102
6.2. RECOMMENDATIONS FOR FUTURE WORK.....	105
REFERENCES	107
APPENDIX A: DATA FROM FLOW MODEL COMPUTATIONS	111

List of Tables

Table 2.1. SPHCT equation of state parameters for dodecane	24
Table A.1. Subsonic solutions for (1) states lying between points h and i on the isentrope shown in Figure A.1	112
Table A.2. CJ solutions for (1) states lying between points i and g on the isentrope shown in Figure A.1	114
Table A.3. Subsonic solutions for (1) states lying at the points c , d , e and f in Figure A.1	117
Table A.4. CJ solutions for (1) states lying along the curve jk shown in Figure A.1	118

List of Figures

Figure 2.1. Pressure-volume diagram of a pure substance showing metastable regions. Properties are normalized by their critical point values, v_c and P_c	9
Figure 2.2. Thermodynamic properties of dodecane calculated with the Starling-Han equation of state	17
Figure 2.3. Thermodynamic properties of dodecane calculated with the Lee-Kesler equation of state.....	17
Figure 2.4. Thermodynamic properties of dodecane calculated with the Twu-Coon-Cunningham equation of state	20
Figure 2.5. Thermodynamic properties of dodecane calculated with the Modified Kumar-Starling equation of state	20
Figure 2.6. Thermodynamic properties of dodecane calculated with the Simonet-Behar-Rauzy equation of state	23
Figure 2.7. Thermodynamic properties of dodecane calculated with the modified Simonet-Behar-Rauzy equation of state	23
Figure 2.8. Thermodynamic properties of dodecane calculated with the Simplified Perturbed Hard Chain Theory equation of state.....	26
Figure 2.9. Thermodynamic properties of dodecane calculated with the modified Benedict-Webb-Rubin equation of state	26
Figure 2.10. Comparison of equation of state spinodals with the kinetic limit of superheat obtained from homogeneous nucleation theory.....	28
Figure 2.11. Equation of state saturation pressure error with respect to the Frost-Kalkwarf-Thodos correlation.....	29
Figure 2.12. Equation of state saturated liquid volume error with respect to the Hankinson-Thomson correlation	30
Figure 2.13. Sample equilibrium isentrope and extensions of single phase branches into metastable regions in the pressure-volume plane.....	39
Figure 2.14. Speed of sound as a function of pressure along the equilibrium isentrope shown in Figure 2.13	39

Figure 2.15. Isentropic processes leading to condensation for (a) a regular fluid and (b) a retrograde fluid, in the normalized temperature-entropy plane	40
Figure 2.16. Schematic of a diaphragm burst experiment	43
Figure 3.1. Dimensions of the conical converging nozzle.....	51
Figure 3.2. Injection of dodecane at 311°C ($0.89T_c$)	54
Figure 3.3. (a) Photographic enlargement of the nozzle exit region for an injection temperature of 311°C. (b) Cross-sectional schematic of the flow structure, including the nozzle interior	55
Figure 3.4. Temperature dependence of liquid core length for dodecane injections exhibiting an evaporation discontinuity.....	56
Figure 3.5. Control surface enclosing the evaporation discontinuity	58
Figure 3.6. Thermodynamic model for an evaporation discontinuity. Properties jump from a metastable liquid state (1) to a state (2) on the equilibrium Hugoniot. State (2a): zero velocity, weak deflagration; state (2c): subsonic velocity, weak deflagration; state (2b): sonic velocity, CJ deflagration; state (2d): supersonic velocity, strong deflagration. The process from (0) to (1) represents the isentropic expansion through the nozzle.	62
Figure 3.7. Model for subsonic flow downstream of the evaporation discontinuity	69
Figure 3.8. Thermodynamic states corresponding to the subsonic flow model shown in Figure 3.7.....	69
Figure 3.9. Model for sonic flow at point (2), the downstream state of the evaporation discontinuity.....	71
Figure 3.10. Thermodynamic states corresponding to the CJ flow model shown in Figure 3.9	71
Figure 4.1. Domain of possible (1) states achievable by isentropic expansion from the experimental (0) states. Region <i>abdc</i> : state (1) yields a CJ solution. Region <i>cdfe</i> : state (1) yields a subsonic solution	74
Figure 4.2. Subsonic solutions for points on the isentrope <i>gh</i> shown in Figure 4.1	76

Figure 4.3. Evaporation wave speeds corresponding to the subsonic solutions plotted in Figure 4.2.....	76
Figure 4.4. CJ solutions for points on the isentrope gh shown in Figure 4.1	77
Figure 4.5. Evaporation wave speeds corresponding to the CJ solutions plotted in Figure 4.4	77
Figure 4.6. Non-dimensionalized shock radius as a function of state (1) pressure for the CJ solutions of Figure 4.4.....	79
Figure 4.7. Dependence of Jakob number on injection temperature along the cutoff isobar cd of Figure 4.1	80
Figure 4.8. Experimental mass flow rates at various injection temperatures compared with those calculated by equation (4.4).....	83
Figure 4.9. Calculation of state (1) as a function of injection temperature, using equation (4.3)	85
Figure 4.10. CJ solutions corresponding to the experimental injections	85
Figure 4.11. Non-dimensionalized shock locations for the CJ solutions plotted in Figure 4.10	86
Figure 5.1. Comparison of mass flow rates predicted by the discontinuity model with experimental values at each injection temperature	89
Figure 5.2. Possible interpretations of the evaporation wave structure observed in diaphragm burst experiments.....	95
Figure A.1. Domain of possible (1) states achievable by isentropic expansion from the experimental (0) states. Region $abdc$: state (1) yields a CJ solution. Region $cdfe$: state (1) yields a subsonic solution. Curve jk : (1) states calculated using equation (4.3) and the experimental mass flow rates	111

List of Appendices

Appendix A: Data from flow model computations.....	111
--	-----

Nomenclature

A	surface area
c	speed of sound
c_p	specific heat at constant pressure
c_v	specific heat at constant volume
\tilde{c}_v	non-dimensionalized ideal gas specific heat at constant volume
d	nozzle exit diameter
f	fugacity
h	specific enthalpy
i	mass flux
j	number of homogeneous nucleation events per molecular collision
J	rate of formation of homogeneous nuclei per unit volume
Ja	Jakob number
k_B	Boltzmann constant
l	evaporation discontinuity length
m	mass of one molecule
\dot{m}	mass flow rate
Ma	Mach number
N_l	number of liquid molecules per unit volume
P	pressure of the bulk fluid
R	ideal gas constant

r	radial position
s	specific entropy
T	temperature of the bulk fluid
u	fluid velocity
v	specific volume
w	acentric factor, maximum width of evaporation discontinuity
W_{cr}	critical work of nucleation
x	quality
Z	compressibility

Symbols

Π	superheat, pressure definition
ρ	density
σ	surface tension
ϕ	heterogeneous nucleation factor
Φ	Helmholtz energy
μ	chemical potential
ΔT	superheat, temperature definition
Γ	fundamental derivative

Subscripts

c	critical property
exp	experimental value
l	liquid

<i>lv</i>	difference between liquid and vapour saturation properties
<i>ml</i>	metastable liquid
<i>n</i>	normal component
<i>r</i>	reduced property
<i>sat</i>	saturation property
<i>sp</i>	spinodal property
<i>t</i>	tangential component
<i>v</i>	vapour

Superscripts

0	ideal gas property
<i>R</i>	residual property

1. INTRODUCTION

1.1. Context and Objectives

When a liquid is at a temperature which is above the boiling temperature at the ambient pressure, it is said to be superheated. Virtually all phase changes from liquid to vapour involve some degree of superheating, however small, of some portion of the liquid phase. In many applications, evaporation is achieved through local superheating of a liquid by heat transfer through the walls of a containment structure. However, it is possible to conceive of processes by which a fluid can undergo vapourization adiabatically, i.e. with negligible heat transfer from the surroundings. For instance, the rapid depressurization of a saturated liquid can lead to significant superheating and the sudden production of tiny, growing vapour bubbles. Depending on the extent to which the liquid has departed from equilibrium, the evaporation can progress in a rapid and potentially explosive manner.

This rapid or “flash” evaporation is a phenomenon which can be hazardous in some situations. The loss of coolant accident, or “LOCA” as it is abbreviated, has been studied extensively in nuclear power plant safety analyses. In this scenario, hot water under pressure in cooling lines is suddenly exposed to the atmosphere through a pipe or valve failure. The pressure drop results in superheating and subsequent flashing of the water which forces a two-phase flow violently through the rupture. Similar problems can occur in liquefied gas pipelines or chemical reactors.

Another dangerous scenario resulting from liquid superheating is the boiling-liquid, expanding-vapour explosion (BLEVE). In these incidents, a fire surrounding a liquid-filled container causes the liquid to boil and the internal pressure of the container rises. Although most vessels carrying liquefied gases have relief valves which activate once a certain pressure is reached, they are frequently unable to vent vapour fast enough to reduce the internal pressure. As a result, the container bursts and the remaining liquid boils explosively. If the fluid is flammable, the release may be ignited, causing a fireball (Prugh [1991]).

On the other hand, rapid evaporation can also be exploited in a beneficial manner. An automotive port fuel injector releases pressurized liquid fuel into the intake port in a short duration pulse, usually through a pintle-type nozzle. The liquid jet atomizes into droplets which evaporate in the surrounding air during the intake and compression processes. However, at least some of the injected fuel impacts on the port walls and the back of the intake valve, forming a liquid film which may flow into the cylinder and escape combustion. Both fuel efficiency and exhaust emissions are affected negatively. Pre-heating the fuel prior to its injection so that it becomes superheated has been shown to produce a more finely atomized spray (see, for example, Senda et al. [1994]). This increases the overall evaporation rate in proportion to the increase in evaporative surface area and serves to reduce wasted fuel. Enhanced atomization, faster fuel-air mixing and reduced spray penetration are also cited by Oza and Sinnamon [1983] as advantages of flashing injection in direct-injection diesel engines. These are important benefits because direct-injection engines require careful combustion chamber and injector design to attain sufficiently rapid mixing at high speeds.

Experiments have recently been conducted by Sloss [1996] to study the use of flashing injection as a means of improving the operation of domestic oil furnace burners. As in automotive fuel injectors, it is necessary to break up the fuel jetting from the burners into very fine droplets to augment the evaporation rate. By doing so, fewer droplets are likely to escape complete combustion, which in turn reduces the emissions of pollutants such as unburned hydrocarbons and soot and increases the furnace efficiency. In these experiments, a pure substance, dodecane, and various heavy fuel mixtures were pressurized to 10 bar, uniformly heated, and then injected through a small nozzle into a chamber at atmospheric pressure. Depending on the temperature to which the fuel was pre-heated and the type of nozzle used, different flow patterns were observed in the injection chamber. For injections of dodecane through a conical, converging nozzle at the highest temperatures achieved in the study (above 303°C), the evaporation of the fuel was found to occur along a single, conical front having its base at the nozzle exit. Downstream of this standing “evaporation wave”, the photographic evidence revealed a finely dispersed two-phase flow, the liquid fraction of which evaporated completely within a distance of a few times the nozzle exit diameter.

The objective of the present work is to model this evaporative interface and overall flow to ascertain the thermodynamic states attained by the fluid expanding outward into the injection chamber. As part of this study, a review of published hydrocarbon equations of state was undertaken to choose a suitable expression to represent the thermodynamic properties of dodecane. Various theories which have been advanced on the structure and mechanisms of the evaporation wave are also discussed.

2. THEORY

2.1. Nucleation and Metastable States

Classically, phase transitions between the liquid and vapour states of a pure substance take place under equilibrium conditions. In the absence of interfacial effects, both phases have essentially the same temperature T , pressure P , and chemical potential μ during the process. For a given pressure, there is only one particular temperature for which the two phases can co-exist in equilibrium. Therefore, a functional relation $P_{sat}=P_{sat}(T_{sat})$, or alternatively $T_{sat}=T_{sat}(P_{sat})$ can be defined for a given substance, where the subscript sat indicates a saturated or two-phase equilibrium state. This functional relation combined with the volumetric properties of the liquid and vapour phases establishes a saturation boundary in the pressure-volume plane of a pure substance. For an equilibrium phase transition, once a liquid has reached its saturation temperature, energy addition to the fluid at constant pressure results only in vapourization and the temperature remains constant. Similarly, energy removed from a saturated vapour results in condensation.

However, most liquid-vapour phase transitions actually occur under non-equilibrium conditions. For example, a liquid can be heated at constant pressure to a temperature in excess of its saturation temperature, or it may be expanded isothermally below its saturation pressure without vapourization immediately occurring. The state the liquid attains through these processes is metastable, meaning that it exists for a finite time before phase change

allows the fluid to relax to equilibrium. The mechanism by which the vapourization process is initiated from a metastable (i.e. superheated) liquid state is termed nucleation.

When a liquid achieves a metastable thermodynamic state, it is subject to random, localized density fluctuations that may be sufficient to produce small nuclei having a molecular density approximately equal to that of saturated vapour. By examining the change in the availability function associated with the formation of a bubble nucleus in superheated liquid, it can be shown that if such a nucleus exceeds a certain critical size, it will spontaneously grow to form a vapour bubble in the bulk liquid phase. This process is called homogeneous nucleation. In a given volume of fluid, nuclei of critical size are formed more frequently as the liquid departs from equilibrium. This gives rise to the concept of a homogeneous nucleation rate, J , having units of critical nuclei per unit volume per unit time. Assuming that the vapour phase can be described as an ideal gas, the steady-state rate of generation of critical size bubbles can be written as a function of the thermodynamic state of the liquid phase, and the liquid-vapour interfacial tension (Carey, [1992]).

$$J = N_l \left(\frac{3\sigma}{\pi m} \right)^{1/2} \exp \left\{ \frac{-W_{cr}}{k_B T_l} \right\} \quad (2.1a)$$

$$W_{cr} = \frac{16\pi\sigma^3}{3 \left[P_{sat}(T_l) \exp \left\{ \frac{v_l [P_l - P_{sat}(T_l)]}{RT_l} \right\} - P_l \right]^2} \quad (2.1b)$$

In these expressions, N_l is the number of liquid molecules per unit volume, σ is the liquid-vapour interfacial tension, m is the mass of a single molecule, k_B is the Boltzmann constant, and R is the ideal gas constant. P_l and T_l are the pressure and temperature of the superheated

liquid, and v_l is the saturated specific liquid volume corresponding to T_l . W_{cr} represents the work required to produce a bubble of critical size.

Equations (2.1a) and (2.1b) represent the rate at which nuclei form homogeneously in bulk superheated liquid. In many cases, however, nucleation occurs preferentially at available interfaces between the liquid and a solid surface, as can be seen clearly in a pot of water simmering on a stove. This *heterogeneous* nucleation results from a reduction in the work necessary to produce a critical nucleus due to the geometry of the solid surface. Various expressions for heterogeneous nucleation rates can be derived which are analogous to (2.1) for different idealized surface cavity shapes (Cole [1974]). The analysis is further complicated by the fact that nucleation is often facilitated by gas or vapour entrapped in the cavities. An alternative approach to determining an equation for the heterogeneous nucleation rate is to multiply the critical work of equation (2.1a) by a so-called heterogeneous nucleation factor, ϕ , where $0 < \phi < 1$. This factor has been correlated by conducting fast depressurization experiments, mainly with water (Alamgir and Lienhard [1981], Deligiannis and Cleaver [1992]). Such an approach has the advantage that it works around the difficulty of describing the infinite variety of cavity geometries present on a given solid surface by averaging their combined effect. However, the usefulness of this technique is limited by the functional dependence of ϕ on the depressurization rate, surface material and surface preparation method.

As mentioned previously, the nucleation rate increases as a metastable liquid moves farther from equilibrium. Two commonly used measures of superheat quantify the extent to which the liquid has deviated from a reference, saturation property. One is the pressure

definition of superheat. Π , a dimensionless number based on the difference between the bulk liquid pressure, P_l , and the saturation pressure corresponding to the bulk liquid temperature, T_l .

$$\Pi = \frac{P_{sat}(T_l) - P_l}{P_{sat}(T_l)} \quad (2.2)$$

Alternatively, it is possible to come up with a similar parameter based on a temperature difference, ΔT :

$$\Delta T = T_l - T_{sat}(P_l) \quad (2.3)$$

A third measure of superheat is the Jakob number, Ja :

$$Ja = \frac{h_{ml} - h_l}{h_{lv}} \quad (2.4)$$

Here h_{ml} , h_l and h_{lv} are the metastable liquid enthalpy, saturated liquid enthalpy and heat of vapourization of the fluid, all evaluated at the bulk liquid pressure. For a given mass of liquid, $Ja \geq 1$ represents metastable states which have enough stored energy to effect a complete isobaric phase transition adiabatically. When $Ja < 1$, it is easy to show that equation (2.4) is equivalent to the mass fraction of liquid which can evaporate before an equilibrium state is reached.

Each of the measures of superheat has a value of zero for a state at the saturation boundary. There are also theoretical maximum values of each measure which are reached at the limit of mechanical stability for the liquid phase. This is the point at which

$$\left(\frac{\partial P}{\partial v} \right)_T = 0 \quad (2.5)$$

The pressure and volume at which this condition is satisfied depends on the temperature of the fluid, and therefore equation (2.5) represents a curve in the P - v plane. On the liquid side, this curve is called the liquid spinodal. Along with the saturated liquid line, it bounds the metastable liquid region (Figure 2.1). A similar curve called the vapour spinodal bounds a region of metastable (i.e. supercooled) vapour. The two spinodals and the saturation boundary converge at the critical point for the fluid, above which there is no phase distinction.

The liquid spinodal is not a physically realizable state because there is no process that has a sufficiently short time scale to bring the liquid to the spinodal without inducing the molecular fluctuations that lead to homogeneous nucleation. In other words, the nucleation rate at the spinodal is infinite. It is interesting to note that the homogeneous nucleation theory does not in itself predict a spinodal according to this criterion, since the value of J calculated by equations (2.1a) and (2.1b) will always be a finite number for temperatures up to the critical temperature. Instead, the nucleation rate expression is used to define the somewhat arbitrary concept known as the kinetic limit of superheat. Essentially, a threshold value of J is chosen and equations (2.1a) and (2.1b) are solved iteratively to obtain the limiting superheat temperature above which nucleation will occur almost instantaneously at a given liquid pressure, P_l . However, if a theoretical liquid spinodal is desired, it is necessary to have an equation of state which expresses a relation between the pressure, volume and temperature of the fluid of interest, ideally of the form $P=P(T,v)$. Then equation (2.5) may be used to locate the spinodal states. Lienhard and Karimi [1981] have demonstrated analytically that the kinetic and thermodynamic limits of superheat lie very close together.

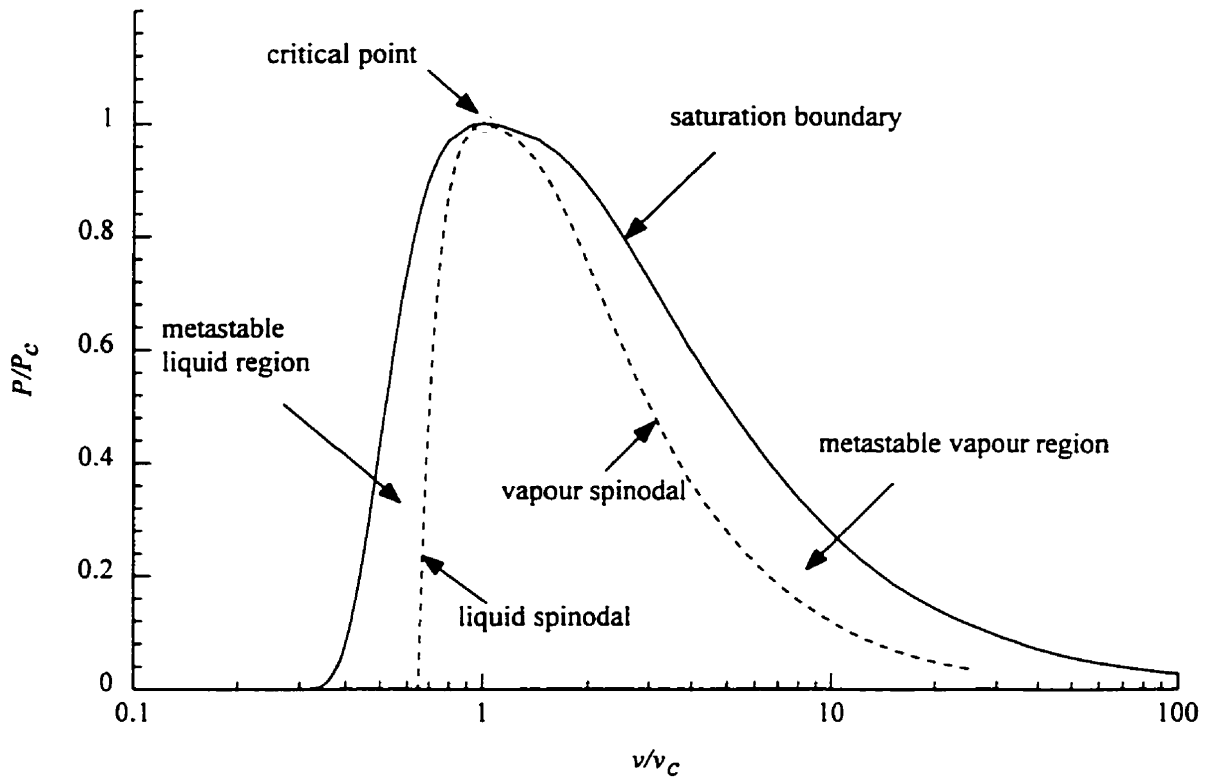


Figure 2.1. Pressure-volume diagram of a pure substance showing metastable regions. Properties are normalized by their critical point values, v_c and P_c .

Therefore it is possible to use the kinetic limit of superheat to test the accuracy of equations of state in the metastable liquid region, as will be shown in a later section.

2.2. Hydrocarbon Equations of State

In order to model the nozzle expansion and evaporation processes which are central to this work, it is necessary to have accurate thermodynamic property data of the fluid of interest. Therefore, a survey of various equations of state for hydrocarbons was undertaken to determine which would best describe dodecane, the fluid in which evaporation waves were

observed in the high temperature injections performed by Sloss [1996]. In total, eight equations of state were examined: the Starling-Han (SH) EOS (Starling et al. [1979]), the Lee-Kesler (LK) EOS [1975], the Twu-Coon-Cunningham (TCC) EOS [1995], a modified Kumar-Starling (MKS) EOS (Chu et al. [1992]), the Simonet-Behar-Rauzy (SBR) EOS (Behar et al., [1985]) and a modification (MSBR) of it (Jullian et al. [1989]), the Simplified Perturbed Hard Chain Theory (SPHCT) EOS (Shaver et al. [1995]), and lastly a modified Benedict-Webb-Rubin (MBWR) EOS (Soave, [1995]).

2.2.1. Method of Comparison

Equilibrium Properties

Each equation's suitability for predicting equilibrium states was evaluated both quantitatively and qualitatively. The quantitative evaluation was twofold. Values for the saturation vapour pressure P_{sat} calculated from the EOS as a function of temperature were compared with values obtained by the Frost-Kalkwarf-Thodos (FKT) equation

$$\ln P_{sat} = A - \frac{B}{T} + C \ln T + \frac{DP_{sat}}{T^2} \quad (2.6)$$

using the constants A , B , C and D as quoted in Reid, Prausnitz and Poling [1987]. In all cases but the Lee-Kesler equation, Maxwell's equal areas construction was used to calculate vapour-liquid equilibria. This ensures the equivalence of the chemical potentials of the phases by requiring a line of constant pressure at saturation to define two enclosed equal areas where it intersects the S-shaped isotherm for the corresponding saturation temperature.

Secondly, values for the saturated liquid volume (v_l) as a function of temperature obtained using the EOS were compared with the Hankinson-Thomson correlation

$$\frac{v_l}{v^*} = v^{(\gamma)} [1 - w_{SRK} v^{(\delta)}] \quad (2.7a)$$

$$v^{(\gamma)} = 1 + a(1 - T_r)^{1/3} + b(1 - T_r)^{2/3} + c(1 - T_r) + d(1 - T_r)^{4/3} \quad (2.7b)$$

$$v^{(\delta)} = [e + fT_r + gT_r^2 + hT_r^3] / (T_r - 1.00001) \quad (2.7c)$$

Here T_r is the reduced temperature. The coefficients a through h , and the values of v^* and w_{SRK} are constants that were obtained for dodecane from Reid, Prausnitz and Poling [1987].

Although both comparison equations are essentially curve fits to experimental data and therefore have their own built-in inaccuracy, they are almost certainly more accurate predictors than the various equations of state due to the relative simplicity of fitting a single curve compared to the entire P - v - T surface. Equation (2.6) has an average absolute deviation of just 0.25% from the saturation pressure data quoted by Vargaftik [1975] over the temperature range 350-520 K. Below 350 K the correlation tends to break down. This is primarily due to the very low saturation pressure values (less than 1 kPa). However, as the pressure range of interest in this work is significantly above 1 kPa, the increasing inaccuracy of the correlation below 350 K is not of concern. The correlation also reproduces the accepted thermodynamic critical point of dodecane ($P_c=18.2$ bar, $T_c=658.2$ K), suggesting that it may also have excellent accuracy for temperatures above 520 K. Experimental data for the saturated liquid volumes of dodecane are extremely limited, and in most cases the published values are inferred from measurements taken at subcooled liquid states. Therefore, little can be said about the quantitative accuracy of the Hankinson-Thomson correlation as it

applies to dodecane. However, since in many cases equations of state are in fact fit to data generated by this correlation (among others), its use seems justified as a means of testing equation of state accuracy. Percentage error curves for each EOS were generated according to the formula

$$\%error = \frac{EOS - correlation}{correlation} \times 100 \quad (2.8)$$

Qualitatively, each EOS was examined to determine its applicability over various regions of P - v - T space. Flaws in the representation of the near-critical region or in the overall thermodynamic consistency of the equations were documented.

Metastable Liquid Properties

It has been demonstrated (Lienhard and Karimi [1981]) that the limit of homogeneous nucleation in a liquid and the liquid spinodal line should lie extremely close to one another when plotted on pressure-temperature coordinates. Therefore, the locus of states for which $(\partial P / \partial v)_T = 0$ as predicted by the various equations of state might be compared with the limit given by classical homogeneous nucleation theory to give some indication of the ability of each EOS to represent the metastable liquid region. Theories of homogeneous nucleation are generally of the form

$$j \frac{\text{nucleation events}}{\text{molecule - collision}} = \exp \left[- \frac{\text{critical work needed to trigger nucleation}}{k_B T_c} \right] \quad (2.9)$$

Based on an analysis of experimental data, Lienhard and Karimi suggest that a good upper bound for the steady state rate of nucleation would correspond to a value of j of 10^{-5} . Thus the value of the spinodal pressure (P_{sp}), as a function of temperature can be obtained from

$$j = 10^{-5} = \exp \left[- \frac{16\pi\sigma^3}{3k_B T_c (1 - v_l / v_v)^2 (P_{vp} - P_{sat})^2} \right] \quad (2.10)$$

where σ is the surface tension, and v_l and v_v are the saturated liquid and vapour specific volumes respectively. This formula is similar to that shown for J in equations (2.1a) and (2.1b), the differences being the units of j as opposed to those of J and certain assumptions made in arriving at the expression. Essentially, j is an expression for the nucleation rate on a molecular scale. When j is multiplied by the number of liquid molecules per unit volume and the number of molecular collisions per unit time, the result is J , the nucleation rate on a macroscopic scale.

Since there does not appear to be an accurate corresponding states correlation for the saturated vapour volume, it was decided to obtain saturation properties for use in the above equation from one of the equations of state in this study, namely the MBWR EOS. As shall be seen later, it provides excellent quantitative and qualitative results for equilibrium properties, especially at the high temperatures for which the spinodal pressure is positive. A correlation from the DIPPR data compilation of Daubert and Danner [1985] was used to obtain temperature dependent values of surface tension.

2.2.2. *The Equations of State*

Starling-Han (Starling et al. [1979])

The pressure-density-temperature (P - ρ - T) relationship commonly known as the Starling-Han EOS has the form

$$\begin{aligned}
P = \rho RT + \left(B_0 RT - A_0 - \frac{C_0}{T^2} + \frac{D_0}{T^3} - \frac{E_0}{T^4} \right) \rho^2 + \left(bRT - a - \frac{d}{T} \right) \rho^3 \\
+ \alpha \left(a + \frac{d}{T} \right) \rho^6 + c \frac{\rho^3}{T^2} (1 + \gamma \rho^2) \exp(-\gamma \rho^2)
\end{aligned}
\tag{2.11}$$

where each of the constants γ , α , B_0 through D_0 and a through d are expressed in an additional set of equations as functions of critical volume, critical temperature and an acentric factor.

Figure 2.2 is a plot of the saturation boundary, and two sample isotherms obtained from this EOS. Two things are noteworthy about this graph. First, the equation is unreliable in the near-critical region, since the saturated liquid and vapour roots converge to a point nowhere near the experimental critical point. Second, for a certain range of temperatures, four extrema exist on the isotherms instead of the expected two. This does not necessarily mean that the equation of state is invalid, because one may argue that the entire region between the first minima and last maxima is non-physical, regardless of the shape of the isotherm between these two points.

Lee-Kesler (Lee and Kesler [1975])

The Lee-Kesler method for calculating vapour-liquid equilibria uses a set of two equations of state, one for a so-called simple fluid, and one for a reference fluid (usually octane). Both equations have an identical functional form but different values for their constants. The properties of other substances are obtained by interpolating or extrapolating from these two equations using an acentric factor. The equation for the two base fluids is given by Reid, Prausnitz and Poling [1987] as:

$$\frac{Z}{Z_c} = \frac{P_r v_r}{T_r} = 1 + \frac{B}{v_r} + \frac{C}{v_r^2} + \frac{D}{v_r^5} + \frac{c_4}{T_r^3 v_r^2} \left[\beta + \frac{\gamma}{v_r^2} \right] \exp \left[-\frac{\gamma}{v_r^2} \right] \quad (2.12)$$

Here Z is the compressibility, Z_c is the critical compressibility and v_r , T_r and P_r are reduced volume, reduced temperature and reduced pressure respectively. B , C and D are functions of reduced temperature and c_4 , β and γ are constants. At the same reduced temperature and reduced pressure, the above equation is solved to obtain the reduced volumes of both base fluids, and hence their compressibilities which are designated as $Z^{(0)}$ (simple) and $Z^{(R)}$ (reference). The compressibility factor for the fluid of interest is then obtained from

$$Z = Z^{(0)} + \frac{w}{w_R} (Z^{(R)} - Z^{(0)}) \quad (2.13)$$

where w is the acentric factor and w_R is the reference fluid acentric factor. Due to the peculiar nature of the Lee-Kesler method, it is not possible to use an equal-areas technique to find the saturation properties. Therefore, it is necessary to use an alternative method in which the equality of the liquid and vapour fugacities is the determining factor. In similar fashion to the compressibility factor calculation, the fugacity to pressure ratio can be calculated for both the simple and reference fluids and used to obtain the actual fugacity to pressure ratio according to

$$\ln \frac{f}{P} = \left(\ln \frac{f}{P} \right)^{(0)} + \frac{w}{w_R} \left[\left(\ln \frac{f}{P} \right)^{(R)} - \left(\ln \frac{f}{P} \right)^{(0)} \right] \quad (2.14)$$

Figure 2.3 shows two isotherms at the same temperature (640 K), one for the simple fluid, and one for the reference fluid. It is clear that the saturation pressure for this temperature can only lie within the pressure range labeled ΔP on the figure, since only over this range do both liquid and vapour volume roots exist for each fluid. In calculating the

saturation boundary for this EOS at temperatures above 644 K, the liquid and vapour phase fugacity to pressure ratios were found to be unequal over this entire pressure range. Therefore the near-critical vapour dome cannot be calculated. This can be seen in Figure 2.3. It is also evident that it is impossible to plot a complete metastable isotherm for dodecane itself without relaxing the requirement that the reduced volumes of the simple and reference fluids be calculated at the same temperature and pressure. For example, if one begins to calculate an isotherm starting in the liquid phase and obtains points on the isotherm by decrementing the pressure, eventually the liquid spinodal of the simple fluid is reached. Decrementing the pressure further is not possible since the only volume root calculable from equation (2.12) for the simple fluid is the vapour phase value. As a result, it is not possible to calculate metastable states very far inside the saturation boundary and the location of the spinodal for dodecane cannot be predicted using the Lee-Kesler method without modification.

Twu-Coon-Cunningham (Twu et al. [1995])

This is a cubic equation of state of the form:

$$P = \frac{RT}{v - b} - \frac{a}{v(v + 4b) + c(v + b)} \quad (2.15)$$

The parameters c and b are constants, while a is a temperature dependent function. The following constraints are applied to the isotherm at temperature T_c where it passes through the critical point:

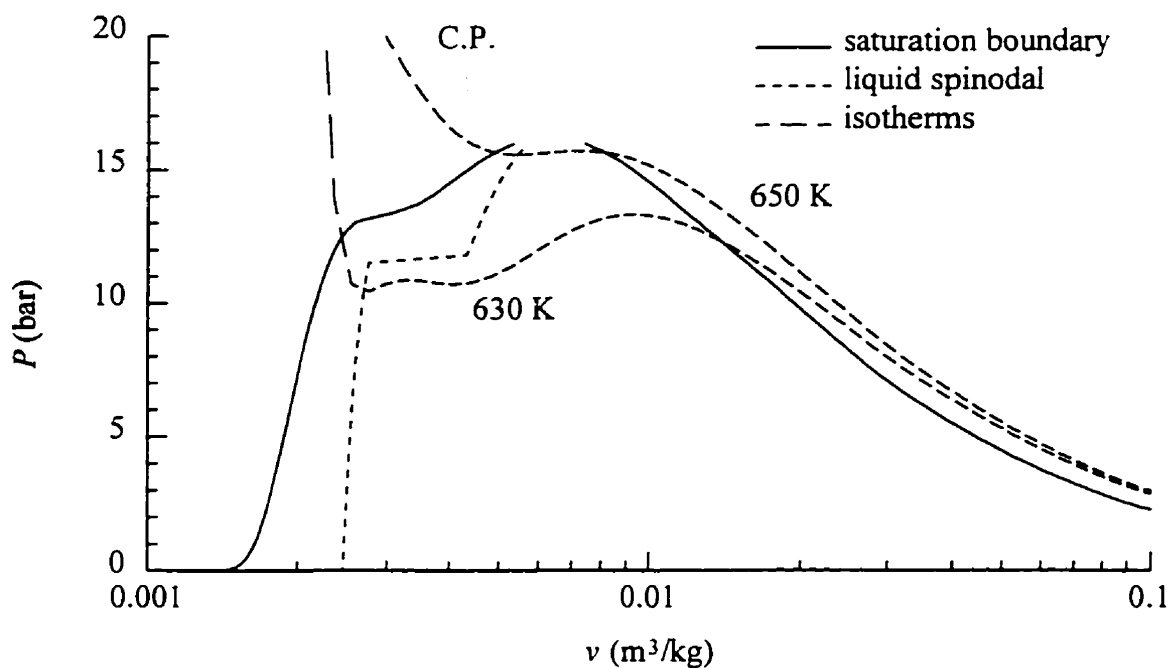


Figure 2.2. Thermodynamic properties of dodecane calculated with the Starling-Han equation of state.

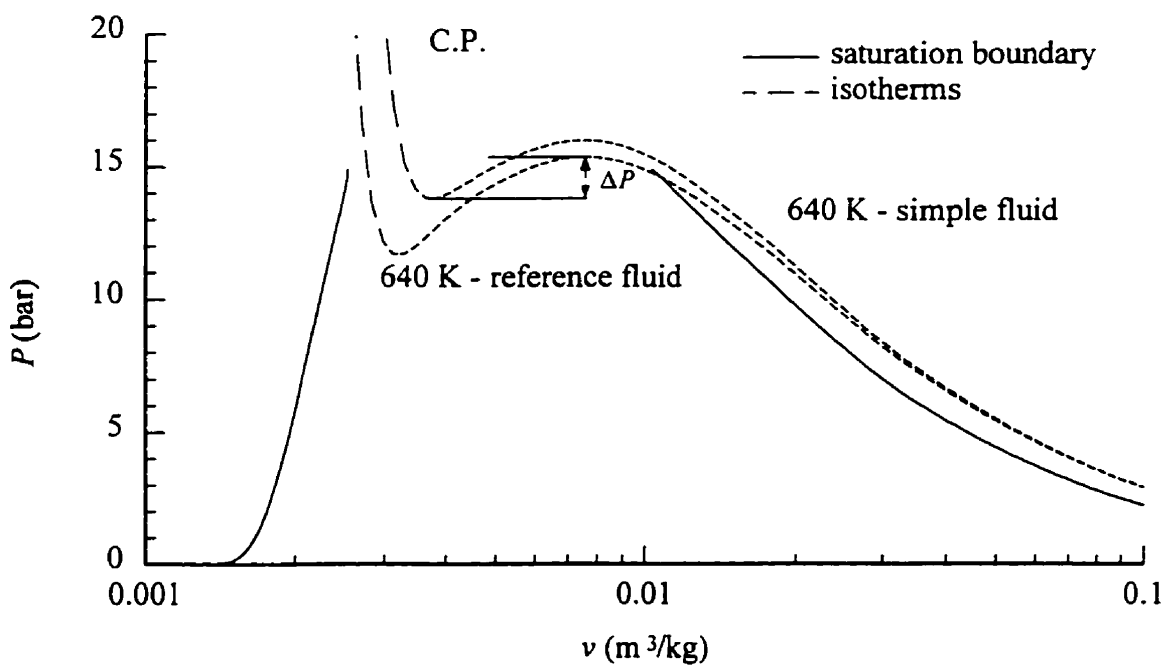


Figure 2.3. Thermodynamic properties of dodecane calculated with the Lee-Kesler equation of state.

$$\left(\frac{\partial P}{\partial v}\right)_{T_c} = 0 \quad (2.16a)$$

$$\left(\frac{\partial^2 P}{\partial v^2}\right)_{T_c} = 0 \quad (2.16b)$$

These constraints, along with a value for the critical compressibility factor that was obtained for each substance by Twu et al. [1995], can be used to obtain c , b and the critical value of a . This “apparent” critical compressibility is not the same as the experimental value but is instead a number which results from fitting the EOS. Therefore the major flaw in this equation of state is its poor prediction of liquid densities, especially near the critical point. Figure 2.4 presents the saturation boundary, sample isotherms and the liquid spinodal calculated using this equation.

Modified Kumar-Starling (Chu et al. [1992])

The modified Kumar-Starling EOS is a complex cubic equation which uses as many as thirty universal constants to describe high molecular weight hydrocarbons. It can be expressed most compactly as

$$P = \frac{RT}{v - b_1} - \frac{a}{(v + b_2)(v + b_3)} \left(1 - \frac{d}{b_1}\right) \quad (2.17)$$

where a , b_1 , b_2 and b_3 are functions of temperature and an acentric factor. In addition to the critical point constraints in equations (2.16a) and (2.16b), this equation also requires that the predicted critical point conform to the experimental value.

Because the original Kumar-Starling EOS could not describe the convergence of the saturated liquid and saturated vapour curves to the critical point, transition functions for

certain parameters were introduced which modify the equation over a range of reduced temperatures between approximately 0.95 and 1.05. While this does allow one to calculate the entire saturation boundary, as shown in Figure 2.5, the resulting modified equation of state exhibits some anomalous behaviour. On the vapour side it can be seen that the isotherms are very closely packed together for high reduced temperatures and that in some cases they intersect the saturation boundary in two locations. This means that the equation of state predicts two different temperatures for the same pressure and volume.

Another aspect of the equation that is notable is the steep slope of the isotherms in the stable and metastable liquid regions as compared with the other equations of state in this study.

Simonet-Behar-Rauzy (Behar et al. [1985]), Modified Simonet-Behar-Rauzy (Jullian et al. [1989])

The original SBR EOS is a non-cubic equation written as

$$P = \frac{RT}{v-b} - \frac{a}{v(v+b)} \left(1 - \gamma \frac{b}{v} + \delta \frac{b^2}{v^2} \right) \quad (2.18)$$

with a , b , γ and δ all expressible as functions of temperature and an acentric factor. The modifications proposed by Jullian et al. [1989] were intended to improve the vapour pressure predictions for heavy hydrocarbons. The basic structure of the equation is unchanged by the modifications but the rules for calculating the factors a and b are altered slightly.

Figures 2.6 and 2.7 are the saturation boundary plots for the original and modified equations, respectively. In both cases the EOS is unable to describe convergence of the

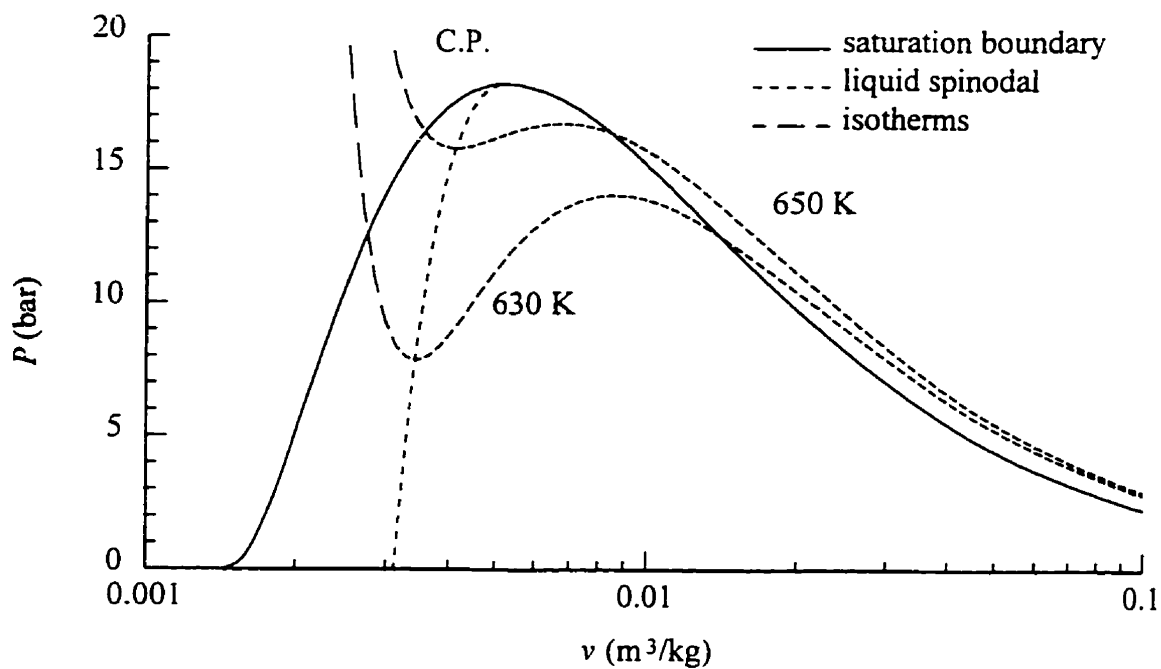


Figure 2.4. Thermodynamic properties of dodecane calculated with the Twu-Coon-Cunningham equation of state.

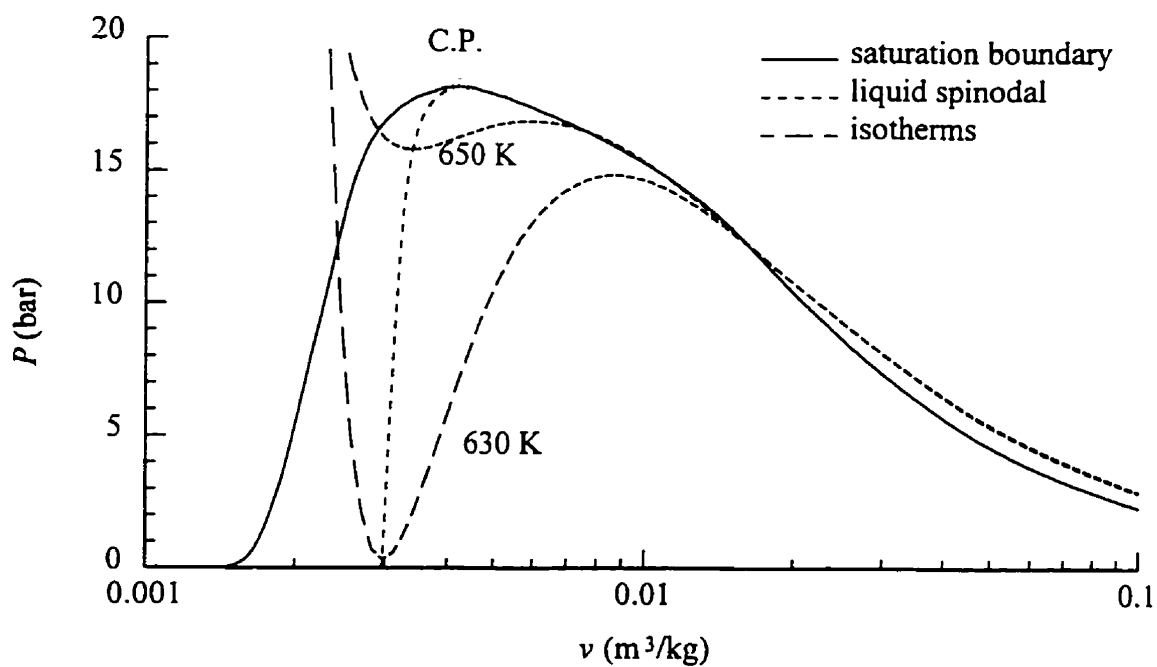


Figure 2.5. Thermodynamic properties of dodecane calculated with the Modified Kumar-Starling equation of state.

liquid and vapour branches of the saturation boundary at the critical point. However, the authors claim that special care was taken in fitting the isotherms in the vicinity of the critical point, so that the equation is a good predictor of P - v - T behaviour everywhere outside the region $0.99 < T_r < 1.01$.

Simplified Perturbed Hard Chain Theory (Shaver et al. [1995])

The SPHCT EOS is most easily expressed in the following fashion:

$$Z = 1 + c \left(\frac{4(\tau\tilde{\rho}) - 2(\tau\tilde{\rho})^2}{(1 - \tau\tilde{\rho})^3} - \frac{Z_M c v^* Y}{c v + c v^* Y} \right) \quad (2.19a)$$

$$Y = \exp\left(\frac{1}{2\tilde{T}}\right) - 1 \quad (2.19b)$$

Here c , τ and Z_M are constants. $\tilde{\rho}$ is equal to v^*/v , \tilde{T} is equal to T^*/T , and v^* and T^* are a characteristic volume and temperature respectively. This equation of state is based on statistical mechanics and without modification does not provide equilibrium property predictions accurately. Shaver et al. [1995] presented a combination of three techniques for improving the equation's accuracy: introducing critical point constraints, modifying the temperature dependence of the attractive term in the compressibility and "tuning" volumetric predictions using a volume translation strategy.

Since Shaver et al. do not quote specific values of the constant c or the characteristic volume and temperature for dodecane, the equation of state was fitted for this substance using their recommended techniques. A total of 10 values of the saturation pressure between the temperatures of 380 K and 550 K were generated using the FKT correlation and the constant c in the EOS was fit by a least squares method to minimize the saturation pressure

error. Simultaneous non-linear equations in the variables v^* , T^* and v_c (critical volume) which define the three critical point constraints were solved at each step of the minimization procedure.

After generating a saturation boundary using the optimized value of c , the results were subjected to a volume translation. A volume translation is essentially a technique by which isotherms are translated volumetrically in the P - v plane to improve property predictions. A translation of this sort does not affect previously calculated vapour-liquid equilibria because the equal areas construction for the isotherm is unchanged by a simple shift to the right or left. Following Shaver et al. volume translations at each temperature were done according to

$$v = v_{EOS} + \delta_c (1 - S^{c_1} - S^{c_2}) \quad (2.20a)$$

$$S = \frac{1}{1+d} \quad (2.20b)$$

$$d = \frac{1}{RT_c} \left(\frac{\partial P}{\partial \rho} \right)_T^{EOS} \quad (2.20c)$$

$$\delta_c = \frac{RT_c}{P_c} (Z_c^{EOS} - Z_c) \quad (2.20d)$$

Here the identifier EOS refers to values calculated by the untranslated equation of state, and the derivative is evaluated at the saturated liquid condition. The constants c_1 and c_2 were optimized by a least squares method using volumes generated by the Hankinson-Thomson correlation between the temperatures of 300 K and 640 K. This volume translation technique ensures that the experimental critical point is described exactly because it incorporates the actual compressibility, Z_c .

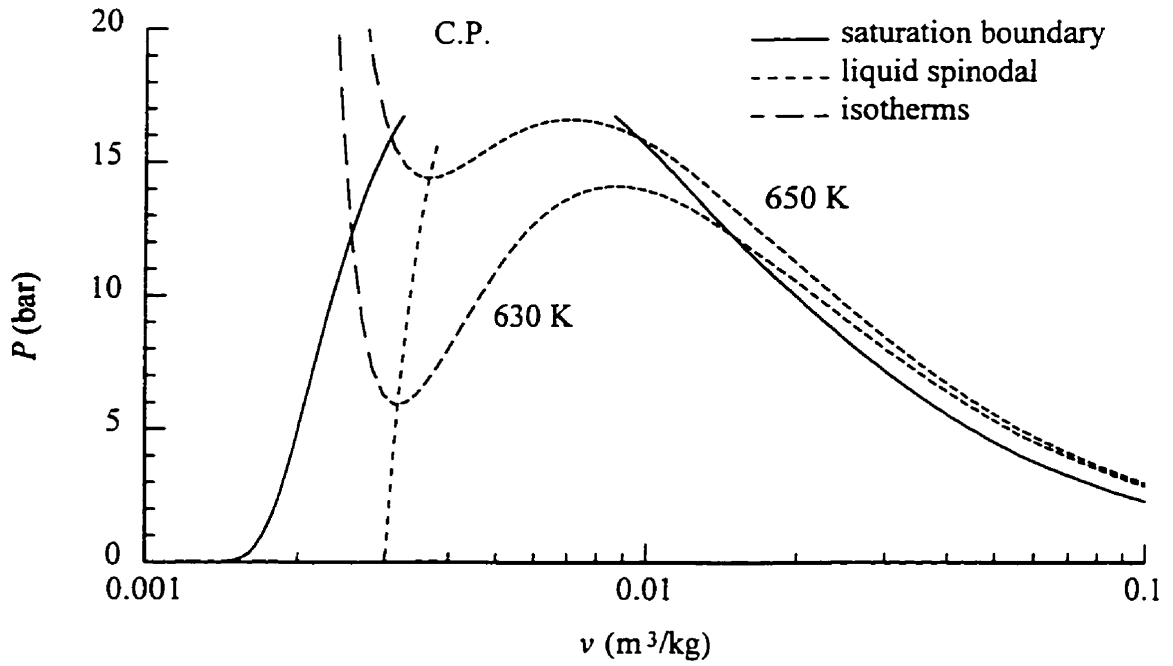


Figure 2.6. Thermodynamic properties of dodecane calculated with the Simonet-Behar-Rauzy equation of state.

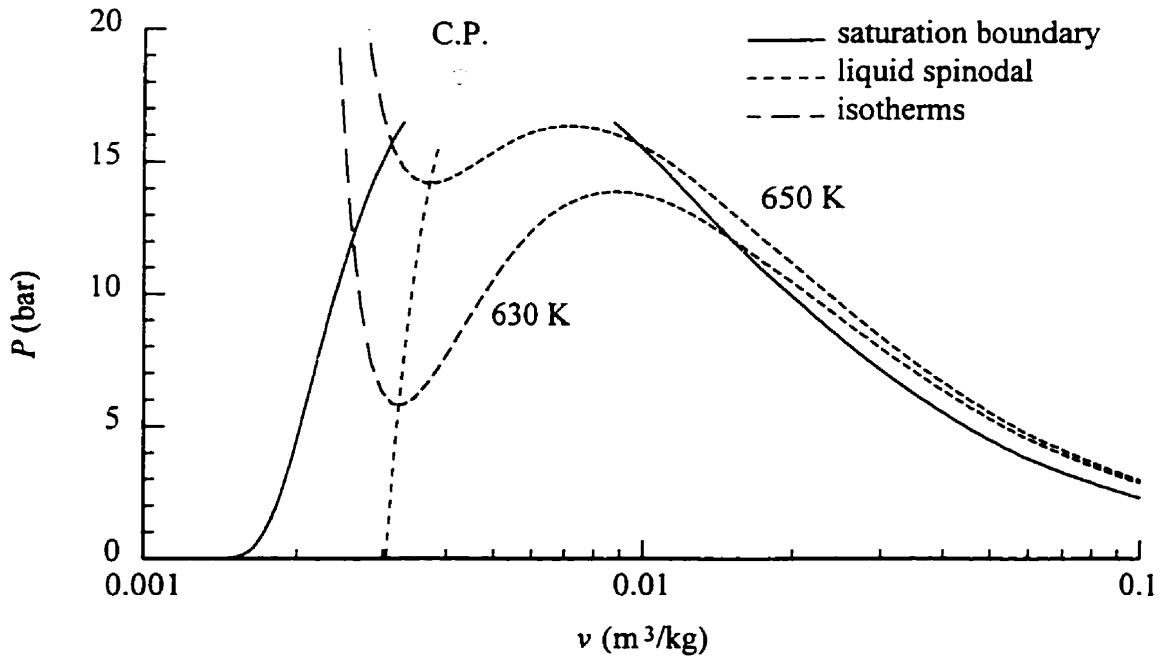


Figure 2.7. Thermodynamic properties of dodecane calculated with the modified Simonet-Behar-Rauzy equation of state.

Results for the various optimized and calculated constants for dodecane are given in the table below.

Table 2.1. SPHCT equation of state parameters for dodecane.

Parameter	Value
v^* (cm ³ /mol)	113.399
T^* (K)	248.74
c	2.7856
c_1	0.017906
c_2	1.422806

Figure 2.8 is a plot of the saturation boundary and isotherms for the translated equation. The saturation boundary is described in a plausible fashion right to the critical point and the isotherms are reasonably shaped. However, closer examination of near-critical isotherms at supercritical pressures (not shown) reveals that the volume translation has the unfortunate effect of producing many points with multiple temperature values.

Another potential problem is the effect of the volume translation on other thermodynamic properties. Determining properties such as enthalpy and entropy requires that the EOS be integrated, but the complex volume dependence of the equation would probably preclude any analytic derivation.

Modified Benedict-Webb-Rubin (Soave [1995])

Like the Starling-Han EOS and the Lee-Kesler EOS, the equation recently proposed by Soave is one of many BWR-type equations having a similar functional form:

$$Z = Pv / RT = 1 + B\rho + C\rho^2 + D\rho^4 + E\rho^2(1 + F\rho^2)\exp(-F\rho^2) \quad (2.21)$$

The principal difference is the exponent of the fourth term on the right hand side, which in all previous incarnations of this equation has been 5. Other changes involve new laws for the temperature and acentric factor dependence of the coefficients B through F . The equation is subject to the usual critical point constraints, with one slight modification. Instead of forcing the equation to reproduce the experimental critical compressibility exactly, Soave has chosen to match the Rackett compressibility Z_{Ra} . This is a quantity from a frequently used saturated liquid density correlation which is normally within about 1% of Z_c .

Figure 2.9 shows that this equation gives a very good qualitative representation of the saturation boundary for dodecane, with excellent convergence near the critical point. The high temperature isotherms are quite steep in the metastable liquid region, but represent a qualitative improvement over the Starling-Han EOS. However, it was found that at lower temperatures (i.e. 360 K, not shown) the peculiar four extrema behaviour seen in the Starling-Han equation occurs. Whether this is endemic to all BWR-type equations or only occurs for certain values of the acentric factor is unclear without further investigation.

2.2.3. Comparison Results

The liquid spinodals calculated from the various equations of state and the

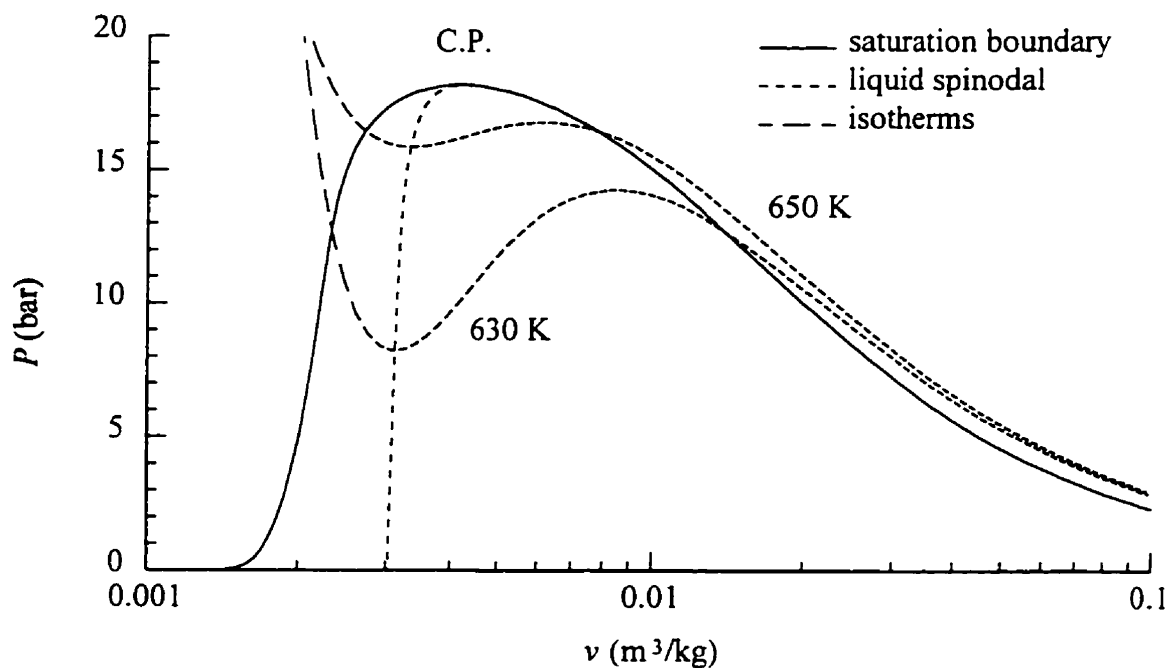


Figure 2.8. Thermodynamic properties of dodecane calculated with the Simplified Perturbed Hard Chain Theory equation of state.

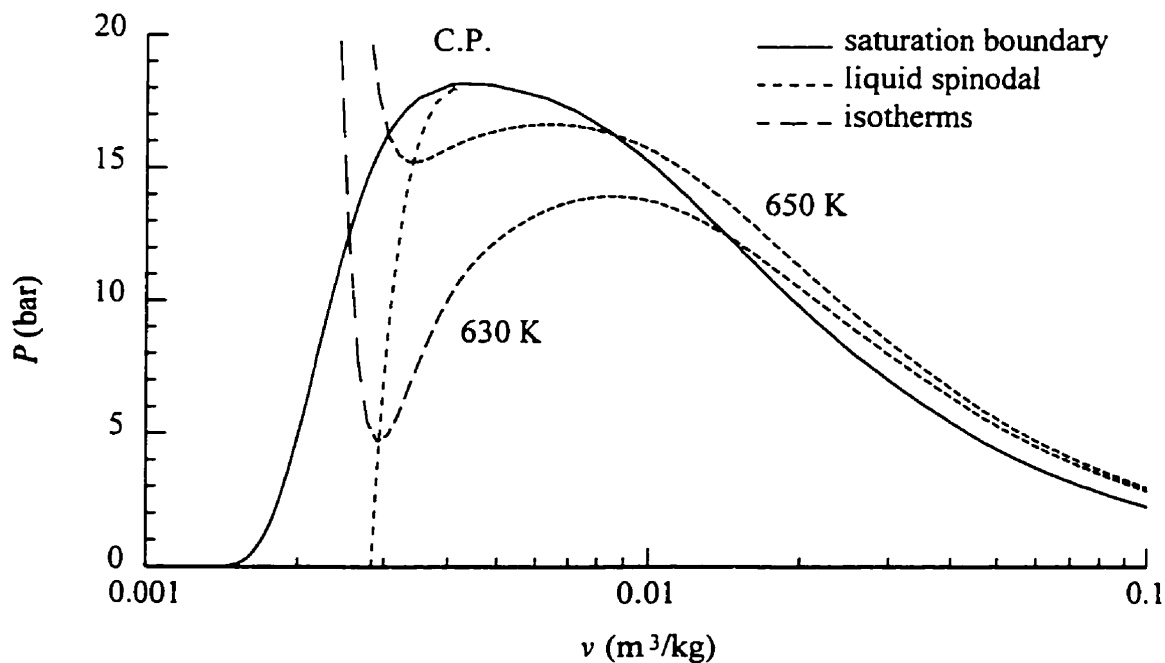


Figure 2.9. Thermodynamic properties of dodecane calculated with the modified Benedict-Webb-Rubin equation of state.

homogeneous nucleation limit curve are shown in Figure 2.10. The SPHCT and TCC equations have the shallowest pressure minima and conform best to the nucleation theory. The spinodal curves of the SBR-type equations do not approach the critical point due to the limitations on the range of applicability of these equations. The SH equation produces an irregular curve due to the transition of its isotherms from having four extrema to two, but in an average sense is fairly close to the nucleation curve over the range of pressures shown. However, at lower temperatures the curve is expected to diverge appreciably. Probably as a result of the transition function applied to force critical convergence, the spinodal of the MKS equation is oddly shaped for positive pressures. Finally, the MBWR spinodal diverges rapidly from that given by nucleation theory. It should be noted that the spinodal and homogeneous nucleation limit curves have been extended to points with negative pressures. Although the properties of liquids under tension are not of primary interest here, the location of the spinodal curve at low temperatures has implications for the overall shape of the corresponding metastable isotherms. Figure 2.10 is plotted for temperatures above 590 K only to clearly distinguish the various curves. Given that the comparisons made on the basis of this figure are largely qualitative, it is sufficient to extrapolate the trends of each curve to estimate the spinodal locations at lower temperatures.

Figures 2.11 and 2.12 are plots of percentage error for each equation of state compared with the correlations given in section 2.2.1. Saturation pressure errors are shown in Figures 2.11(a) and 2.11(b), and saturated liquid volume errors are shown in Figures 2.12(a) and 2.12(b). The vertical lines on the latter two figures indicate a “cut-off”

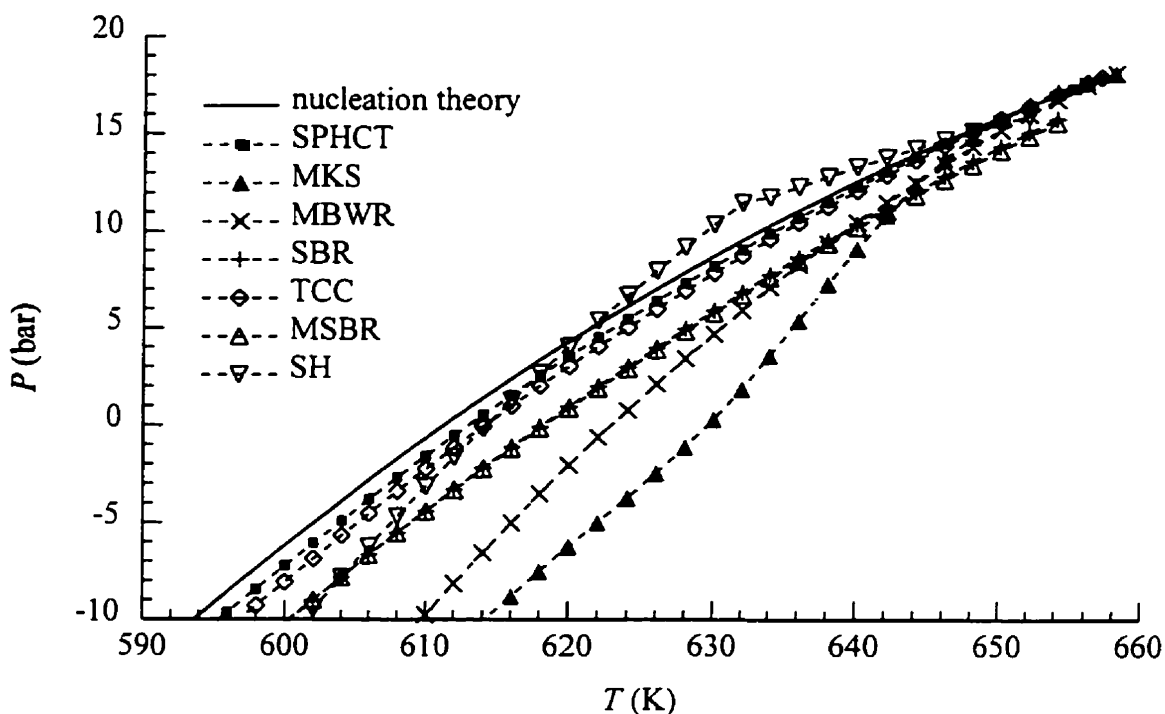
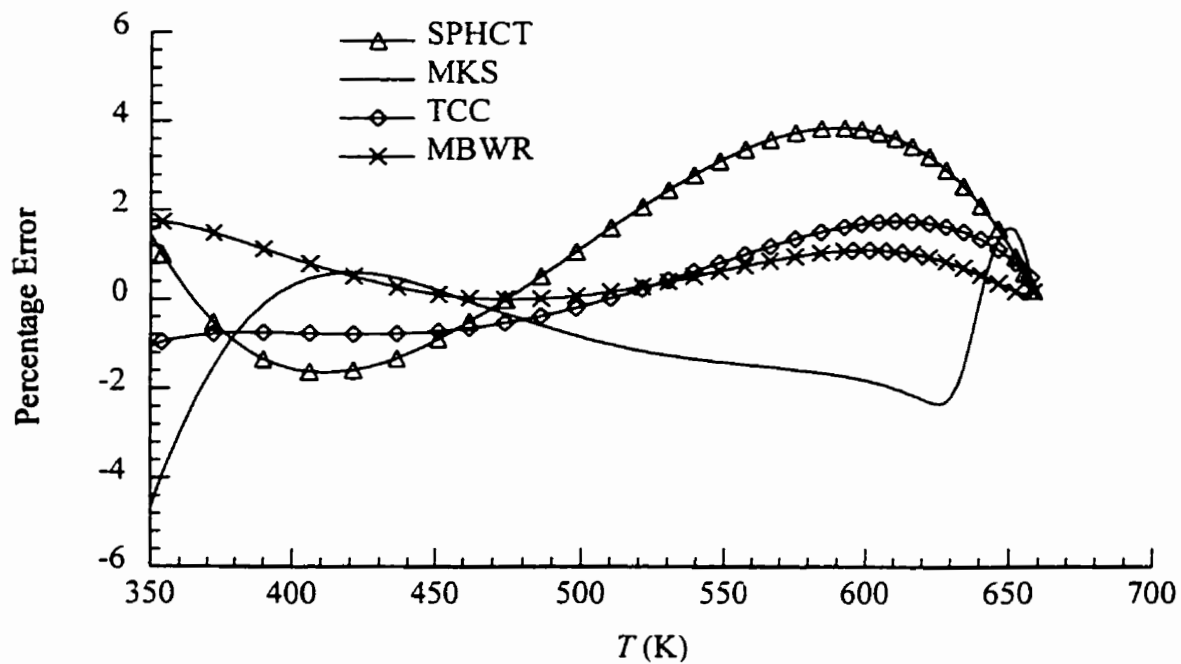


Figure 2.10. Comparison of equation of state spinodals with the kinetic limit of superheat obtained from homogeneous nucleation theory.

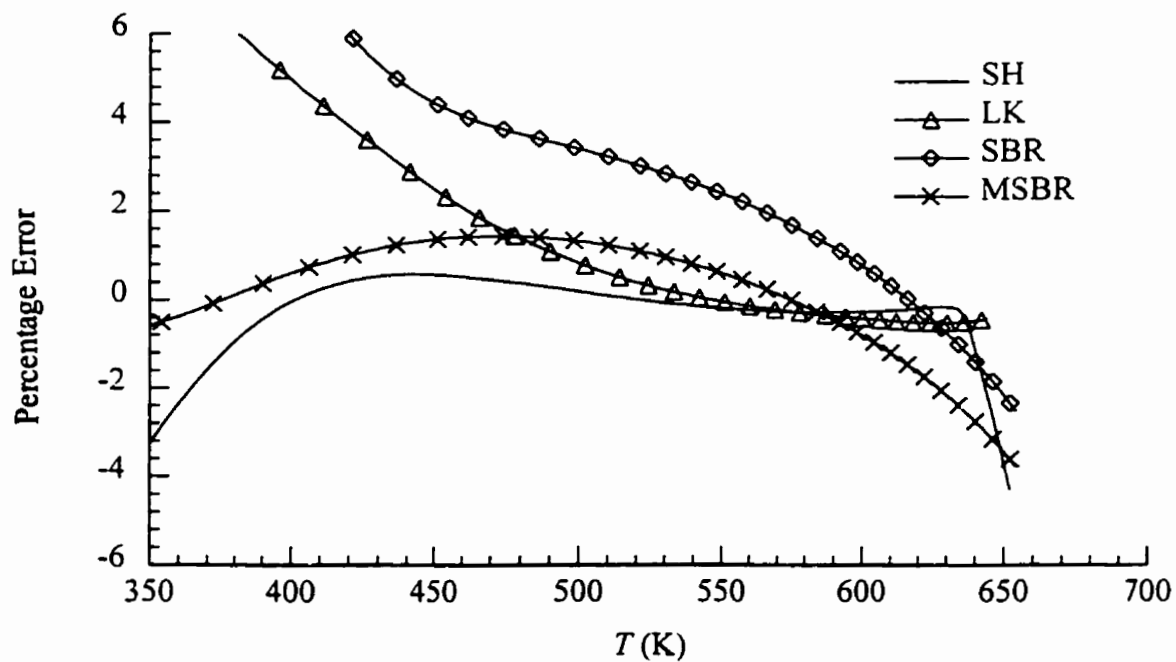
temperature above which the comparison correlation is likely to be no more accurate than some of the equations of state.

Over the entire temperature range, the TCC and MBWR equations seem best able to predict saturation pressure with a consistently low error. The MKS and SH equations are also quite accurate between approximately 400 K and 640 K. The modified version of the SBR equation represents a significant improvement over the original, especially at low temperatures.

For saturated liquid volume predictions, the accuracy of the TCC and SH equations deteriorates markedly with increasing temperature as a result of their poor near-critical

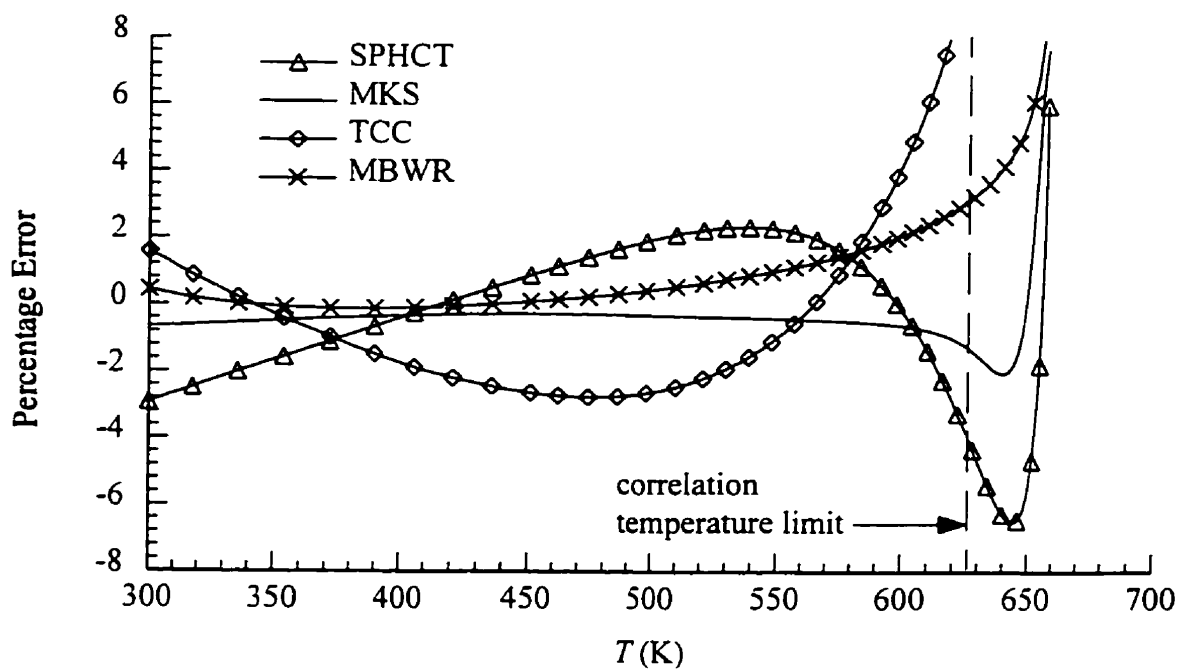


(a)

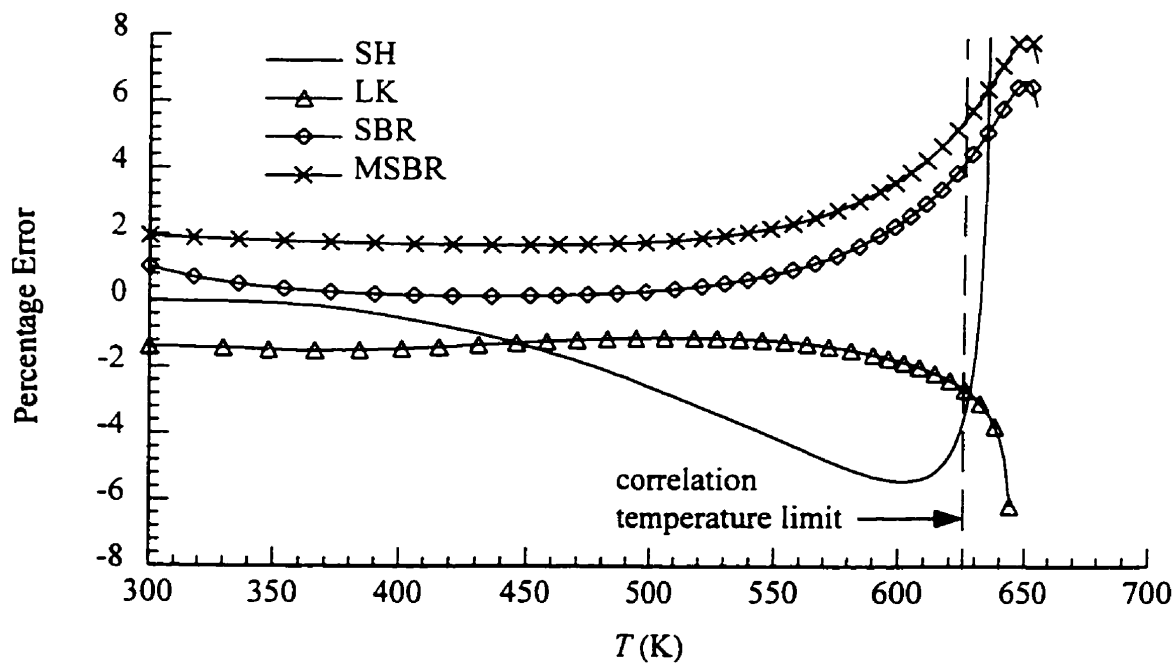


(b)

Figure 2.11. Equation of state saturation pressure error with respect to the Frost-Kalkwarf-Thodos correlation.



(a)



(b)

Figure 2.12. Equation of state saturated liquid volume error with respect to the Hankinson-Thomson correlation.

performance. The MKS and MBWR equations have the lowest percentage error over the largest range of temperatures. Modifying the SBR equation to improve vapour pressure predictions appears to have had a somewhat negative effect on the liquid volume accuracy.

2.2.4. Discussion and Equation Selection

As expected, this study has shown that most equations of state in current use are formulated almost entirely with the purpose of accurately describing vapour-liquid equilibria over as wide a temperature range as possible. As a result of this focus, care is not always taken to ensure that the equations predict behaviour that is reasonable from a physical standpoint throughout both stable and metastable regions. For example, two equations were found to be multi-valued and two others have isotherms with four extrema. Without further study, it is impossible to say which of the equations examined provides physically reasonable values for such derived quantities as sound speed, heat capacity or enthalpy. There is also considerable uncertainty about the accuracy of the vapour branch of the saturation boundary given by each equation, as no experimental data could be found.

It appears that none of the equations of state in this study have high temperature isotherms shaped appropriately to predict both accurate equilibrium properties and spinodal values. In constructing his version of the BWR EOS, Soave included subcooled liquid volumes in his fitting data. Therefore it is likely that the isotherms of the MBWR EOS have approximately the correct slope when crossing the saturation boundary, but should reach the pressure minimum sooner. Of course such a change in the metastable liquid branch of the equation would require substantial changes elsewhere on the isotherm to preserve its

equilibrium characteristics. What is necessary, in effect is something akin to the isotherms of the SH EOS around 630 K. This highlights the extraordinary difficulty of formulating an equation of state valid for all regions of P - v - T space.

From a purely qualitative point of view, the plot of the saturation boundary and isotherms for the SPHCT EOS (Figure 2.8) make it an excellent choice. It also predicts the pressure-temperature behaviour of the liquid spinodal quite well. However, the thermodynamic inconsistency near the critical point and other problems caused by the volume translation disqualify it as a possible selection for use in flow modeling. The LK method is ruled out on the basis of its inability to represent metastable states. The SH EOS performs poorly near the critical point and also produces an irregular spinodal curve. Poor saturation pressure prediction is the main fault of the original SBR EOS. The percentage error plots indicate that the MKS EOS is the best overall quantitatively for predicting the vapour-liquid equilibria of dodecane. Unfortunately, as mentioned previously, its multi-valuedness and the shape of its spinodal and isotherms are areas of concern which make it less attractive than simpler but slightly less accurate equations. This leaves the relatively uncomplicated TCC EOS, which is not a bad choice, especially at temperatures below 600 K, and the MBWR and MSBR equations of state which are also excellent for predicting equilibrium properties.

The apparent inaccuracy of the liquid spinodal represents the only major flaw of the MBWR EOS. If the spinodal is used as a deciding factor, the TCC equation outperforms both of the other two options. However, based on the supposition that the MBWR equation

best describes liquid density data along each isotherm, it would seem that the much more rounded isotherms of the TCC EOS overrepresent the liquid isothermal compressibility. A suitable tradeoff between these conflicting considerations is provided by the MSBR EOS. Therefore, the MSBR equation was selected to be used for all subsequent calculations. As an addendum to this conclusion, it should be noted that both the MSBR and TCC equations are inaccurate near the thermodynamic critical point. If reliable property data in this region are required, the use of the MBWR EOS is recommended.

2.3. Residual Properties of the MSBR Equation of State

An equation of state of the form $P=P(T,v)$ is incomplete in the sense that it is not equivalent to a fundamental relation $u=u(s,v)$ from which all other thermodynamic properties such as P , T and μ can be obtained by direct partial differentiation. The concept of residual functions is a useful means of working around this problem. For a given thermodynamic property evaluated at some P and T , a residual or departure function can be calculated which expresses the difference between the actual value of the property and its value for an ideal gas state having the same temperature and at some reference pressure P^0 . The ideal gas state, indicated by the superscript "0" is of course defined by

$$P^0 v^0 = RT \quad (2.22)$$

where the choice of reference state is somewhat arbitrary. Commonly used choices include $P^0=1$, $v^0=1$ and $P^0=P$, the real gas pressure. If a constant value is chosen for either P^0 or v^0 , the ideal gas constant R in equation (2.22) must be in a consistent set of units. The residual functions will in general depend on the reference state selected; however, the total expression

for a given thermodynamic property differs only by a constant value when derived for two different reference states. The residual function for the Helmholtz energy, Φ^R , is perhaps the simplest to derive from a $P=P(T,v)$ equation, as shown by Reid, Prausnitz and Poling [1987]

$$\Phi^R = \Phi - \Phi^0 = - \int_{\infty}^v \left(P - \frac{RT}{v} \right) dv - RT \ln \frac{v}{v^0} \quad (2.23)$$

For the MSBR equation of state, the residual Helmholtz energy is

$$\begin{aligned} \Phi^R = & -RT \ln \left(\frac{v-b}{v} \right) - \frac{a}{b} (1 + \delta + \gamma) \ln \left(\frac{v+b}{v} \right) + \frac{a(\delta + \gamma)}{v} - \frac{ab\delta}{2v^2} \\ & - RT \ln \left(\frac{v}{v^0} \right) \end{aligned} \quad (2.24)$$

Expressions for the residual functions for entropy s and enthalpy h follow:

$$\begin{aligned} s^R = s - s^0 &= - \frac{\partial}{\partial T} (\Phi - \Phi^0)_v \\ s^R &= R \ln \left(\frac{v}{v^0} \right) + R \ln \left(\frac{v-b}{v} \right) + \frac{ab\delta' + ab'\delta + a'b\delta}{2v^2} + \frac{b'RT}{b-v} \\ &+ \frac{a(\delta' + \gamma')}{b} \ln \left(\frac{v+b}{v} \right) - \frac{a(\delta' + \gamma') + a'(\delta + \gamma)}{v} + \frac{ab'(1 + \delta + \gamma)}{b(v+b)} \\ &+ \left(\frac{a'}{b} - \frac{ab'}{b^2} \right) (1 + \delta + \gamma) \ln \left(\frac{v+b}{v} \right) \end{aligned} \quad (2.25)$$

$$h^R = h - h^0 = \Phi^R + Ts^R + RT(Z - 1) \quad (2.26)$$

The prime superscript above indicates differentiation with respect to T . To calculate the actual enthalpy and entropy, the ideal gas values at the reference state must be added to the residual functions. For an ideal gas the enthalpy is only a function of temperature:

$$dh^0 = c_p^0 dT \quad (2.27)$$

Therefore, all that is required to obtain an expression for h^0 is an appropriate expression for the ideal gas specific heat at constant pressure, c_p^0 , as a function of temperature. A typical correlation is expressed in the form of a polynomial:

$$c_p^0 = A + BT + CT^2 + DT^3 \quad (2.28)$$

Constants A, B, C and D for dodecane were taken from Reid, Prausnitz and Poling [1987].

Assuming a reference state $P^0=1$, the ideal gas enthalpy and entropy expressions can be written as

$$h^0 = AT + \frac{B}{2}T^2 + \frac{C}{3}T^3 + \frac{D}{4}T^4 \quad (2.29)$$

$$s^0 = A \ln T + BT + \frac{C}{2}T^2 + \frac{D}{3}T^3 \quad (2.30)$$

As an example, the change in entropy between real gas states 1 and 2 can be calculated in the following fashion:

$$\begin{aligned} s_2 - s_1 &= [(s - s^0) + s^0]_2 - [(s - s^0) + s^0]_1 \\ &= s_2^R - s_1^R + s_2^0 - s_1^0 \end{aligned} \quad (2.31)$$

Since the ideal gas states in (2.31) are both at the same reference pressure, this allows the ideal gas entropy in equation (2.30) to be written only as a function of temperature. In other words, the volume dependence of the ideal gas entropy is contained in the expression for the residual function. In addition, the constants of integration for equations (2.29) and (2.30) have been arbitrarily set to zero for simplicity, as they would merely cancel in equation (2.31).

Other useful thermodynamic properties can be obtained through the concept of residual functions, or may be derived from properties already calculated by using

thermodynamic identities. The single phase speed of sound c , which is used in gas dynamic calculations can be written as

$$c = v \sqrt{\frac{T}{c_v} \left(\frac{\partial P}{\partial T} \right)_v - \left(\frac{\partial P}{\partial v} \right)_T} \quad (2.32)$$

where c_v is the specific heat at constant volume. The thermodynamic equilibrium sound speed for a two-phase fluid is more difficult to derive, but can be expressed in closed form starting with the definition of the speed of sound $c^2 = (\partial P / \partial \rho)_s$ and proceeding from the following equation

$$\frac{1}{\rho} = \frac{(1-x)}{\rho_l} + \frac{x}{\rho_v} \quad (2.33)$$

Taking the derivative of the above relation with respect to P at constant s gives

$$\frac{\partial}{\partial P} \left(\frac{1}{\rho} \right)_s = \frac{\partial}{\partial P} \left[\frac{(1-x)}{\rho_l} + \frac{x}{\rho_v} \right]_s \quad (2.34)$$

which leads to

$$\frac{1}{c^2} = \rho^2 \left(\frac{1}{\rho_l} - \frac{1}{\rho_v} \right) \left(\frac{\partial x}{\partial P} \right)_s - (1-x) \rho^2 \frac{d}{dP} \left(\frac{1}{\rho_l} \right)_{sat} - x \rho^2 \frac{d}{dP} \left(\frac{1}{\rho_v} \right)_{sat} \quad (2.35)$$

The subscripts v and l denote properties evaluated at the vapour and liquid saturation boundaries and at pressure P , and x is the quality. The last two derivatives in equation (2.35) must be evaluated along the saturation boundary. The appropriate expression is

$$\frac{d}{dP} \left(\frac{1}{\rho} \right)_{sat} = \frac{(c_p - c_v) \frac{v_{lv}}{h_{lv}} + \left(\frac{\partial P}{\partial T} \right)_v / \left(\frac{\partial P}{\partial v} \right)_T}{\left(\frac{\partial P}{\partial T} \right)_v} \quad (2.36)$$

where v_{lv} is equivalent to $v_v - v_l$, and all other properties are evaluated at either a saturated liquid or saturated vapour state. To complete the calculation, the derivative $(\partial x / \partial P)_s$ must be evaluated in a form involving functions that can be easily calculated from the equation of state. One possibility is

$$\left(\frac{\partial x}{\partial P}\right)_s = \frac{(1-x) \left(\frac{c_{p_l} v_{lv}}{h_{lv}} + \left(\frac{\partial P}{\partial T}\right)_{v_l} / \left(\frac{\partial P}{\partial v}\right)_{T_l} \right) + x \left(\frac{c_{p_v} v_{lv}}{h_{lv}} + \left(\frac{\partial P}{\partial T}\right)_{v_v} / \left(\frac{\partial P}{\partial v}\right)_{T_v} \right)}{s_l - s_v} \quad (2.37)$$

Substituting equations (2.36) and (2.37) into (2.35) gives an expression from which the two-phase sound speed may be easily determined. An important qualifier to the derivation presented here is the assumption of *equilibrium* between the phases. In other words, a two-phase mixture responds to pressure disturbances by instantaneously varying its quality through vapourization or condensation to maintain an isentropic condition. The properties of the individual phases must always follow the saturation boundary. This situation may be realized approximately for a case in which the phases are finely interspersed, such as in a mist flow, but in general it is more likely that limitations on the rate of phase transition will cause the liquid and vapour components to behave in an independent, non-equilibrium manner.

The speed of sound is directly related to the shape of isentropes in both the single phase and two-phase regions of the P - v plane. Figure 2.13 shows a sample isentrope for dodecane which begins in the subcooled liquid region, traverses the two-phase domain, and extends out into the superheated vapour region. The continuations of the single phase isentropes into the metastable regions are shown by the dashed lines. Although it is

somewhat distorted by the logarithmic scale of the ordinate, the shape of the equilibrium isentrope curve results in the speed of sound characteristic shown in Figure 2.14. The “kinks” in the isentrope at the saturation boundary cause discontinuities in the sound speed. Substances which have equilibrium isentropes that intersect the saturation boundary at both the liquid side and the vapour side are part of a general class of fluids termed retrograde. Obviously, dodecane qualifies as one such substance. The precise definition of retrograde behaviour and its implications for phase change processes is the subject of the following section.

2.4. Retrograde Fluids

The essential feature of a retrograde fluid is that its vapour can condense when subjected to an adiabatic compression. This is in contrast to a non-retrograde or “regular” fluid, which will only condense upon adiabatic expansion. A sufficient condition for a substance to be classified as retrograde is that some portion of the saturated vapour boundary in the temperature-entropy plane must have positive slope:

$$\left(\frac{\partial s}{\partial T}\right)_{sat} > 0 \quad (2.38)$$

The distinction between regular and retrograde behaviour is made clear in Figure 2.15. The isentropic condensation processes for the two types of fluids are indicated by arrows.

A useful expression relating the slope of the saturation boundary on the T - s plane to other thermodynamic properties can be derived, as shown by Thompson et al. [1986]:

$$T\left(\frac{\partial s}{\partial T}\right)_{sat} = c_v + T\left(\frac{\partial P}{\partial T}\right)_v \left(\frac{\partial v}{\partial T}\right)_{sat} \quad (2.39)$$

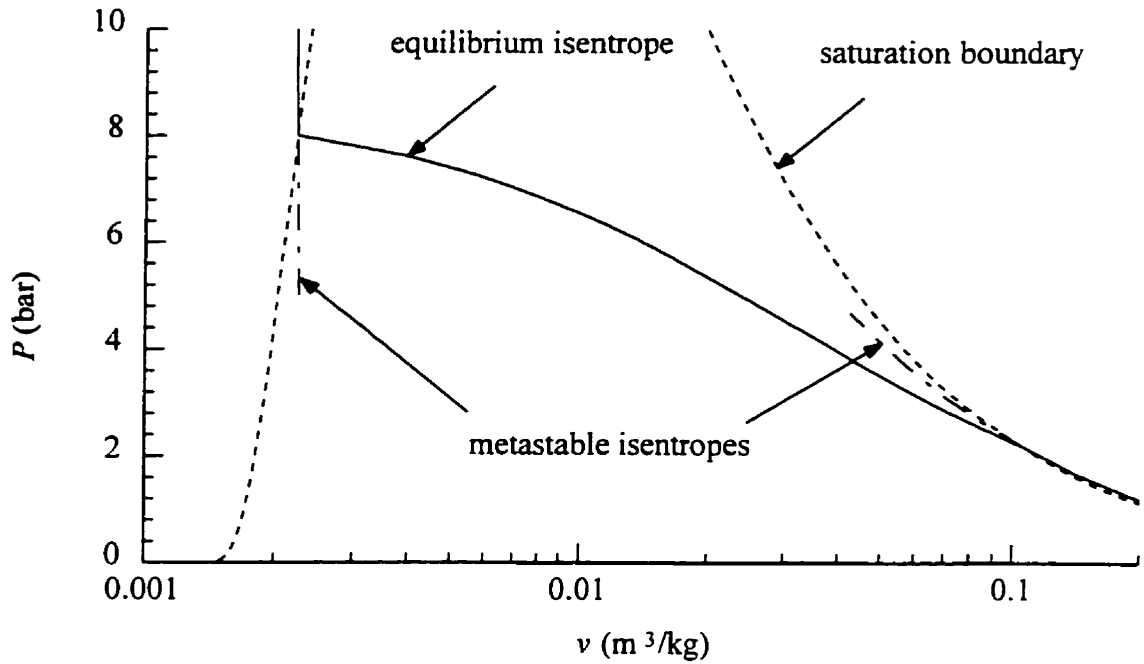


Figure 2.13. Sample equilibrium isentrope and extensions of single phase branches into metastable regions in the pressure-volume plane.

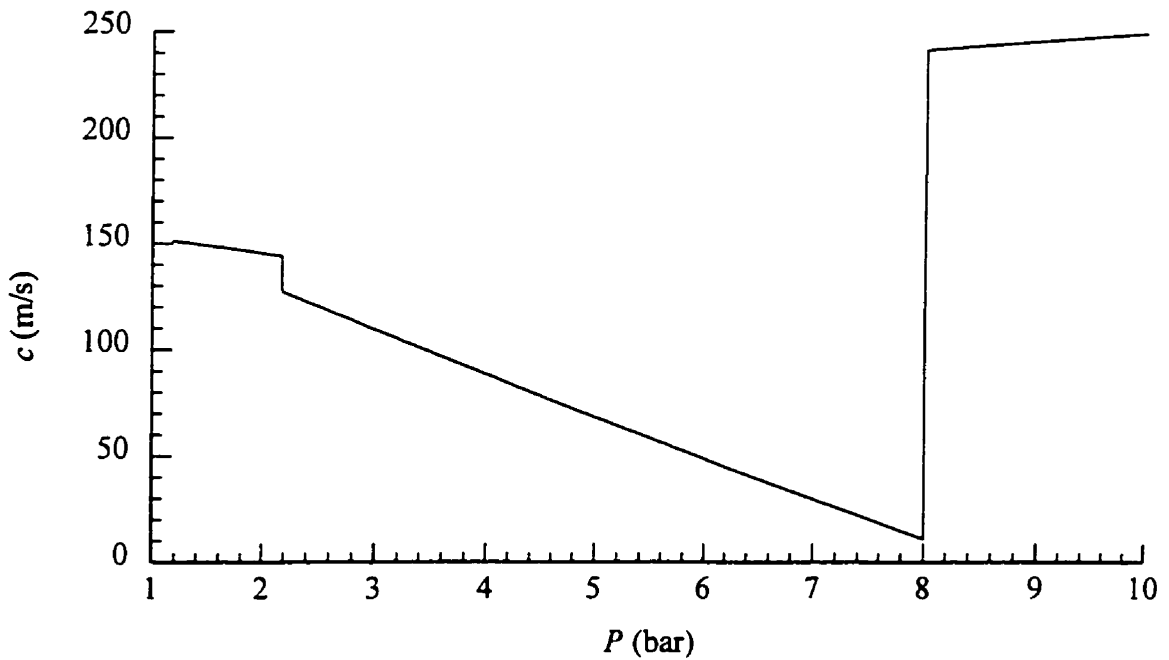


Figure 2.14. Speed of sound as a function of pressure along the equilibrium isentrope shown in Figure 2.13.

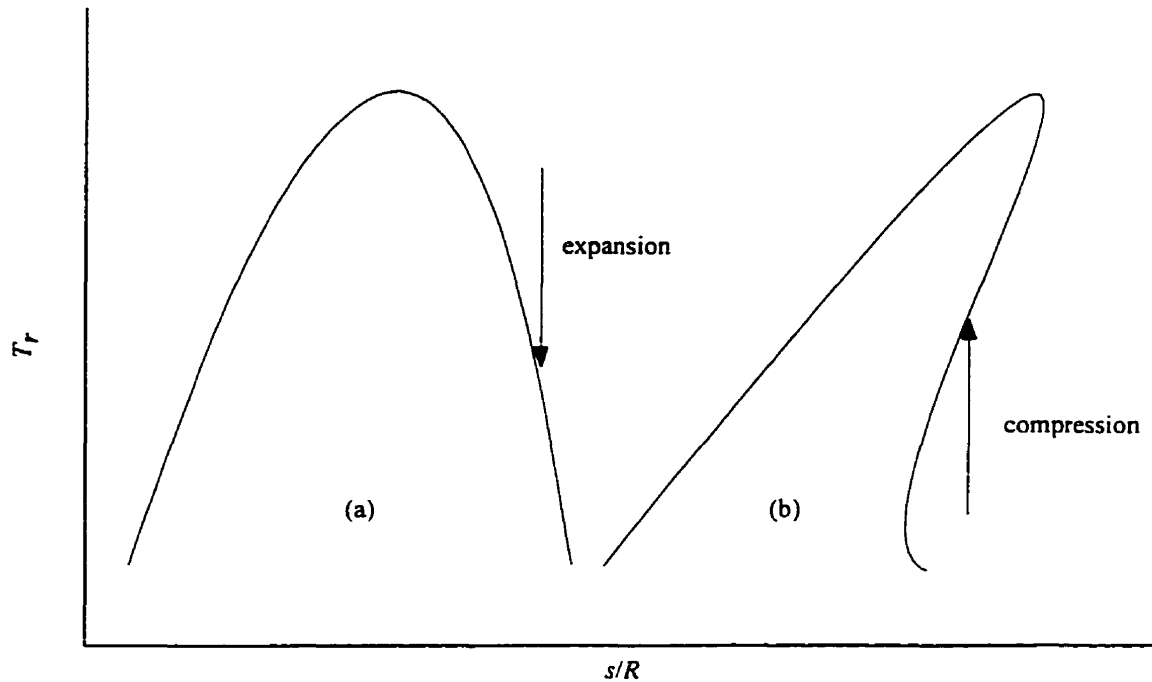


Figure 2.15. Isentropic processes leading to condensation for (a) a regular fluid and (b) a retrograde fluid, in the normalized temperature-entropy plane.

In this equation, c_v is the specific heat capacity at constant volume, and the partial derivatives and heat capacity are evaluated in the single phase region immediately adjacent to the saturation boundary. On the liquid side of the saturation boundary, both terms on the right hand side of equation (2.39) are positive right up to the critical point and therefore the slope is always positive. On the vapour side, the second term on the right hand side of equation (2.39) is always negative. If c_v is sufficiently large, the slope may become positive in some region of the saturation boundary, satisfying the condition for retrogradicity as given by equation (2.38).

As a convenient means of classifying substances as either regular or retrograde, a standard heat capacity \tilde{c}_v has been defined by Thompson and Sullivan [1975] as

$$\tilde{c}_v = \frac{c_v^0(T_c)}{R} \quad (2.40)$$

where c_v^0 is the ideal gas specific heat at the critical temperature of the substance of interest. Retrograde behaviour appears when $\tilde{c}_v > 11.2$ (Detleff et al. [1979]). Molar heat capacity is known to be an increasing function of molecular weight in related series of substances, such as the n-alkane hydrocarbons. For example, propane (C_3H_8) has a value of \tilde{c}_v of 9.64, and as such would be classified as a regular fluid, whereas dodecane ($C_{12}H_{26}$) has a value of \tilde{c}_v of 60.4 and is highly retrograde. Therefore, retrogradicity is usually associated with fluids having high molecular weight, because complex molecules have many internal vibrational degrees of freedom that may be used to store internal energy.

A great variety of interesting liquid-vapour phase change phenomena have been postulated for retrograde systems. Some of the possibilities identified by various researchers include partial and complete liquefaction shock waves, rarefaction shocks, complete evaporation shocks and liquid evaporation waves (Thompson and Meier [1985]). Of these, the existence of the complete liquefaction shock wave has been experimentally established by Detleff et al. [1979] using a retrograde fluorocarbon as the test fluid in a shock tube apparatus. Measurement of thermodynamic properties upstream and downstream of the liquefaction shock produced by reflection at the end of the tube confirmed the validity of applying the Rankine-Hugoniot equation of classical discontinuity theory to this type of shock. Thompson et al. [1986] experimentally and numerically studied the flow of a partial liquefaction shock wave emerging from the open end of a shock tube. Their results indicated

the presence of a mixture evaporation (rarefaction) shock wave in the unsteady two-dimensional flow behind the liquefaction shock front.

Closely associated with the discontinuities in sound speed at the saturation boundary shown in Figure 2.14 are two wave splitting processes in fluids of high specific heat described by Thompson et al. [1987] and Chaves et al. [1985]. The first, vapour-condensation shock splitting, was observed in the open-ended shock tube experiment described above. In this process, a liquefaction shock splits into a forerunner wave and a following condensation discontinuity. The onset of this behaviour occurs where the strength of the liquefaction shock is at the point at which the upstream superheated vapour is adiabatically compressed just enough to reach a metastable vapour state of critical supersaturation. A weaker shock strength results in less than critical supersaturation and a delay of phase change until a following condensation discontinuity is encountered. The other splitting phenomenon which is of direct relevance here is that of liquid-evaporation wave splitting. This is typically encountered in diaphragm burst experiments. In these experiments, a vertical column is filled with liquid in equilibrium with its vapour, usually maintained at a high reduced temperature. The two-phase system (liquid on the bottom, vapour on top) is isolated from a low pressure chamber above by a breakable diaphragm. When the diaphragm is mechanically ruptured, a forerunner rarefaction wave propagates into the vapour and is transmitted into the liquid, where it moves at the speed of sound in the liquid. The pressure drop caused by this wave superheats the liquid, resulting in nucleation and the development of a second front which follows at a slower speed and rapidly evaporates the liquid (see Figure 2.16). This type of phenomena provides a one-dimensional

analog to the system considered in the present work. Evaporation waves have been observed by several researchers and a model for the change in thermodynamic properties across the interface has been proposed.

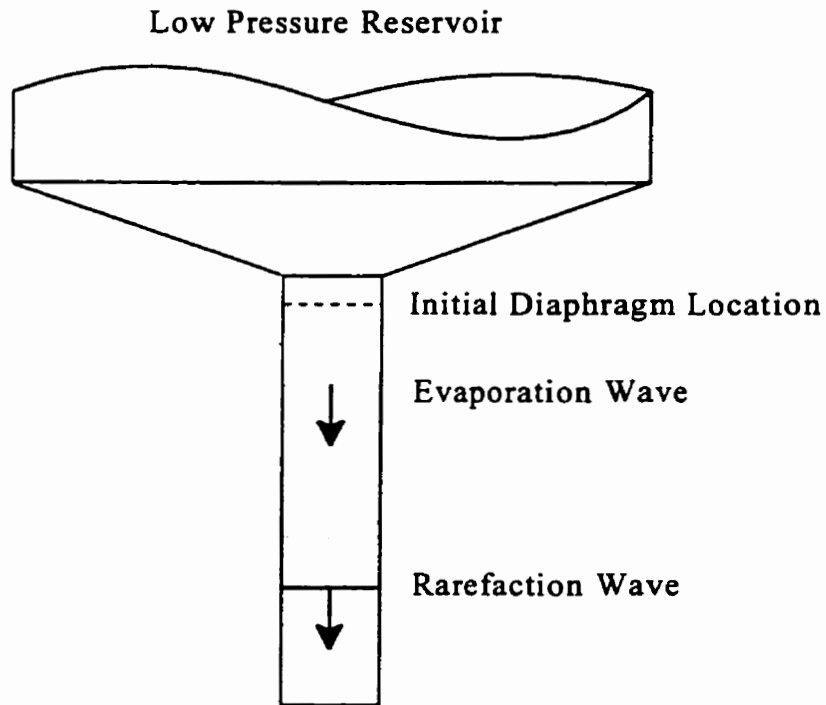


Figure 2.16. Schematic of a diaphragm burst experiment.

3. EVAPORATION WAVES

3.1. Previous Observations of Evaporation Waves

3.1.1. *Internal Flows*

The wave splitting process of diaphragm burst experiments is not strictly limited to retrograde fluids. In fact, evaporation waves have been observed by several researchers in regular fluids such as water. The distinction between the retrograde and non-retrograde cases lies in the possible thermodynamic states attainable by the fluid immediately downstream of the evaporation wave. If the fluid is regular, the downstream state is necessarily two-phase. A regular fluid cannot store enough energy when superheated to effect a complete phase change, and the Jakob number of equation (2.4) is necessarily less than unity for metastable states up to the maximum superheat limit.

Perhaps the first observation of an evaporation wave was made by Turner [1962], who conducted diaphragm burst experiments with water at pressures up to 50 bar and at various initial temperatures up to 238°C in an effort to study cavitation mechanisms. The wave splitting process typical of this type of experiment occurred, but no attempt was made to measure the velocity of the evaporation wave. Similar experiments also conducted with water by Friz [1965] established the velocity of the evaporation front as a function of the degree of liquid superheating.

More comprehensive work was done by Grolmes and Fauske [1974], who rapidly depressurized water, methyl alcohol and refrigerant 11 in glass tubes. Unlike earlier studies,

extra care was taken in preparing the fluids and tubes so that nucleation of bubbles at the wall in the liquid ahead of the evaporation wave was suppressed. They identified two parameters which had an effect on whether the test fluid reacted to depressurization by simple surface evaporation or more violent “free surface flashing” characterized by two-phase flow downstream of the surface. The first parameter was the superheat of the liquid, which was found to have a threshold value below which flashing did not occur. The other was the diameter of the test section tubing, with larger diameters requiring less liquid superheating to initiate and sustain the axial propagation of the wave. This latter result was attributed to the greater number of potential nucleation sites present at the liquid-vapour-glass interface in larger test cells.

The diaphragm burst experiments of Peterson et al. [1984] were carried out using freon 11 as a test fluid. By using Mach-Zehnder interferometry, they calculated temperature profiles for spherical regions directly below the liquid surface to gain some insight into the initial response to sudden depressurization. They concluded that instabilities together with evaporation induced a convective motion in the fluid adjacent to the interface. In addition, fluid initially at ambient temperature and pressure was subjected to varying amounts of pressure decrease. Mass flow rates out of the test section were measured. This data was used to correlate the ratio of flashing-surface mass flux to theoretical, non-flashing evaporation mass flux as a function of pressure drop and initial temperature. This ratio was found to be of order 10 or larger.

The measurement of evaporation wave velocities was the focus of an experimental study by Das et al. [1987]. In particular, the dependence of what they termed “boiling front

propagation” velocity on liquid superheating (ΔT), liquid purity and test section diameter was examined with water as the test fluid. In agreement with other researchers’ work, a linear relationship between velocity and superheat was found. Small diameters and the presence of impurities tended to decrease the measured velocity. The authors also proposed a qualitative convective model for the front propagation involving a circulating flow containing growing bubbles upstream of the wave.

The thesis work of Hill [1991] summarized in a separate publication (Hill and Sturtevant [1989]) is likely the most complete analysis of the nature of evaporation waves generated in diaphragm burst experiments. Hill used a regular fluid, refrigerant 12, and a retrograde fluid, refrigerant 114, both of which were superheated to Jakob numbers less than unity. Extensive research into the modes of wave initiation, wavefront propagation mechanisms and simplified flow models are presented in this work. Hill countered the upstream convection of liquid proposed by Das et al. [1987] as a propagation model by placing a marker fluid below the test fluid. As the wave approached, the marker fluid did not distort appreciably. According to Hill’s interpretation, the latent heat of vapourization necessary to evaporate a portion of the liquid is supplied to the wave by normal heat conduction through a thermal boundary layer between the upstream superheated liquid and the interface. A saturated liquid condition is never achieved upstream of the wave because dynamic effects in the interfacial region constantly fragment and strip away cooled liquid which is convected downstream as part of a two-phase aerosol-like flow. This allows the wave to continue to propagate until it has consumed all of the superheated liquid. It should be noted that the heat conduction described here occurs within the fluid itself and is not

supplied by an external source. Therefore, an evaporation wave in a regular fluid constitutes a partial adiabatic evaporation.

The heat conduction model of propagation with a downstream two-phase flow is clearly possible for a fluid which is only slightly retrograde, or even for a highly retrograde fluid which is only moderately superheated by the forerunner rarefaction wave. However, if the fluid is superheated to a state having a Jakob number greater than or equal to one, a complete adiabatic phase transition is possible on a molecular scale and the flow downstream of the wave will, in theory, be composed purely of vapour. Heat conduction is no longer required to supply energy to the interface, since an amount of energy exceeding the latent heat of vapourization can be given up by the superheated liquid itself. The possibility of complete evaporation waves in the n-alkane hydrocarbons has been investigated (Shepherd et al. [1990]). It was found that at the superheat limit and atmospheric pressure, the simplest fluid in this series which satisfies $Ja \geq 1$ is octane (C_8H_{18}).

In accordance with this result, Simões Moreira [1994] used a heavier alkane, dodecane, in an attempt to generate a complete evaporation wave in the customary rapid depressurization experiment. Unfortunately, he was unable to conduct many experiments at the required level of superheat due to concerns about the stress limitations of his apparatus at high initial saturation pressures. Furthermore, upstream nucleation at the wall disrupted the overall flow in the few test runs carried out at high Jakob numbers. However, the general trends in the data indicated that complete evaporation may be possible in a properly designed experiment.

3.1.2 External Flows

A somewhat different experiment that exhibits rapid adiabatic evaporation involves nozzle flows from a high pressure reservoir. Initially subcooled liquid, maintained at a high pressure, is vented through a small diameter channel or converging nozzle into a low pressure chamber. The pressure drop superheats the liquid, often leading to complex two-dimensional flashing jet flows. In most experiments of this type regular fluids such as water have been used, necessarily attaining superheats with $Ja < 1$. The resulting visual and analytical evidence suggests that the characteristics of the flow can be described by the heterogeneous and/or homogeneous nucleation of bubbles which grow to disrupt the jet. This can occur at discrete locations in a coherent liquid stream, or, at higher superheats, a large bubble population may shatter the jet completely into a wide angle spray at or near the nozzle exit.

A representative sample of these experiments includes those of Lienhard and Day [1970] in which the breakup lengths of nitrogen and water jets were investigated, and similar works by Miyatake et al. [1981] and Peter et al. [1994] using water. Senda et al. [1994] and Oza and Sinnamon [1983] have done studies with hydrocarbon fuels in automotive fuel injectors. Unlike diaphragm burst experiments, rapid evaporation was not observed to occur in a distinct wavefront by these researchers. The work of Labuntsov and Avdeev [1982], however, is an exception. Carbon dioxide was injected at near-critical initial temperatures into a low pressure environment. They assumed that the fluid reached a very high degree of superheat (close to the spinodal) and proposed that a “boiling shock” was present within the nozzle. They modeled this shock using the Rankine-Hugoniot equation for a discontinuity

and obtained general agreement with experiment in predicting the mass flux out of the nozzle.

There has been very limited study of flashing nozzle flows with retrograde fluids. Kurschat et al. [1992] expanded the fluorocarbon C_6F_{14} through a converging nozzle into a very low pressure environment (10 mbar). For low superheats, the observed jet characteristics were similar to those described for regular fluids. However, when the initial temperature of the fluid upstream of the nozzle exceeded roughly $0.7T_c$, the flow pattern changed radically. An almost radial expansion from the nozzle exit was observed. Furthermore, interferometry revealed the presence of a complicated structure of intersecting shock waves, indicating supersonic conditions in some part of the flow. At still higher initial temperatures, the shock structure persisted and complete adiabatic evaporation of the fluid was achieved between the region just downstream of the nozzle exit and the outlying shock waves. Due to the large concentration of evaporating droplets in this area, the core flow emanating from the nozzle could not be discerned in many cases. However, for initial temperatures above $0.87T_c$, shadowgraphs taken of the flow clearly showed that evaporation takes place within a very short distance from the surface of a liquid jet core based at the nozzle exit. The authors described this structure as an evaporation discontinuity.

Athans [1995] extended the work of Kurschat et al. to encompass the expansion from upstream states near the thermodynamic critical point to a low pressure reservoir. Although the fluid used by Athans was iso-octane, the results can be qualitatively viewed as similar to those of Kurschat et al. if one examines the flows at comparable reduced temperatures.

3.2. Basis of Present Analysis

Sloss [1996] designed an apparatus for the measurement and visualization of preheated fuel injection into a reservoir at atmospheric pressure. In a subset of his experiments, dodecane at a pressure of 10 bar was heated to high initial temperatures ($T_0 \approx 0.9T_c$) and injected through a simple converging nozzle. A distinct evaporation wave was observed in the flow, and the fuel evaporated within a short distance from the nozzle exit. Much of the present work revolves around this data, so a brief overview of the relevant experiments follows. For a more complete description, the reader is referred to the original document.

3.2.1. Overview of Experimental Conditions and Apparatus

In the injection experiments described by Sloss [1996], dodecane at a nominal pressure of 10 bar and temperatures up to 325°C was delivered vertically downwards through a conical converging nozzle into an inert nitrogen atmosphere at a pressure of approximately 1 bar. The nozzle had an exit diameter of 0.21 mm and an angle of 90° as shown in Figure 3.1. The fuel was pressurized inside a bladder accumulator using nitrogen as the pressurizing gas. Physically separating the fuel from the nitrogen by means of the accumulator's membrane was deemed necessary to avoid dissolving any gas into the fuel. It is well known that gas coming out of solution during depressurization can create heterogeneous nucleation sites which may have a marked influence on nozzle flows, especially at large gas concentrations (Simoneau [1981]). This effect was therefore controlled by the chosen pressurization system.

Heating of the fuel to its desired temperature was accomplished inside a furnace immediately above the nozzle and injection chamber. Fuel flow to the injection chamber was controlled by a valve immediately upstream of the nozzle.

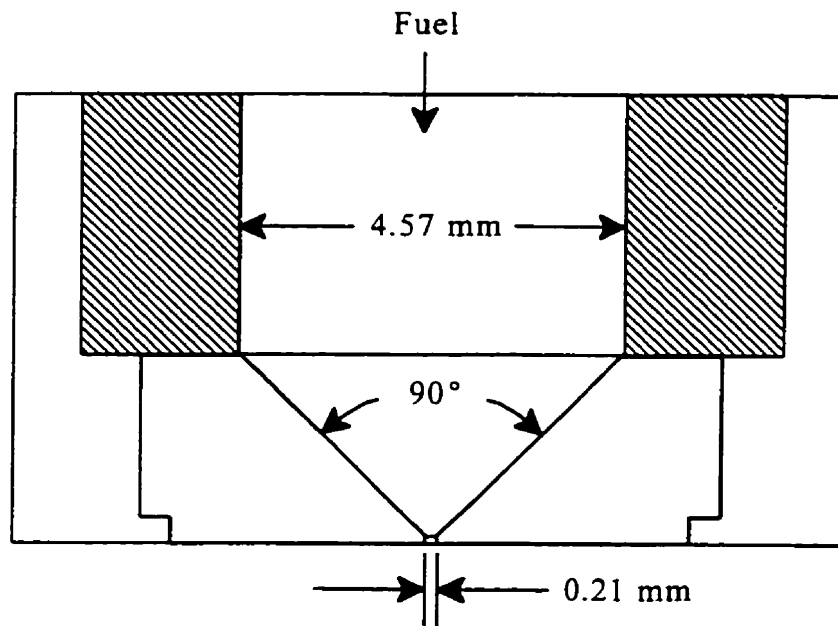


Figure 3.1. Dimensions of the conical converging nozzle.

3.2.2 Instrumentation

The injection temperature of the fuel was measured with a thermocouple located within the nozzle body upstream of the converging region. Fluid pressure was also measured through a tap at this location (approximately 25 mm above the nozzle exit). Fuel flow rates were measured with a rotameter in the fuel line between the bladder accumulator and furnace. For each individual experiment, a high contrast black and white photograph was taken of the flow.

3.2.3. Experimental Procedure

Once the heated components and pressurized fuel inside the furnace had reached the set point temperature for a given injection, the valve upstream of the nozzle was opened manually. The photography and data acquisition equipment was triggered when the nozzle pressure transducer signal registered above a chosen threshold value. An appropriate timing delay of roughly 300 ms was instituted so that initial pressure fluctuations propagating through the system upon the opening of the valve had disappeared when the picture was taken. The temperature and pressure transducer signals were recorded continuously from 1s before this event to 1s after. As soon as the picture had been taken a spray removal system was raised within the injection chamber. This served to collect the liquid and/or vapour fuel, minimizing deposition on the chamber walls and windows. When the rotameter level was judged to have reached a steady value (several seconds later), it was read to get a mass flow rate measurement.

3.1.4. Experimental Results

At injection temperatures between 20°C ($0.45T_c$) and 251°C ($0.80T_c$), axial liquid jets were observed. Downstream of the nozzle exit, these jets were broken up into droplets due to the growth of surface instabilities. The break up length was found to decrease with increasing temperature. Flashing jet flows occurred at injection temperatures between approximately 261°C ($0.81T_c$) and 303°C ($0.88T_c$). At low temperatures in this range, a coherent liquid jet emerged from the nozzle. Bubbles nucleated and grew to expand the jet into a wide angle spray at a location downstream of the nozzle exit. The intact length of the

jet decreased to zero and the outer cone angle of the spray increased substantially (from 15° to 90°) as the injection temperature was raised. The results of interest here are those in which a coherent evaporation wave can be discerned in the flow. This phenomenon was regularly observed for injection temperatures above $0.88T_c$. Figure 3.2 shows one such injection, corresponding to an initial temperature of 311°C ($0.89T_c$). The region close to the nozzle exit is enlarged in Figure 3.3(a) to show its characteristics more clearly. A schematic which highlights the features of the flow is shown in Figure 3.3(b). It can be seen that a dense, liquid core of essentially conical shape is based at the nozzle exit. This core appears to represent an almost discontinuous surface at which the liquid is rapidly evaporating. The fine scale structure of the surface region cannot be distinguished in the photographs; plainly it is not a smooth liquid-vapour interface since the downstream flow appears to be a two-phase mixture. Therefore, describing the surface region as a discontinuity is a convenient idealization which is only justified in comparison with the scale of the global flow. All of the fuel droplets in the mixture region completely evaporate within a few nozzle diameters of the liquid core, leading to a pure vapour state. Much further downstream the recondensation of vapour is visible, producing a fog cloud.

Figure 3.4 shows Sloss's data for the dependence of the liquid core length on the injection temperature. The core length becomes shorter as the initial temperature is increased. Evaporation waves were not observed for initial temperatures below approximately 303°C , although it is possible that denser droplet clouds surrounding the nozzle at slightly lower temperatures obscure discontinuities in the photographs.

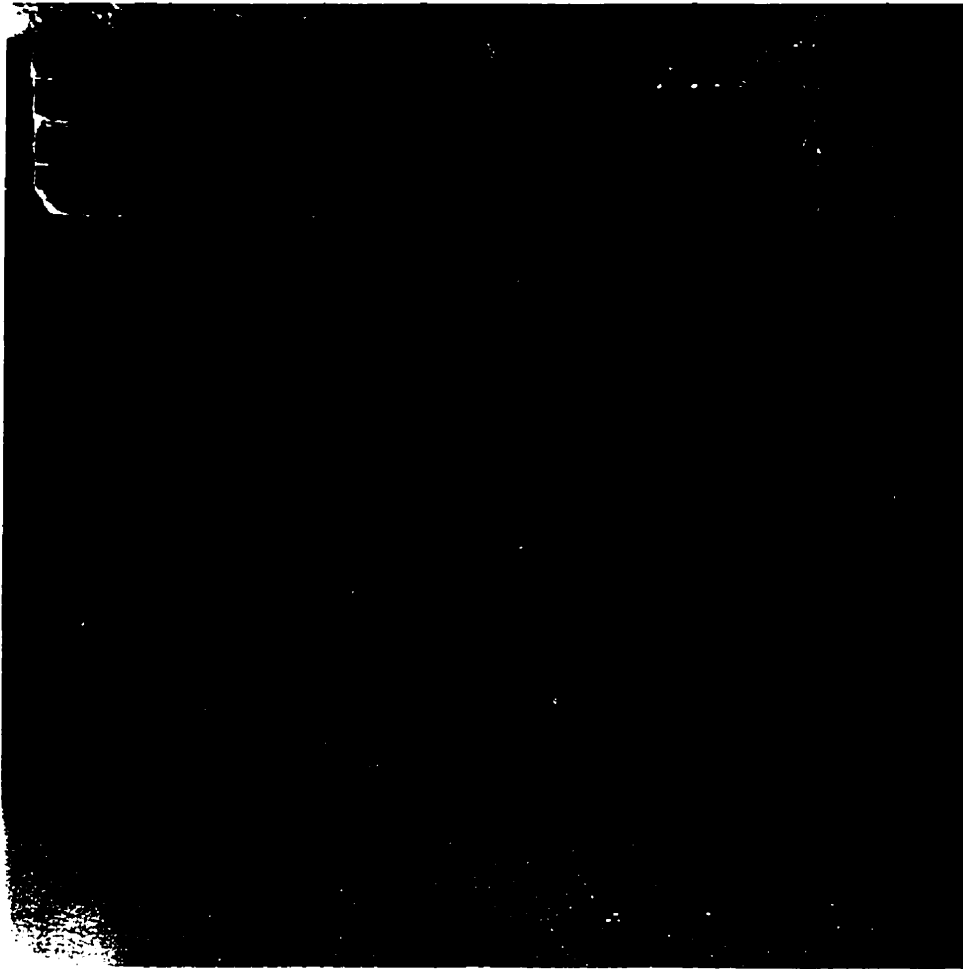
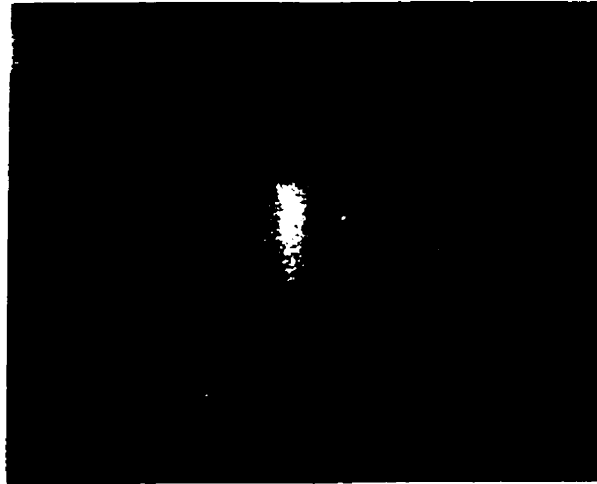
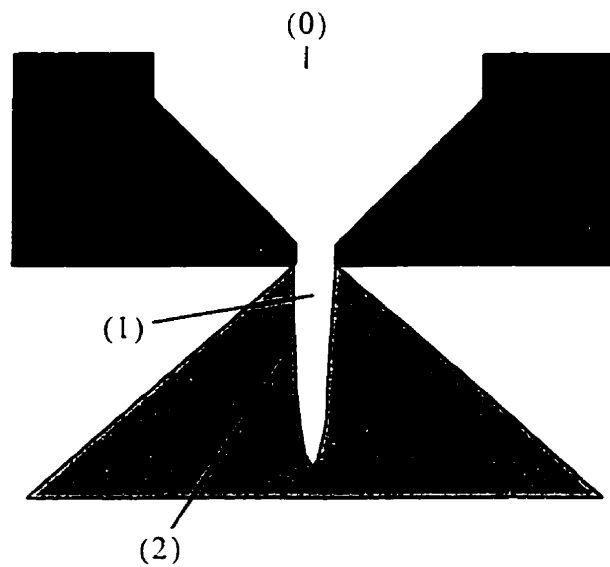


Figure 3.2. Injection of dodecane at 311°C ($0.89T_c$).



(a)



(b)

Figure 3.3. (a) Photographic enlargement of the nozzle exit region for an injection temperature of 311°C. (b) Cross-sectional schematic of the flow structure, including the nozzle interior.

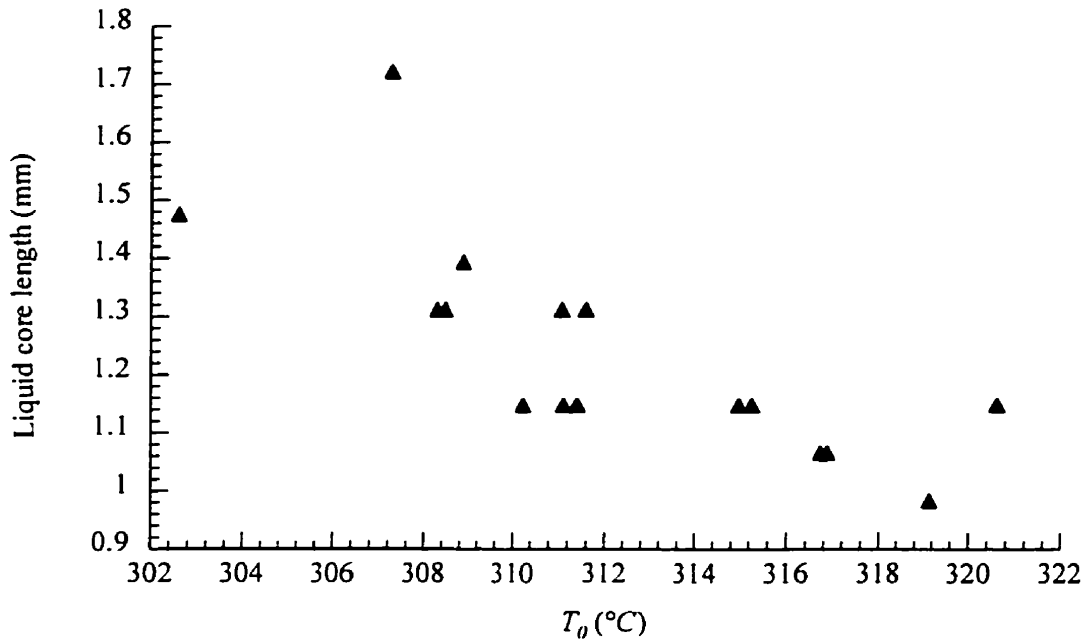


Figure 3.4. Temperature dependence of liquid core length for dodecane injections exhibiting an evaporation discontinuity.

3.3. Flow Model

In order to model the thermodynamic states attained by the fluid throughout its expansion, it is necessary to have a satisfactory description of the various flow regimes which can be identified in the photographs. The expansion can be broken into three stages: liquid acceleration through the nozzle, rapid evaporation across a flow discontinuity, and outward flow approaching the ambient pressure of the injection chamber.

3.3.1. Nozzle Flow

In the absence of heat transfer from the nozzle walls, and neglecting viscous effects, the fluid's acceleration through the nozzle can be considered to be an isentropic

depressurization. The liquid dodecane follows an isentropic path from an almost stagnant state (0) above the nozzle to a lower pressure state (1) immediately preceding the evaporation discontinuity (see Figure 3.3(b)). In so doing, the fluid follows a metastable isentrope as it crosses the saturation boundary and is, therefore, “storing” internal energy which is used later to effect a transition to an equilibrium state via phase change. Precisely how much the liquid becomes superheated before entering the flow discontinuity is an issue related to the closure conditions of the model.

3.3.2. *Evaporation Discontinuity*

Of primary importance in the overall model is the description of the evaporation process. Accordingly, it is necessary to determine the possible equilibrium states (2) downstream of the wave corresponding to a given upstream metastable state (1). The starting point in formulating a solution is to examine the conservation equations of mass, momentum and energy across the discontinuity. Consider a control volume enclosing a section of the stationary evaporation front, as shown in Figure 3.5. It is assumed that the front represents a true discontinuity in the sense that the control volume may be chosen to be arbitrarily thin and still capture all of the structure inside the volume. This idealization allows fluxes through the short edges to be neglected in the analysis. Fluid enters the control volume with velocity u_1 , pressure P_1 , density ρ_1 , and specific enthalpy h_1 . The velocity has components normal and tangential to the control surface, labeled u_{1n} and u_{1t} , respectively. Properties are similarly defined for the downstream side of the surface, with the subscript 2. Per unit surface area, the balance equations for mass, momentum and energy simplify to

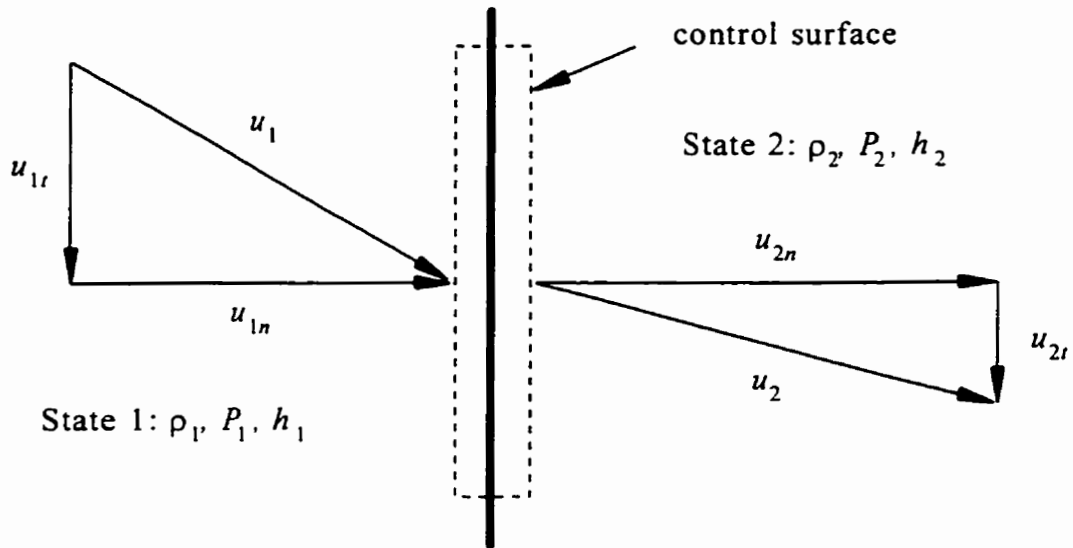


Figure 3.5. Control surface enclosing the evaporation discontinuity.

$$\rho_1 u_{1n} = \rho_2 u_{2n} = i \quad (3.1)$$

$$P_1 + \rho_1 u_{1n}^2 = P_2 + \rho_2 u_{2n}^2 \quad (3.2a)$$

$$u_{1t} = u_{2t} \quad (3.2b)$$

$$h_1 + \frac{u_{1n}^2}{2} = h_2 + \frac{u_{2n}^2}{2} \quad (3.3)$$

where i is the local mass flux. An additional condition that must be satisfied is the second law of thermodynamics:

$$s_2 \geq s_1 \quad (3.4)$$

Figure 3.5 is drawn in the plane of the velocity vectors. Thus equations (3.2a) and (3.2b) represent the conservation of normal and tangential momentum, and there is no

velocity component in the third (tangential) coordinate direction on either side of the discontinuity. Equations (3.1) to (3.4) are identical in form to the classical relations used to calculate oblique shock transitions in gas dynamics. Neglected in the formulation presented are heat transfer across the control surface, viscous effects, and the effects of surface tension. As pointed out by Thompson [1988] in his discussion of the shock relations, the changes in velocity and temperature across a discontinuity can be quite large. As such, viscous stresses and heat flux *within* the control volume cannot be negligible, and the shock relations are inexact. However, these effects can be neglected *at* the control surface. In order to justify the inviscid and adiabatic approximations at the control surface, it must be assumed that the control surface can be selected in such a way that the gradients of velocity and temperature at the surface are sufficiently small without violating the condition of small thickness. The effect of surface tension on the pressure ratio across the discontinuity is expected to be dominated by a large change in fluid momentum and is not taken into account.

Several useful expressions can be obtained by combining equations (3.1), (3.2a) and (3.3). The first two of these can be combined to give

$$\frac{P_2 - P_1}{v_2 - v_1} = -i^2 \quad (3.5)$$

where v is the specific volume, equal to the reciprocal of the density. This expression describes a line in the pressure-specific volume (P - v) plane and is called a Rayleigh line. All three of the designated conservation equations can be combined to produce the Rankine-Hugoniot equation:

$$h_2 - h_1 = \frac{1}{2}(v_1 + v_2)(P_2 - P_1) \quad (3.6)$$

Together with an equation of state that relates enthalpy to specific volume and pressure, equation (3.6) can be used to plot a P - v curve of possible downstream states (2) for a given upstream state (1). A curve calculated in this manner is termed a Hugoniot. In the case of a simple shock wave, the functions $h_2(P_2, v_2)$ and $h_1(P_1, v_1)$ are identical and the Hugoniot curve must therefore pass through the point (v_1, P_1) . However, since state (1) is a metastable liquid state and state (2) is assumed to be an equilibrium vapour or two-phase state, the functions are not the same. Then the Hugoniot is offset from the point (v_1, P_1) on a P - v diagram (Figure 3.6). As a result of this observation, an analogy is often drawn between the evaporation process described here and other flows which are modeled as adiabatic discontinuities, such as a flame front. Differences in the properties of the reactant and product species result in different enthalpy functions.

A Rayleigh line can be drawn from the upstream state (1) to intersect the Hugoniot which represents possible downstream states. Each intersecting Rayleigh line can be interpreted as containing information about the normal flow velocities on either side of the discontinuity. In particular, the slope of a Rayleigh line allows one to calculate a mass flux across the discontinuity. From equation (3.5) it can be seen that a Rayleigh line with a positive slope leads to an imaginary mass flux. For this reason, the Hugoniot curve is plotted as a dashed line in the affected region to indicate that these downstream states are non-physical.

As a consequence of this, the Hugoniot is separated into two branches. The upper branch of the curve corresponds to solutions for compression discontinuities and is termed the detonation branch. In relation to liquid-vapour phase transitions, the detonation mode has

been considered as a mechanism for the propagation of vapour explosions by Fowles [1989], among others. However, the evaporation waves generated in diaphragm burst experiments are known to sustain a measurable pressure drop between the upstream and downstream states (see, for example Hill [1991]). Therefore the lower Hugoniot branch associated with expansion discontinuities provides a more appropriate solution for the analogous nozzle flows considered here. Another analog which involves a pressure drop is that of a flame propagating in a combustible mixture (i.e. a deflagration wave). This region of the Hugoniot curve is therefore called the deflagration branch.

Two limiting Rayleigh lines can be drawn from a given state (1) to the deflagration Hugoniot. A horizontal, constant-pressure line, (1) to (2a) on Figure 3.6, gives a hypothetical solution in which the mass flux i across the discontinuity is zero. The line of maximum negative slope which is just tangent to the Hugoniot at point (2b) corresponds to a maximum local mass flux. This point of tangency is called the lower Chapman-Jouguet (CJ) solution. Hereinafter the term CJ point will be used to refer to the lower CJ point, distinct from the analogous location on the detonation branch of the Hugoniot. It can be shown that the CJ solution is a point of maximum entropy production on the deflagration Hugoniot, and that the isentrope passing through the CJ point is necessarily tangent to the Hugoniot curve. For flows which are strictly normal to the discontinuity, the CJ point represents a downstream state that has sonic velocity. In other words, the outflow from the discontinuity has a Mach number $Ma_2 = u_2/c_2$ of one. Determining the CJ point requires a numerical root-finding technique in which the velocity u_2 obtained from a Rayleigh line is compared to the

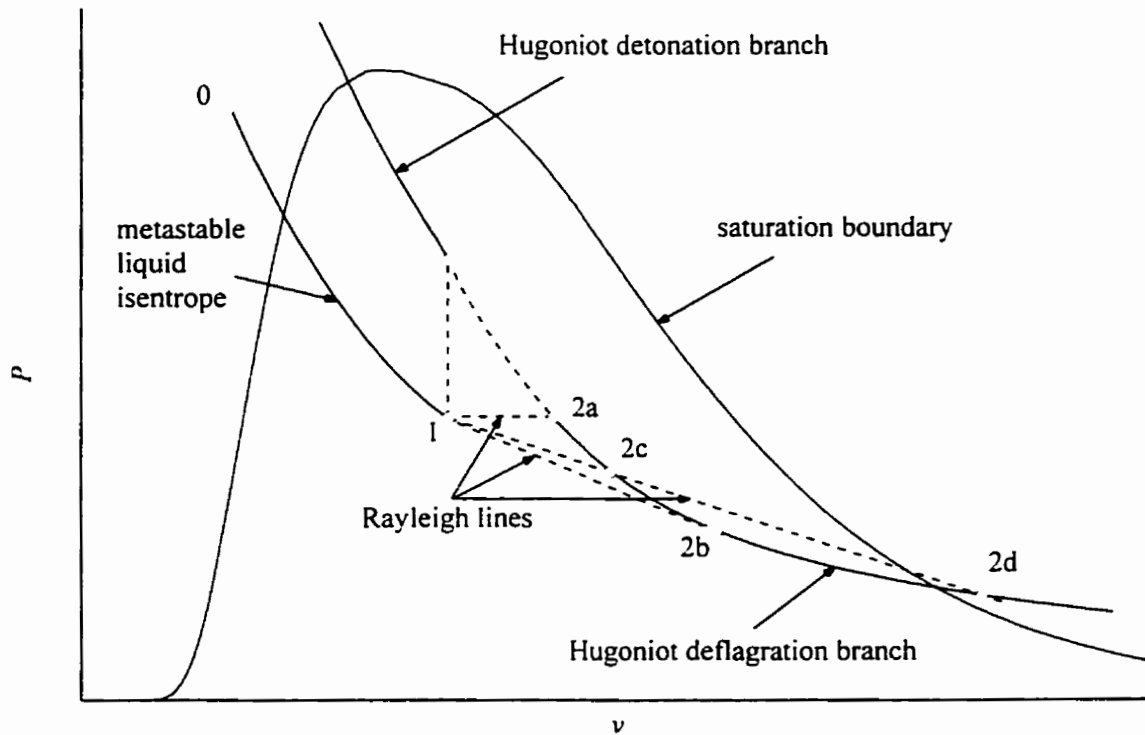


Figure 3.6. Thermodynamic model for an evaporation discontinuity. Properties jump from a metastable liquid state (1) to a state (2) on the equilibrium Hugoniot. State (2a): zero velocity, weak deflagration; state (2c): subsonic velocity, weak deflagration; state (2b): sonic velocity, CJ deflagration; state (2d): supersonic velocity, strong deflagration. The process from (0) to (1) represents the isentropic expansion through the nozzle.

appropriate single-phase or two-phase sound speed, c_2 . An alternate approach is to search for a maximum in the mass flux along the Hugoniot.

Other Rayleigh lines intersect the Hugoniot at two points, such as the one passing through (2c) and (2d). Again, considering purely normal flows, the state with higher pressure (2c) corresponds to a subsonic outflow ($Ma_2 < 1$) from the discontinuity and is called a weak deflagration. State (2d) corresponds to supersonic outflow ($Ma_2 > 1$) and is called a strong deflagration. It can be shown that strong deflagration solutions do not exist for

combustion discontinuities, based on wave structure considerations (Williams [1985]). The same claim is made for evaporation discontinuities by Kurschat et al. [1992], as an additional boundary condition is deemed necessary for a stable strong deflagration. In the case of an oblique discontinuity, the analysis is complicated by the tangential velocity component. However, it is suggested that the limiting case for stability is still that the normal component of velocity is at the CJ value.

It should be pointed out that the conservation equations (3.1) to (3.3) do not specifically have to apply to a discontinuity; in fact, the same equations would hold true across a finite control volume drawn in a constant area duct or other normal plane flow. Then the subscript “ n ” can be dropped from the velocity terms and the tangential velocity is by definition zero. Indeed, an identical treatment is used by both Hill [1991] and Simões Moreira [1994] to describe the downstream states of the axially propagating evaporation waves obtained in their diaphragm burst experiments. These waves were observed to be relatively thick, on the order of 1 to 2 cm.

3.3.3. *External Flow*

Like the flow through the nozzle, the flow downstream of the discontinuity can be assumed to be isentropic if viscous effects, heat transfer and mixing with the surrounding nitrogen atmosphere are neglected. State (2) is taken to be at equilibrium, and the flow is assumed to follow an equilibrium isentrope.

Following the work of Kurschat et al. [1992], additional simplification results if the flow is treated as purely radial. Then the conical, metastable liquid core is replaced in the

model by a cylinder of equivalent surface area, and the discontinuity is no longer considered to be oblique. Treating the external flow as one-dimensional in this fashion represents a substantial idealization of what is observed in the photographs. Clearly, the wide angle sprays (approximately 110°) under analysis must have a significant axial velocity component. However, a fully two-dimensional model would greatly complicate the mathematics of the overall solution without providing much additional insight into the thermodynamic effects being considered.

Leaving aside the issue of uniquely determining state (1) as a function of the injection temperature, it can be seen that a family of possible solutions exists depending on which state (2) on the Hugoniot curve is chosen for a given state (1). It is also evident that this family of solutions can be divided into two groups. In one solution group, the discontinuity is a weak deflagration, corresponding to a subsonic outflow. In the other, sonic conditions are achieved and state (2) is the CJ state. Each type of solution has very different implications for the nature of the flow downstream of the discontinuity, as can be seen from a manipulation of the conservation equations for a radial, isentropic expansion. The steady flow continuity equation is

$$\rho \frac{du}{dr} + u \frac{d\rho}{dr} + \frac{\rho u}{r} = 0 \quad (3.7)$$

and conservation of momentum yields

$$u \frac{du}{dr} = -\frac{1}{\rho} \frac{dP}{dr} \quad (3.8)$$

The isentropic condition can be expressed as

$$dP = c^2 d\rho \quad (3.9)$$

Using equations (3.9) and (3.8) to eliminate the term $d\rho/dr$, equation (3.7) can be simplified to

$$\left(1 - \frac{u^2}{c^2}\right) \frac{du}{dr} + \frac{\rho u}{r} = 0 \quad (3.10)$$

From this expression, it is clear that the sign of du/dr will be negative at the discontinuity and the flow will slow down as the radius increases for a subsonic state (2) (i.e. $u < c$). Equations (3.8) and (3.9) imply that both the pressure and density start out as increasing functions of the radius in the subsonic case.

If the flow is sonic (i.e. $u=c$) at state (2), then the variation of u with respect to r at the discontinuity is indeterminate in equation (3.10). Therefore we consider small perturbations from the CJ velocity. A small perturbation that decreases the velocity will result in the subsonic downstream flow described above. However, a perturbation which marginally increases the velocity produces a supersonic condition (i.e. $u > c$). Then the sign of du/dr in equation (3.10) is positive at the discontinuity and the pressure and density will begin as decreasing functions of the radius.

The question to be considered is whether or not the initial trends followed by the pressure, velocity and density will hold true throughout the expansion. The critical parameter is the functional dependence of the sound speed on the radius in equation (3.10). To examine this dependence, consider the following isentropic flow relation derived by Thompson [1988]:

$$\frac{du}{u} = \frac{dMa \cdot Ma}{1 + (\Gamma - 1)Ma^2} \quad (3.11)$$

Here Γ is the so-called fundamental derivative, which may be related to the other thermodynamic variables involved through two expressions:

$$\Gamma = \frac{v^3}{2c^2} \left(\frac{\partial^2 P}{\partial v^2} \right) \quad (3.12)$$

$$\left(\frac{\partial c}{\partial P} \right)_s = \frac{v}{c} (\Gamma - 1) \quad (3.13)$$

Equation (3.11) indicates that for a subsonic flow, the Mach number will decrease with decreasing fluid velocity as long as $\Gamma > 0$. This will be true as long as isentropes are concave upwards in the P - v plane, as shown by the second derivative in equation (3.12). Since all equilibrium isentropes in the P - v - T domain under consideration meet this criteria, the initially subsonic flow will remain subsonic and slow down as the radius increases. It is interesting to note that for certain high molecular weight fluids, Γ is negative over a finite region of P - v - T space near the critical point. The formation of rarefaction shock waves is associated with negative Γ behaviour (Thompson [1988]).

In the supersonic case, the Mach number is guaranteed to monotonically increase with velocity for $\Gamma \geq 1$. This will also be true for $0 < \Gamma < 1$ if the Mach number is sufficiently small to keep the denominator on the right hand side of (3.11) positive. In the two-phase region and in the superheated vapour region near the saturation boundary, calculations with the MSBR equation of state reveal that the speed of sound, c , can become a decreasing function of pressure (see, for example, Figure 2.14). Then equation (3.13) requires that the fundamental derivative be less than one for certain portions of the equilibrium isentrope of Figure 2.13. A rough calculation with equation (3.13) and the data shown in Figures 2.13

and 2.14 gives values of Γ of 0.8 and 0.9 for the two-phase and single phase states adjacent to the vapour saturation boundary. With this result, it is conceivable that the Mach number may begin to decrease during the expansion. In spite of this possibility, it is clear from equation (3.11) that the supersonic flow cannot make an isentropic transition to a subsonic condition unless Γ drops below zero. Therefore, the trends of increasing velocity and decreasing pressure and density continue as the fluid expands from an initial CJ state (2).

Thus isentropic subsonic flows remain subsonic and isentropic supersonic flows remain supersonic. However, a theoretical exception to this must be noted for the flows considered here. It is clearly possible that for some calculations, state (2) may lie very close to the saturation boundary, and that the isentropic expansion may cross this boundary. Γ abruptly becomes equal to $-\infty$ at this point due to the discontinuity in the speed of sound. Therefore an isentropic transition from subsonic to supersonic flow or vice versa becomes conceivable in this particular situation. The assumption has been made here that non-equilibrium effects smooth the sound speed jump at the boundary without causing the other thermodynamic properties to deviate appreciably from their equilibrium values. Therefore, these singular cases are explicitly ignored even though the equilibrium assumption is maintained.

In order to complete the model, it is necessary to specify an end state for the expansion. The ambient pressure must be approached by an unconstrained isentropic flow. Therefore, this pressure is an appropriate boundary condition. For a subsonic state (2), this presents no particular problem. As the fluid flows radially outwards, its initial momentum is converted to pressure and its velocity decreases. For the radial isentropic expansion

considered here, conservation of mass dictates that the flow will stagnate completely as the radius approaches infinity. Therefore, a convenient idealization is to consider the injection chamber to be semi-infinite. The ratio of the radius at the chamber wall to that of the nozzle is about 1500:1 for the experimental conditions, indicating that a stagnation condition may be approximately achieved.

Locating the end state (3) of the expansion raises the question of which of the possible subsonic states (2) downstream of the discontinuity is appropriate for a given state (1). It is precisely the solution which has an initial momentum such that the flow will stagnate isentropically to the pressure of the surrounding atmosphere. One method of finding this state (2) involves the integration of the momentum equation (3.8) along an isentrope:

$$\int_2^3 u du = - \int_2^3 \frac{dP}{\rho} \quad (3.14)$$

With $u_3=0$, this simplifies to

$$u_2 = \sqrt{2 \int_2^3 \frac{dP}{\rho}} \quad (3.15)$$

Then the location of state (2) can be found by satisfying the condition that the velocity u_2 obtained from the Hugoniot and a chosen Rayleigh line be the same as that calculated from equation (3.15), where the lower limit of integration corresponds to the pressure on the Hugoniot curve. A schematic of the subsonic flow model is shown in Figure 3.7, and a P - v diagram which indicates the relevant thermodynamic states is shown in Figure 3.8.

The solution procedure for an expansion from a CJ state is quite different. With no possibility of the fluid reaching a subsonic state isentropically, the supersonic flow downstream of a sonic discontinuity is in the incongruous situation of having ever-increasing

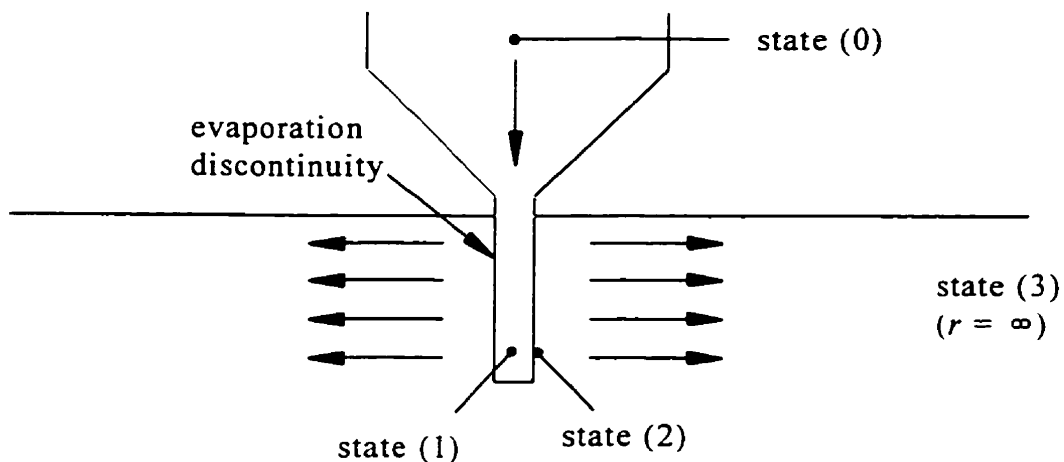


Figure 3.7. Model for subsonic flow downstream of the evaporation discontinuity.

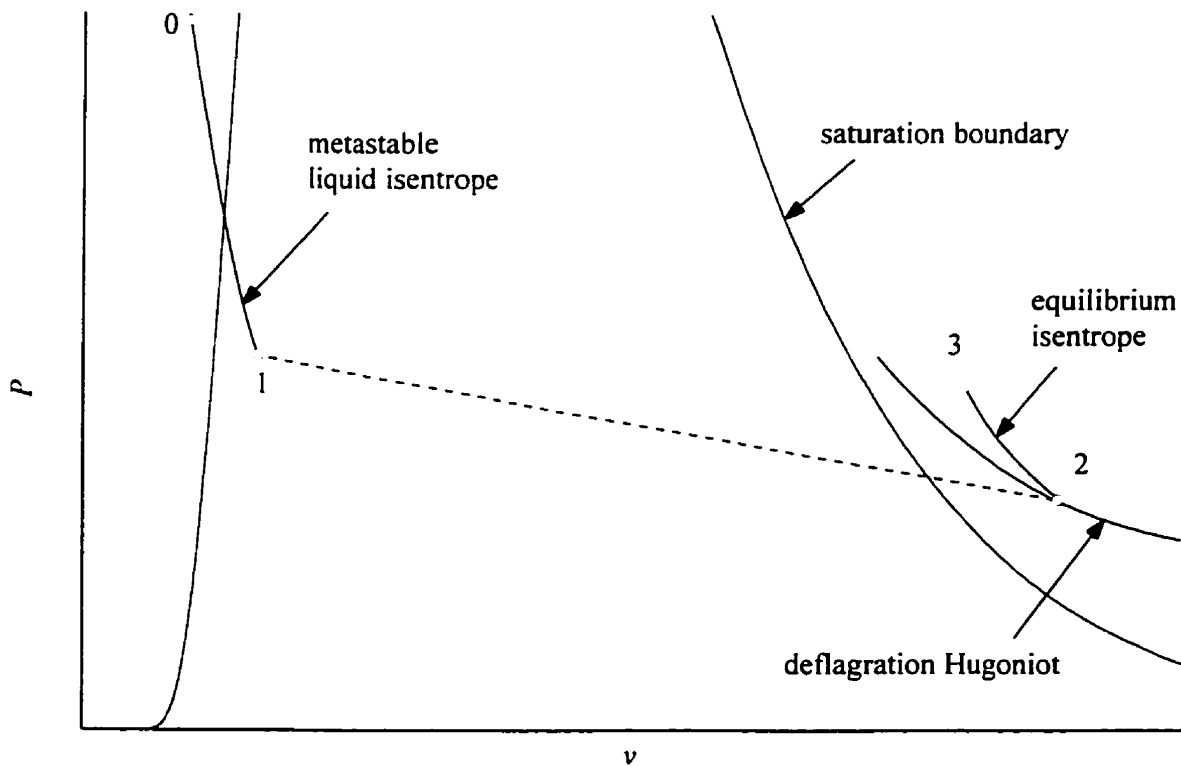


Figure 3.8. Thermodynamic states corresponding to the subsonic flow model shown in Figure 3.7.

velocity and ever-decreasing pressure. As a result, the fluid will eventually become overexpanded with respect to the injection chamber pressure. The only means by which the flow may become subsonic and match this pressure is through a second, non-isentropic discontinuity. For the radial expansions considered, this will take the form of a stationary normal shock wave. The problem then centers on calculating the location and strength of this shock wave. Specifically, it is necessary that the subsonic downstream state of the shock be such that isentropic flow from the shock outwards will stagnate at the ambient pressure.

Flow from the evaporation discontinuity to the shock wave can be described in similar fashion to equations (3.14) and (3.15). Designating the upstream shock state as (2'), these become

$$\int_2^{2'} u du = - \int_2^{2'} \frac{dP}{\rho} \quad (3.16)$$

$$u_{2'} = \sqrt{- \int_2^{2'} \frac{dP}{\rho} + u_2^2} \quad (3.17)$$

The shock transition can be calculated using the standard shock relations. The shock adiabat in the P - v plane passes through the point $(v_{2'}, P_{2'})$ and the appropriate downstream state (2'') on this adiabat is uniquely determined because the velocity $u_{2'}$ is known from equation (3.17). This is equivalent to saying that the slope of the Rayleigh line from the state upstream of the shock front is a known quantity. Extending the solution to the end state (3) is then identical to the procedure for the subsonic evaporation discontinuity. A schematic of a CJ solution is shown in Figure 3.9. In the corresponding P - v diagram (Figure 3.10), discontinuous transitions are represented by dotted Raleigh lines.

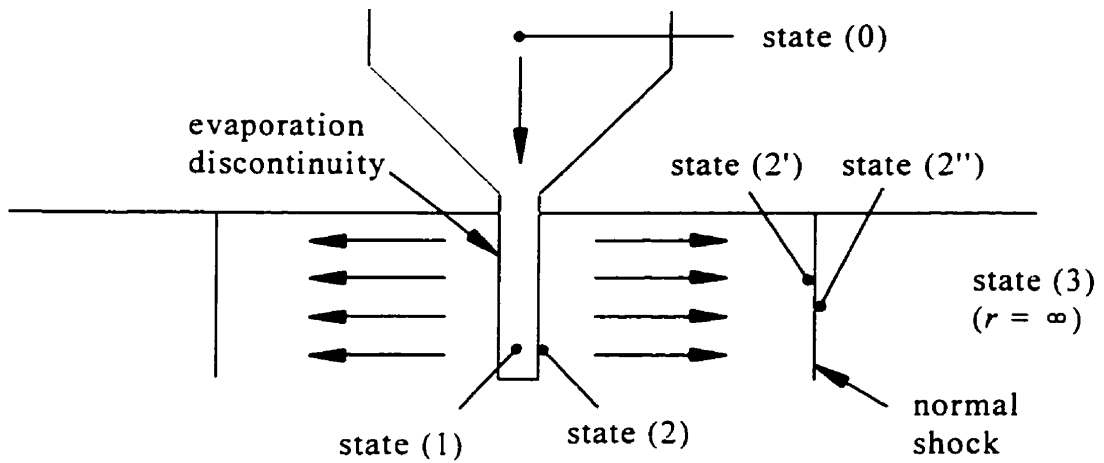


Figure 3.9. Model for sonic flow at point (2), the downstream state of the evaporation discontinuity.

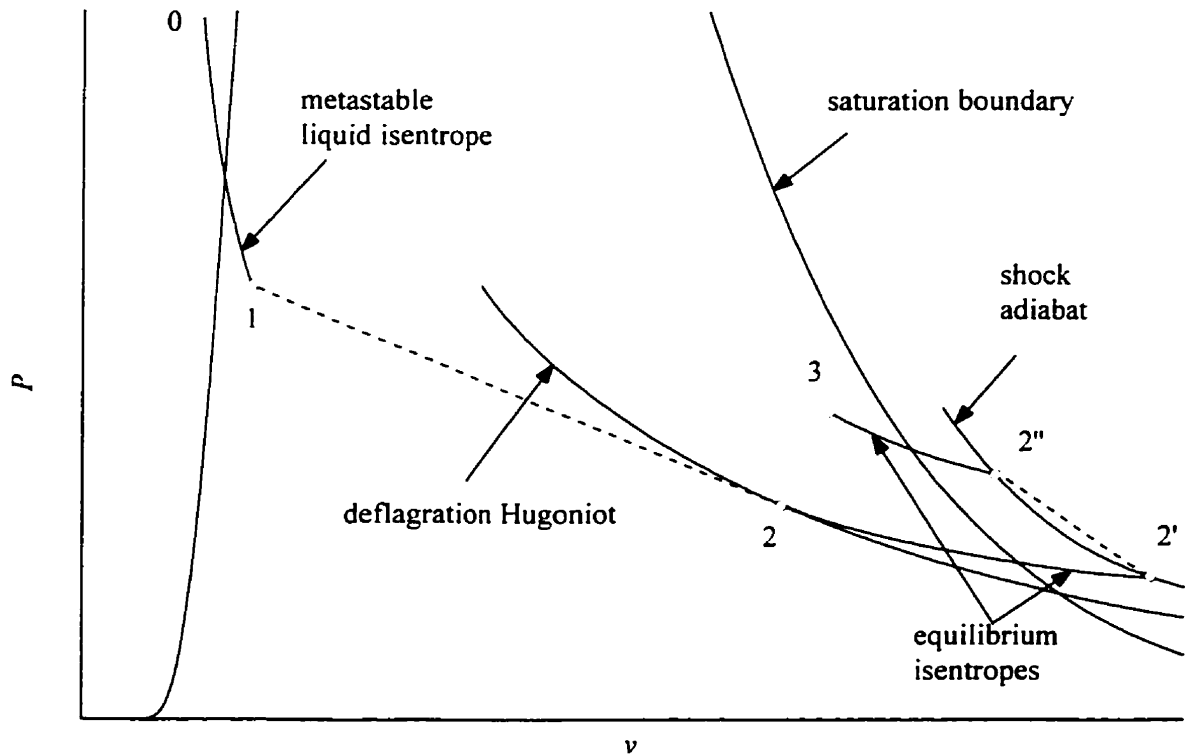


Figure 3.10. Thermodynamic states corresponding to the CJ flow model shown in Figure 3.9.

3.3.4. Comments on Computational Procedure

Due to the complexity of the MSBR equation of state, it is not possible to calculate the two solution types analytically. As a result, the integration in expressions such as (3.15) must be performed numerically, and finding the overall solution in each case is an iterative process. For a subsonic solution, an initial guess of the pressure P_2 on the Hugoniot is made and adjusted until P_2 and u_2 are consistent with isentropic flow to stagnation at pressure P_3 . This technique is similar to a shooting method. Similarly, in calculating a CJ solution it is necessary to guess and adjust the upstream pressure of the shock wave P_2 until the stagnation boundary condition is met. In the next section a means of dividing the metastable liquid region into areas in which state (1) produces either a subsonic solution or a CJ solution for the injection temperatures of interest is discussed. Based on this division, some calculations are performed to predict the temperatures at which complete adiabatic evaporation is expected and the results are presented. Finally, a means of selecting state (1) at each temperature is discussed with corresponding results.

4. RESULTS

4.1. Solution Domain

Before directly modeling a particular experiment, it is useful to consider which of the two solution types is valid for the range of metastable liquid states (1) that may be reached as the liquid dodecane is isentropically depressurized in the converging nozzle. It is also instructive to determine the nature of a series of solutions originating from various states lying on a common isentrope.

The region *abfe* of Figure 4.1 represents the range of metastable states that the liquid may attain from initial state (0) locations in the temperature range 303-321°C and at an initial pressure of 10 bar. The line bounding this area on the left is a metastable isentrope extending from the (0) state at 303°C, while the boundary on the right is the metastable isentrope passing through the (0) state at 321°C. The area is bounded above by the liquid saturation boundary and below by an isobar at the injection chamber pressure. Area *cdfe* encloses all (1) states that correspond to strictly subsonic solutions. The area above this, *abdc*, corresponds to states for which only CJ solutions are possible. At an almost constant pressure of roughly 1.21 bar, line *cd* divides the two solution domains. Model calculations have been performed for a variety of (1) states of interest and the numerical results are presented in Appendix A. A graphical summary of some of these results is displayed here and in section 4.2.

The details of the solutions starting at state (1) locations on the isentrope labeled *gh* in Figure 4.1 are displayed in Figures 4.2 through 4.5. The subsonic, weak deflagration

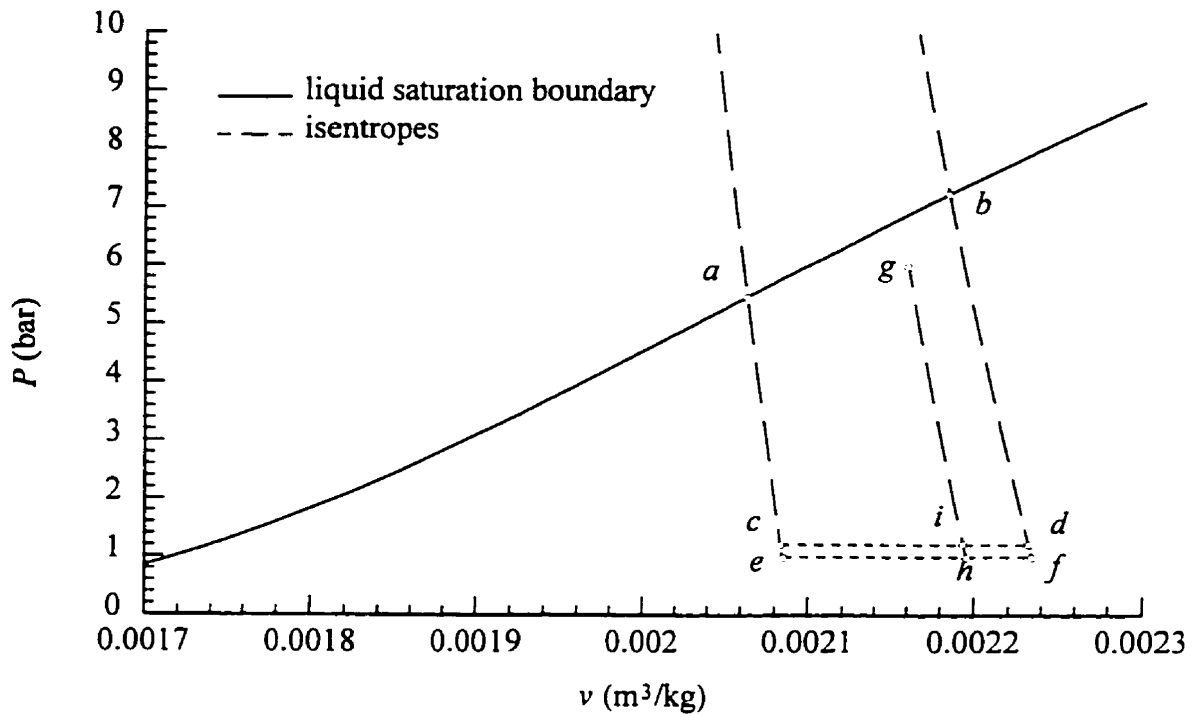


Figure 4.1. Domain of possible (1) states achievable by isentropic expansion from the experimental (0) states. Region *abc*: state (1) yields a CJ solution. Region *cdf*: state (1) yields a subsonic solution.

solutions are shown in Figures 4.2 and 4.3. In the first of these two figures, the dashed line represents the CJ pressure on the Hugoniot drawn for each state (1) in the range of pressures between 1 and 1.21 bar. The solid curve shows the Hugoniot (2) states which satisfy the stagnation boundary condition. It can be seen that for a state (1) at exactly 1 bar (case *h* of Figure 4.1), the appropriate Hugoniot state (2) is at the same pressure. The Rayleigh line construction then yields a mass flux of zero across the discontinuity, and P_2 is identical to the stagnation pressure P_3 in this case. As the pressure at state (1) increases, the Hugoniot state (2) gradually converges to the CJ point. In order to clarify the relationship between a given

(1) state and its corresponding (2) state, the Hugoniot states (2) for cases *h* and *i* of Figure 4.1 have been given the same labels in Figure 4.2.

Figure 4.3 is a plot of the velocity (u_1) of the metastable liquid normal to the evaporation discontinuity implied by the Rayleigh lines drawn to the Hugoniot solutions. If one considers a frame of reference in which the upstream liquid is stationary, this velocity can be viewed as the evaporation wave speed. Again, the labels *h* and *i* are used to indicate the velocities corresponding to the cases shown in Figure 4.1. The wave speeds increase with increasing pressure P_1 because v_1 stays essentially constant and the slope of the Rayleigh line increases as state (2) moves closer to the CJ point on the corresponding Hugoniot.

Figures 4.4 and 4.5 describe CJ solutions. As before, the dashed line in Figure 4.4 represents the CJ pressure (2) corresponding to each metastable liquid state (1). The increase in the slope of this line occurs when the CJ point becomes a two-phase mixture state. The solid curve is the pressure just upstream of the normal shock wave (2'), and the dotted curve is the pressure (2'') downstream of the shock. At the cutoff pressure of about 1.21 bar, the states (2') and (2'') are coincident with the CJ point. In this limiting case, a zero strength shock is present, coincident with the evaporation discontinuity. As the pressure of state (1) increases, the pressure ratio across the shock wave increases and the downstream pressure (2'') gets closer to the stagnation pressure of 1 bar. The labels *i* and *g* on the figure indicate the CJ (2) states corresponding to the identically labeled cases shown in Figure 4.1. Figure 4.5 shows the evaporation wave speeds for the CJ solutions of Figure 4.4. A trend of higher wave speeds with increasing state (1) pressure is evident.

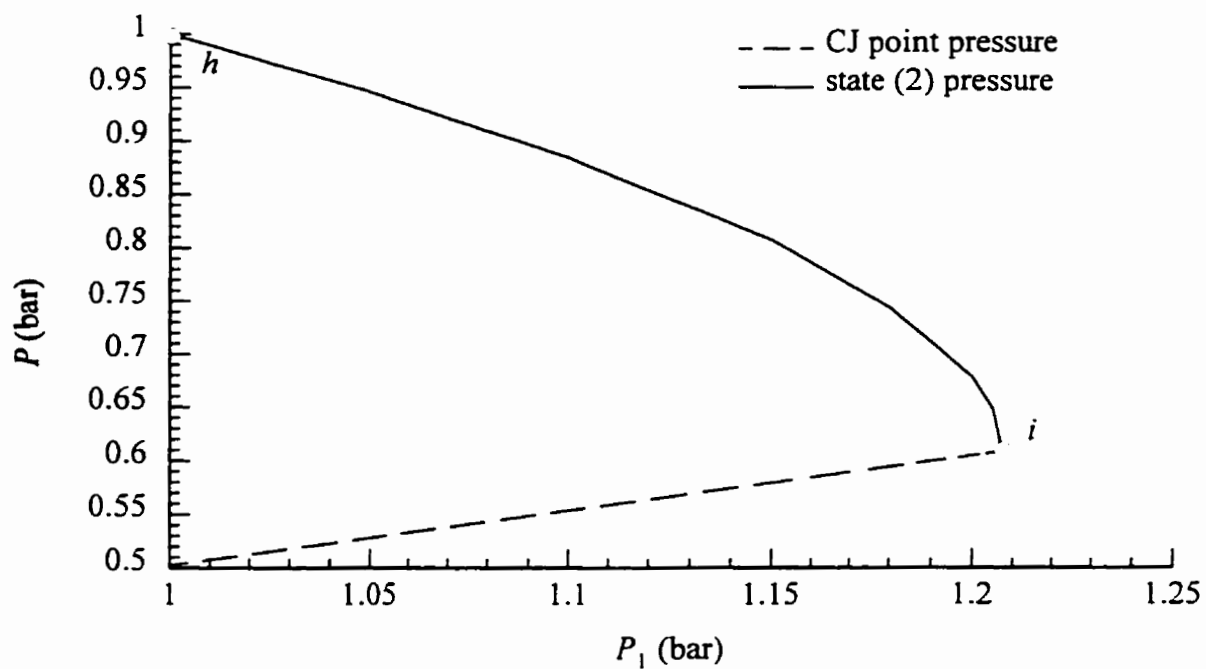


Figure 4.2. Subsonic solutions for points on the isentrope gh shown in Figure 4.1.

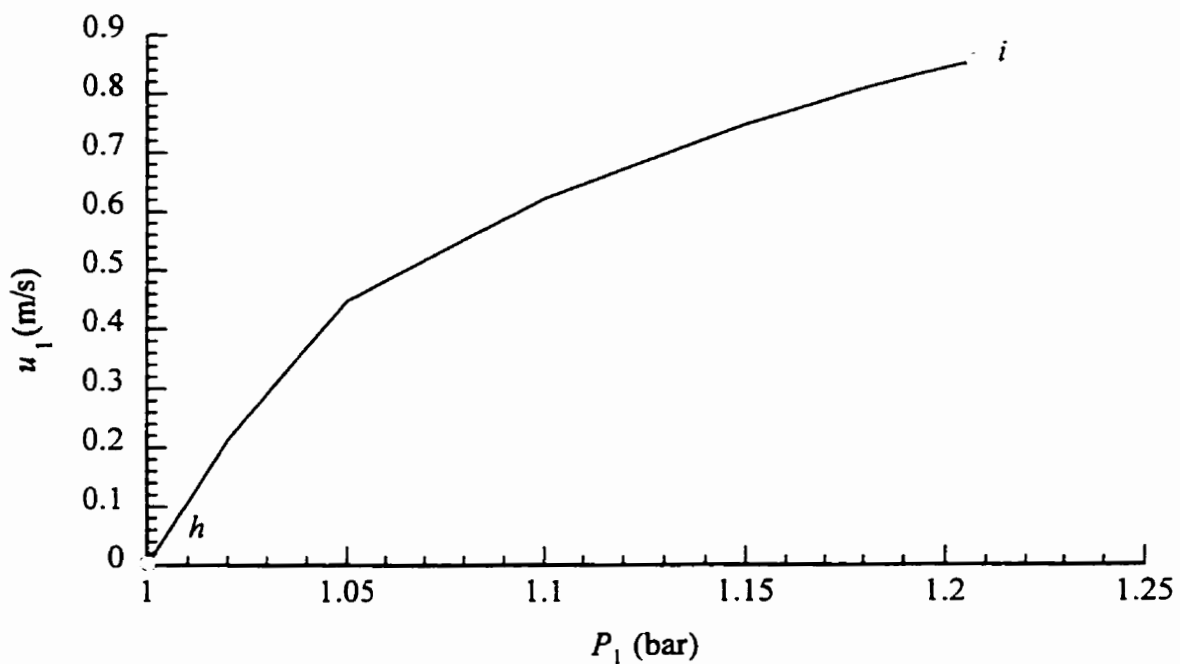


Figure 4.3. Evaporation wave speeds corresponding to the subsonic solutions plotted in Figure 4.2.

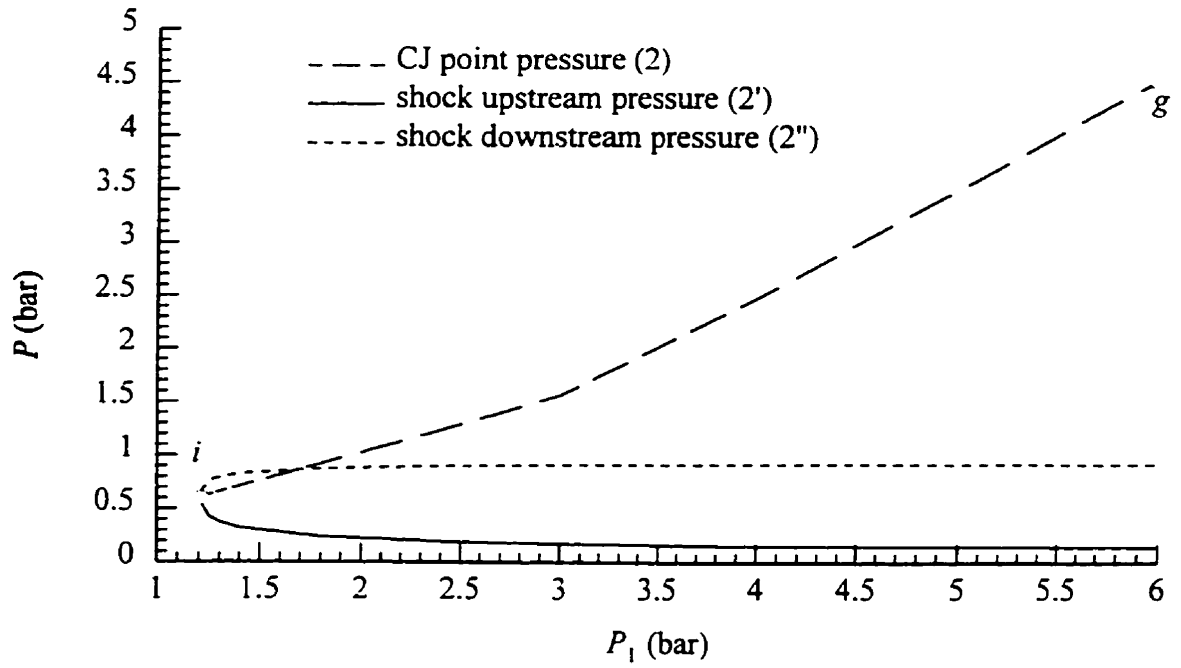


Figure 4.4. CJ solutions for points on the isentrope gh shown in Figure 4.1.

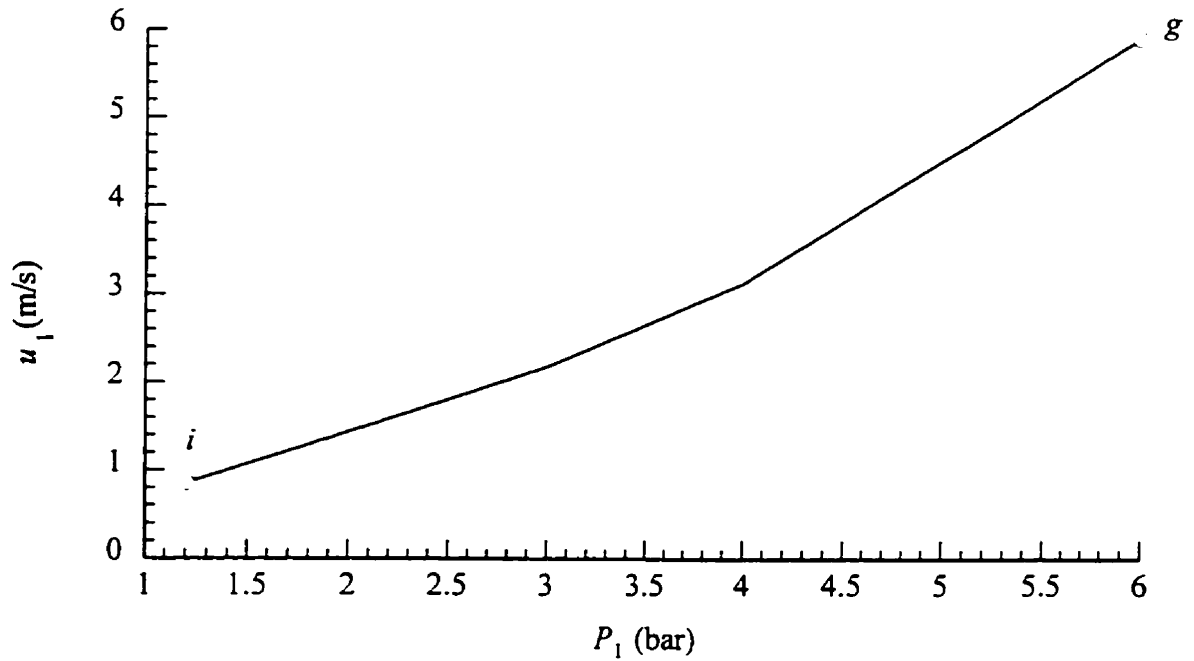


Figure 4.5. Evaporation wave speeds corresponding to the CJ solutions plotted in Figure 4.4.

In order to complete the description of the CJ solutions, a calculation of the predicted radial shock locations is necessary. This can be done simply by considering the conservation of mass between the two discontinuity locations, i.e.

$$\rho_1 u_1 A_1 = \rho_2 u_2 A_2 \quad (4.1)$$

The surface area A in a one-dimensional cylindrical geometry at any radial location is of course equal to $2\pi r l$, where r is the variable radius and l is a constant length equal to that of the cylindrical evaporation discontinuity. Then equation (4.1) can be solved for the shock radius r_2 :

$$r_2 = \frac{\rho_1 u_1}{\rho_2 u_2} r_1 \quad (4.2)$$

The shock locations for the CJ solutions of Figure 4.4 are plotted in Figure 4.6, non-dimensionalized by the nozzle exit radius r_1 .

The question of which state (1) locations lead to a prediction of complete adiabatic evaporation of the liquid can be answered in part by calculating their Jakob numbers. A Jakob number of one indicates that the constant pressure deflagration solution lies on the vapour saturation boundary. In general, the saturation boundary has a slope which is greater than that of the deflagration Hugoniot. Therefore, if the Jakob number at a given state (1) is greater than one, it can be said that all possible (2) states on the Hugoniot will lie in the superheated vapour region of P - v - T space. Since all of the subsonic Hugoniot solutions originate from initial (1) states below 1.21 bar, calculating the Jakob numbers along this cutoff pressure provides an indication of whether or not the evaporation discontinuity model

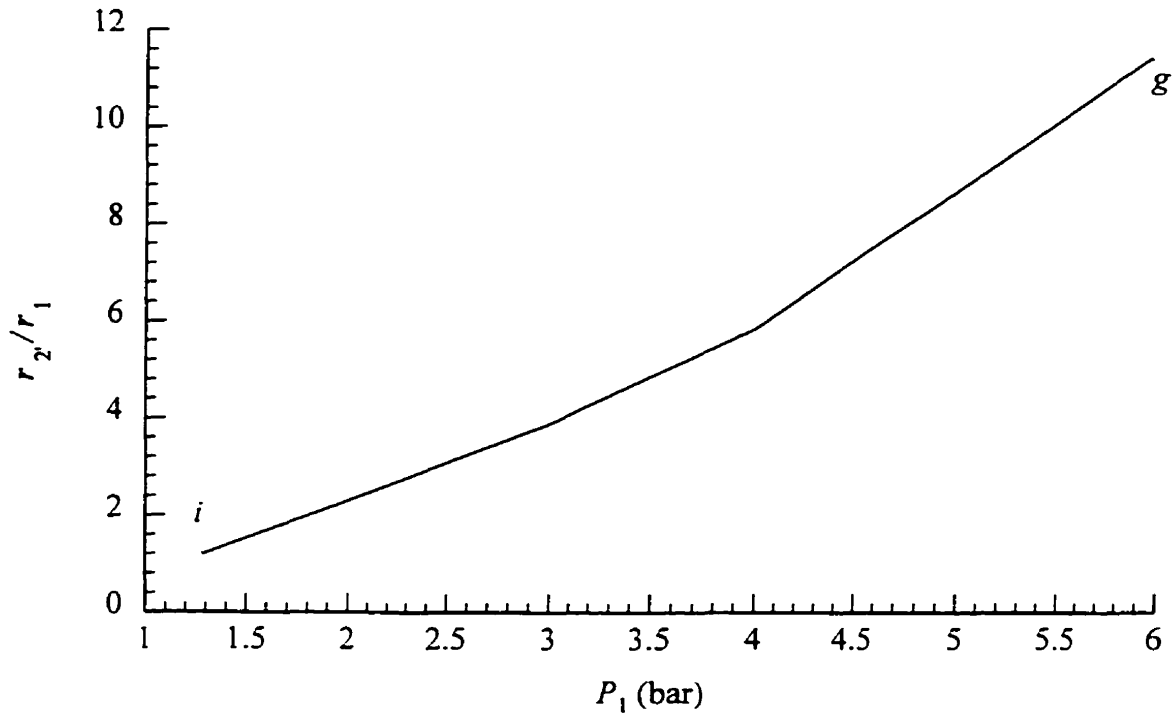


Figure 4.6. Non-dimensionalized shock radius as a function of state (1) pressure for the CJ solutions of Figure 4.4.

predicts complete evaporation in the subsonic case. Furthermore, if $Ja > 1$, the expansion end state (3) will also lie in the single phase region because isentropes have greater negative slope in the P - v plane than the deflagration Hugoniot (see Figure 3.8). The results of the Jakob number calculation are shown in Figure 4.7, plotted against the injection temperature. Virtually all of the subsonic solutions predict a complete evaporation, with the possible exception of some (2) states which are just at the saturation boundary for the lowest injection temperature at which evaporation discontinuities were experimentally observed (303°C).

Above the cutoff pressure, all (2) states are CJ states. A general calculation which divides the CJ solution domain of Figure 4.1 into (1) states that lead to single phase or two phase CJ points has not been attempted. A specific example has already been given for the

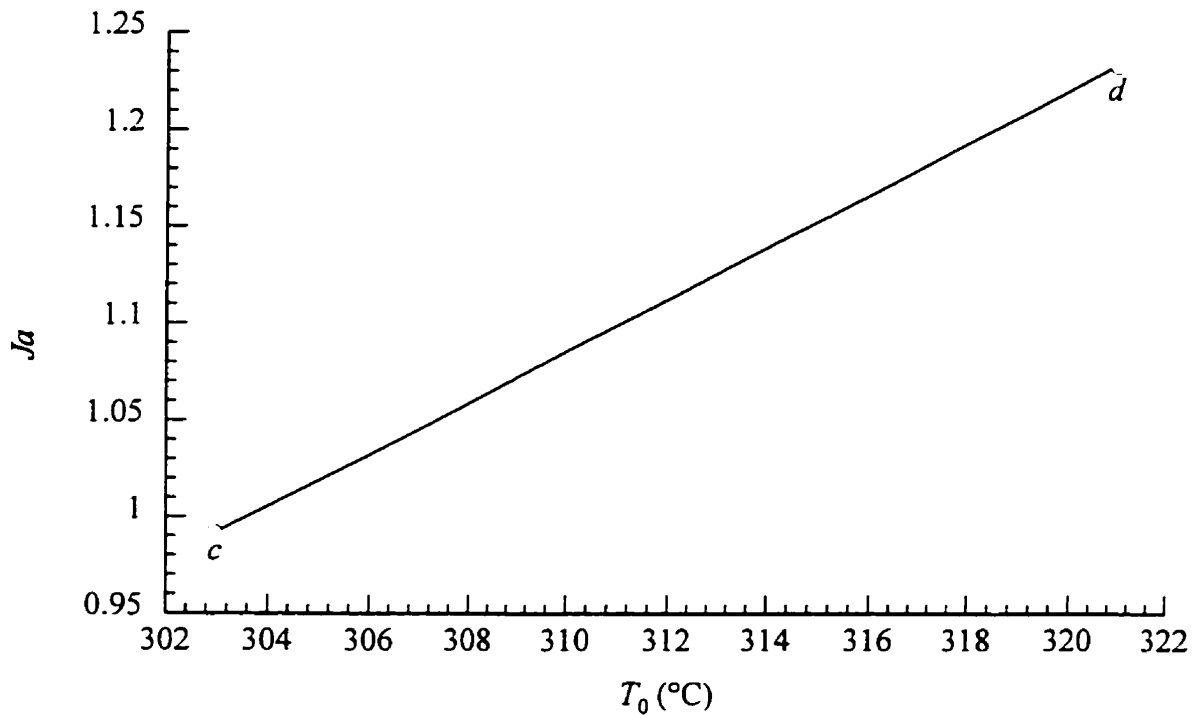


Figure 4.7. Dependence of Jakob number on injection temperature along the cutoff isobar cd of Figure 4.1.

isentrope gh , where the change in slope of the CJ pressure curve indicated a transition to a two-phase CJ point. However, in these cases it was found that the fluid eventually reaches a single phase state during the isentropic expansion from (2) to (2'). Therefore a complete evaporation is predicted in all cases, although not necessarily across the evaporation discontinuity.

4.2. Model of Experimental Injections

As was mentioned previously, closing the model for the experimental results requires a unique determination of the properties of state (1) for each injection temperature. Ideally this would be accomplished without any direct or indirect use of experimental data; instead,

predictions would be made a priori on the basis of an additional boundary condition founded upon thermodynamic considerations. This boundary condition would necessarily involve a description of the fundamental structure of the evaporation discontinuity. Such an approach was taken by Athans [1995], who proposed that the kinetic limit of superheat be used to establish state (1). It is then implicitly assumed that the evaporation discontinuity represents an abrupt surface of coalescing homogeneous nuclei. Athans' results and the experimental diaphragm burst data discussed by Thompson et al. [1987] suggest that specifying a limiting nucleation rate to obtain state (1) is approximately valid very near the critical temperature, but becomes less satisfactory as the temperature decreases. In relation to the present study, a calculation of the homogeneous nucleation rate J at the most highly superheated state likely to be attained (i.e. case f of Figure 4.1, $T \approx 0.9T_c$) results in a value on the order of 10^{-8} nuclei/m³·s. Therefore it seems unlikely that homogeneous nucleation plays a substantial role in the evaporation process and specifying a nucleation rate to estimate state (1) is not appropriate.

The alternative, then, is to use some piece of experimental data to determine state (1). In the fluorocarbon injection experiments of Kurschat et al. [1992] a shock structure incorporating a cylindrical, normal shock wave was seen using interferometry. This observation, along with mass flow measurements which indicated that the flow was not gas dynamically choked (i.e. at the nozzle exit) led them to conclude that a sonic state was being reached in the observed evaporation discontinuity. Accordingly, they considered only CJ solutions in modeling the flow. The measured location of the normal shock wave was used in their computations to "work backwards" to a solution for state (1). By comparison, the

photographic techniques employed by Sloss [1996] did not permit visualization of the density fields in the flow. Therefore, this means of establishing state (1) was not a possibility for the situation under consideration here, and it cannot be definitively stated that CJ solutions are appropriate.

As neither of the two approaches used by other researchers seems applicable, the chosen method of defining state (1) makes use of the experimental data for the mass flow rate at each injection temperature. Assuming that the flow through the nozzle is isentropic, and that accurate thermodynamic property data are available, the experimental mass flow rate is predicted by

$$\dot{m}_{\text{exp}} = \frac{\pi}{4} d^2 \rho_1 \sqrt{-2 \int_0^1 \frac{dP}{\rho}} \quad (4.3)$$

This relation is derived from the Bernoulli equation for steady compressible flow. Equation (4.3) was solved numerically to obtain P_1 , using the experimental mass flow rate \dot{m}_{exp} and the nozzle exit diameter d . It was assumed that nucleation within the nozzle was not occurring and that state (1) was a purely metastable liquid state.

The mass flow rates obtained by Sloss at various injection temperatures are plotted in Figure 4.8. Also plotted for comparison is the discharge predicted by the incompressible version of equation (4.3)

$$\dot{m} = \frac{\pi}{4} d^2 \sqrt{2\rho(P_0 - P_1)} \quad (4.4)$$

The curve corresponding to equation (4.4) is plotted over the “cold” flow region, where the compressibility of liquid dodecane is minimal and the temperature is always less than its

saturation value during the depressurization. P_1 has been taken to be the injection chamber pressure, since the discharge is a purely axial liquid jet in these cases. As can be seen from the figure, there is a large discrepancy between the measured and calculated values, with the measured values being about 35% larger.

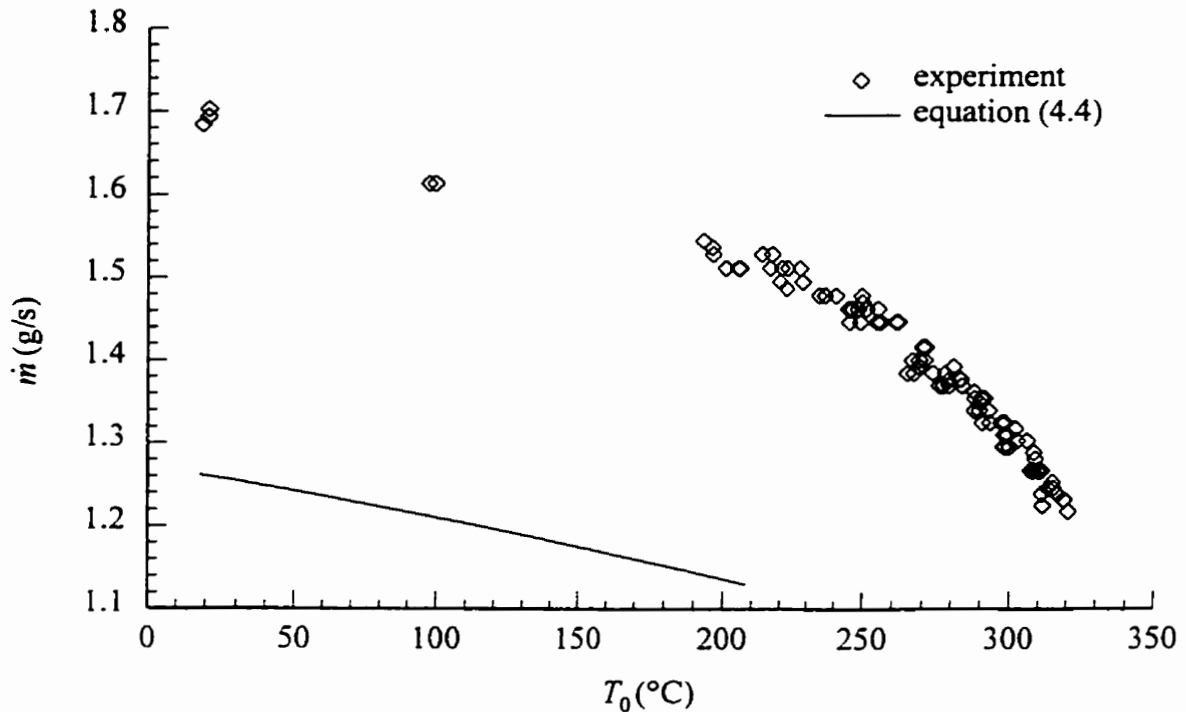


Figure 4.8. Experimental mass flow rates at various injection temperatures compared with those calculated by equation (4.4).

The source of this discrepancy is unclear because it is contrary to what one might expect. Frictional flow losses in the piping or losses associated with viscous effects in the nozzle are not accounted for in equation (4.4), and, therefore, the calculation should overestimate the mass flow rates. Thus it is likely that the error lies in either the experimental readings or in one of the parameters in equation (4.4). Considering the latter possibility, Sloss [1996] suggested that the nozzle diameter d be increased in equation (4.4)

to compensate for the discrepancy. The necessary increase of roughly 16% from 0.21 mm to 0.244 mm is well beyond the estimated error of 0.01 mm of the optical comparator employed in making the diameter measurements. However, a somewhat crude measurement of d in the enlarged photographs of the flow tends to support the hypothesis that the diameter has been underestimated. Based upon calculations with the MSBR equation of state presented earlier in this work, the estimated liquid density error is approximately 2% and as a result is not nearly large enough to account for the mass flow rate error. Therefore it is conceivable that experimental measurement errors have also contributed to the disagreement between experimental and calculated values. It is possible that the rotameter readings were taken before the substantial overshoot of the instrument had been completely damped out. It is also possible that the spray removal system effectively reduced the ambient pressure P_3 somewhat from its nominal value of 1 bar, causing an increase in the mass flow rate.

Regardless of whether the experimental mass flow rates are adjusted downwards to match equation (4.4) or d is increased to match the mass flow rates, the calculation of state (1) in equation (4.3) is not affected because the ratio $\dot{m}_{\text{exp}} / d^2$ remains unchanged. However, determination of the correct mass flow rate is important for assessing the accuracy of the evaporation discontinuity model, as will be shown subsequently. The results of the calculations for state (1) are shown in Figure 4.9, plotted against the injection temperature.

Clearly, all of the (1) states lie in the CJ solution domain (see Figure 4.1). The CJ and shock pressures have been calculated and the results are shown in Figure 4.10. In this case, the plot is made versus the injection temperature because the state (1) points do not lie on a

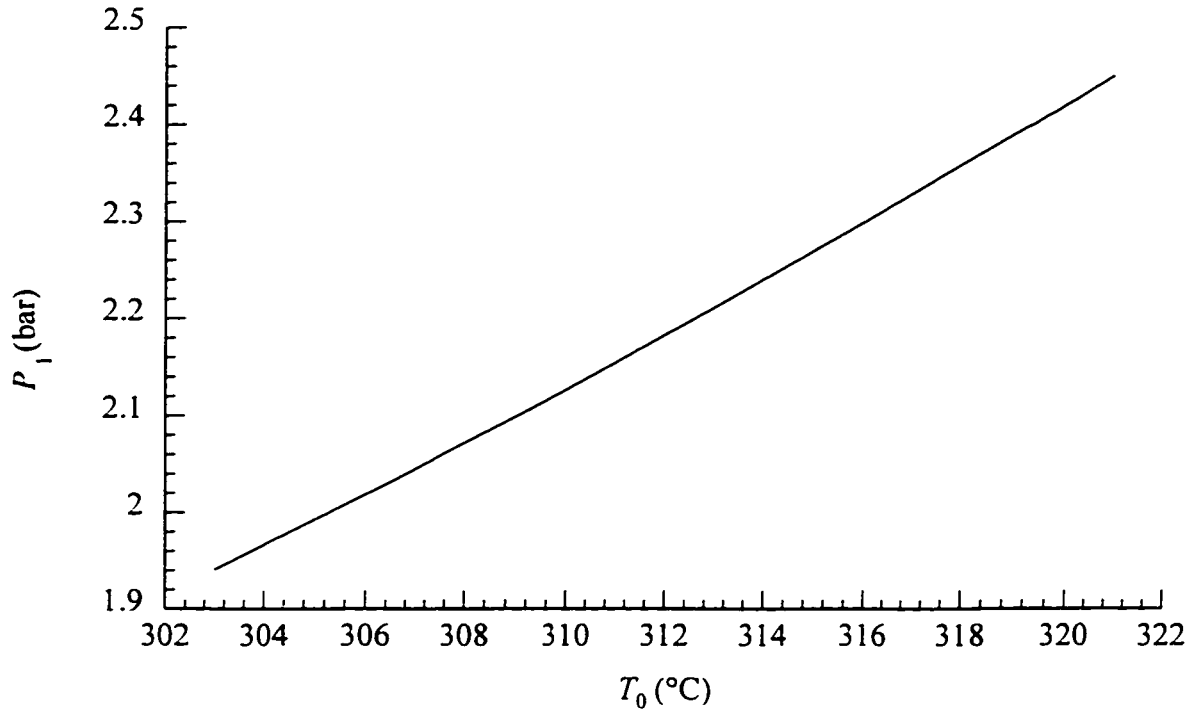


Figure 4.9. Calculation of state (1) as a function of injection temperature, using equation (4.3).

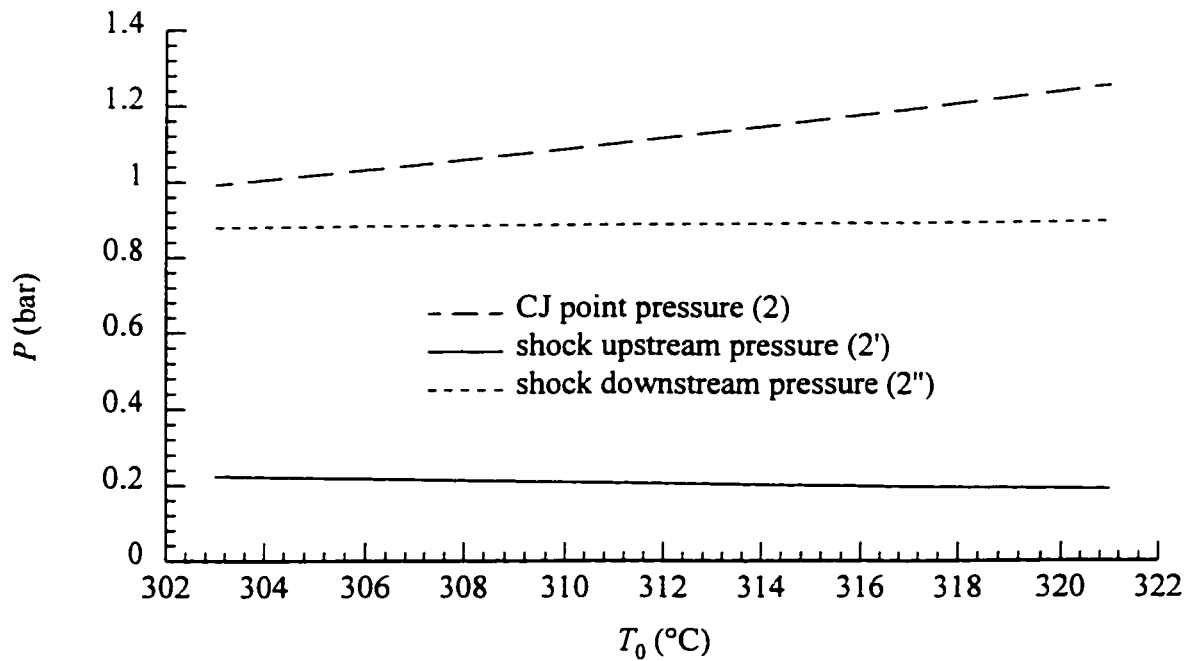


Figure 4.10. CJ solutions corresponding to the experimental injections.

common isentrope. The pressures at the states of interest are very weakly dependent on the injection temperature. The CJ states (2) were found in all cases to lie in the superheated vapour region. Non-dimensionalized radial shock locations are displayed in Figure 4.11. A shock is predicted to lie at a radial distance of roughly 2 to 3 times the nozzle exit radius, depending on the injection temperature. The focus of the next section is a discussion of these results in the context of the experimental observations.

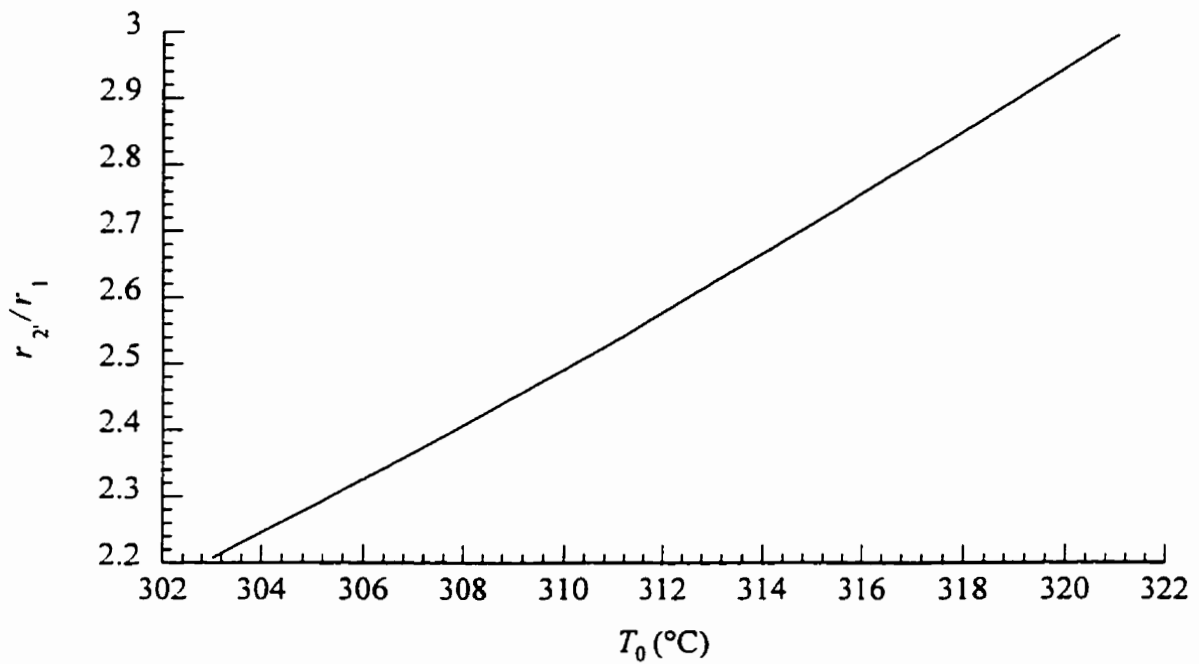


Figure 4.11. Non-dimensionalized shock locations for the CJ solutions plotted in Figure 4.10.

5. DISCUSSION

5.1. Model Comparison with Experiment

In order to validate the proposed model, it is of course necessary to make comparisons between the calculated results and the experimental observations. A quantitative analysis may be made which compares the experimental mass flow rates with those predicted by the deflagration wave theory applied in modeling the evaporation discontinuity. Also, a qualitative comparison can be made by examining the photographic records of the injections, which provide some clues as to the nature of the evaporation process.

5.1.1. Mass Flow Rate Comparison

Although state (1) was selected to match the experimental mass flow rate *through* the nozzle at each injection temperature, nothing has been said to this point concerning the mass flow rate predicted by the balance of the model for the expansion *beyond* the nozzle exit. This is determined from the CJ Rayleigh lines, which indicate the mass flux across the surface of discontinuity. By multiplying the CJ mass flux by an estimate of the discontinuity surface area in each case, a mass flow rate can be obtained and compared with the experimental values. Accurately measuring the surface areas is somewhat difficult due to the graininess of the photographic enlargements, and uncertainties concerning the scale and symmetry of the images. Referring back to Figure 3.3, it can be seen that the discontinuities can be characterized as having an essentially parabolic cross-section, with metastable core lengths, l , at each injection temperature as shown in Figure 3.4. The maximum width, w , of the cross-

section was found to be constant at approximately 0.35 mm, independent of the temperature. This is significantly larger than even the adjusted nozzle diameter of 0.244 mm because there is some radial divergence of the liquid core flow very close to the exit. Surface areas were calculated for each injection in the temperature range 303-321°C according to the formula

$$A = \frac{\pi w^4}{96l^2} \left[\left(1 + 16 \frac{l^2}{w^2} \right)^{\frac{3}{2}} - 1 \right] \quad (5.1)$$

These areas were then multiplied by the corresponding mass fluxes for the CJ solutions described in section 4.2 to obtain the model mass flow rate data points in Figure 5.1. For comparison purposes, the unadjusted experimental mass flow rates for these injections are plotted, as well as the incompressible flow calculation using equation (4.4) with $d=0.244$ mm.

Due to the uncertainty of the surface area measurements, the model predictions of mass flow rate are also essentially uncertain, but are expected to be “accurate” to within $\pm 15\%$. Even if the experimental values of the mass flow rate plotted in Figure 5.1 are assumed to be some 35% larger than the actual values (as was discussed previously in section 4.2), it is clear that the model underestimates the discontinuity mass flux. Several reasons for this can be inferred from the photographs taken of the flow and the assumptions made in formulating various aspects of the flow model.

5.1.2. Qualitative Comparison

A photograph representative of the injections under consideration was shown in

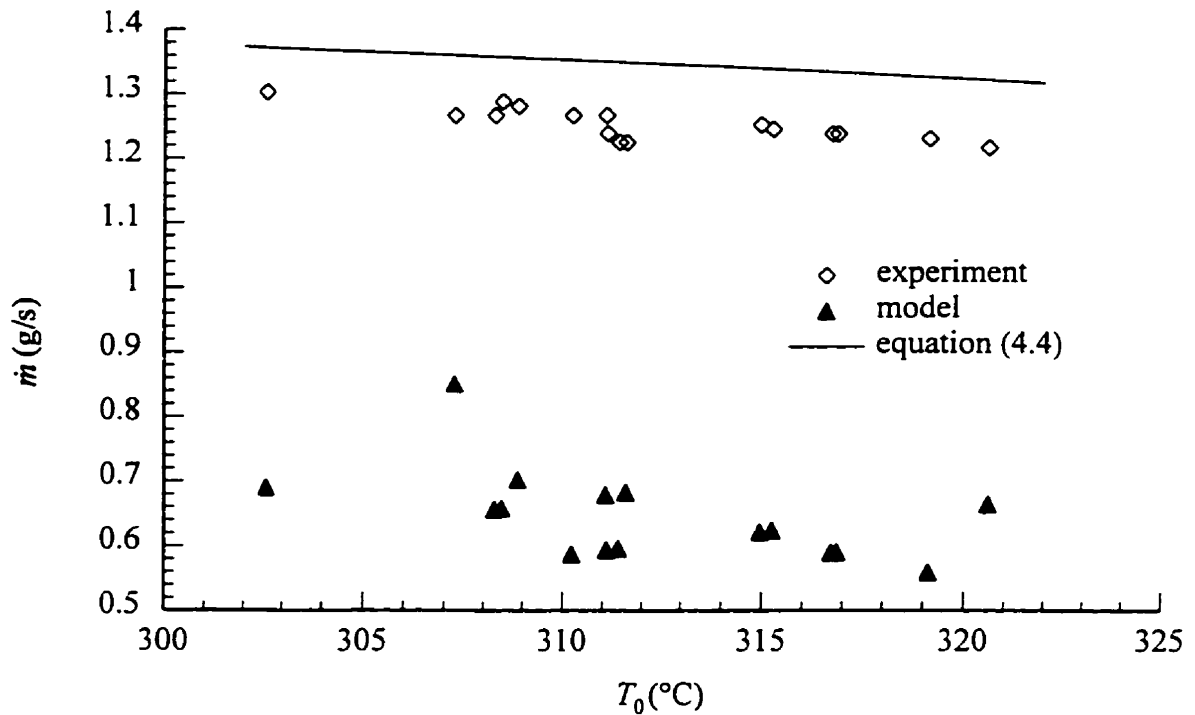


Figure 5.1. Comparison of mass flow rates predicted by the discontinuity model with experimental values at each injection temperature.

Figure 3.3. In this picture, it can be seen that the dense core region below the nozzle is surrounded by an evaporating cloud of droplets. In contrast to this, the CJ states (2) immediately downstream of the evaporation discontinuity obtained in the calculations of section 4.2 were found to lie in the superheated vapour region. CJ solutions which qualitatively match the actual behaviour exist and have been presented in section 4.1. For example, the solution originating from a state (1) with a pressure of 4 bar on the isentrope gh of Figure 4.1 has a two-phase CJ point. The subsequent isentropic expansion from the CJ state (2) to the proposed normal shock wave at state (2') crosses the saturation boundary into the single phase vapour region, in agreement with the gradual disappearance of the spray in

the photographs. The mass flow rate across the evaporation discontinuity is predicted to be 1.2 g/s in this case, similar to the experimental values shown in Figure 5.1. However, a substitution of $P_1=4$ bar into equation (4.3) results in a significant underprediction of the experimental mass flow rate for the flow *through* the nozzle.

These observations suggest that the equilibrium model proposed for the downstream state (2) of the evaporation discontinuity inadequately describes the features of the flow, although it does provide estimates for the mass flow rate which have the correct order of magnitude. On the basis of the example discussed above, it is also evident that if the downstream state (2) of the evaporation discontinuity is partially liquid, then higher mass flow rates will be predicted. This can be seen clearly from equation (3.5) for the mass flux i across a discontinuity, repeated below as equation (5.2)

$$\frac{P_2 - P_1}{v_2 - v_1} = -i^2 \quad (5.2)$$

For a given pressure drop, P_1-P_2 , the mass flux will be considerably larger when the specific volumes of the two states are closer together. Therefore it is reasonable to expect that state (2) is a non-equilibrium mixture of liquid and vapour, with a smaller value of v_2 than that obtained from the equilibrium model. For the purposes of this discussion it may be assumed that mechanical equilibrium is maintained between the liquid and vapour phases; therefore the non-equilibrium is expressed as a temperature difference between the phases. In this scenario, the liquid phase would be further superheated due to the pressure drop across the discontinuity, so it is conceivable that the droplets could eventually evaporate completely.

The droplets would form a fine mist that gradually disappears at a location downstream of the discontinuity.

There is also some cause to doubt the validity of the chosen states (1). The difference between the incompressible flow calculation for the mass flow rate and the experimental data points in Figure 5.1 was assumed to be a result of the presence of the evaporation discontinuity. The large change in fluid momentum caused by the evaporation was hypothesized to support a sizable pressure drop across the discontinuity, with the sonic flow condition allowing the pressure at the nozzle exit to be significantly above the ambient pressure of 1 bar (Figure 4.9). Carrying this interpretation further, there would have to be a discontinuous decrease in the experimental mass flow rates at the lowest injection temperature at which evaporation discontinuities were first observed. Instead, the complete set of data shown previously in Figure 4.6 indicates that no such transition occurs. The experimental data points diverge smoothly from the mass flow rate calculated using equation (4.4) for injection temperatures above the normal boiling temperature of dodecane (216°C). Taking into account liquid compressibility by using equation (4.3) to obtain the mass flow rates does not alter this result. Therefore, it is possible that the rapidly decreasing mass flow rate at the highest injection temperatures is a result of vapour production within the nozzle at heterogeneous nucleation sites on the nozzle walls.

The presence of small bubbles in the metastable liquid flow through the nozzle would have the effect of increasing the compressibility and decreasing the average density of the fluid, resulting in lower mass flow rates. Also, v_l in equation (5.2) would be significantly larger even for small vapour fractions, allowing the model to predict an even larger

discontinuity mass flux for a given pressure drop. If the flow upstream of the discontinuity is a bubbly liquid, however, it is unclear whether a homogeneous model is still applicable for state (1). It is also doubtful that the properties of state (1) would be uniform along the discontinuity, meaning that the local jump conditions at each point of its surface could be different. The supposition of a non-uniform state (1) is supported by the photographs of the flow. Near the base of the dense core, the flow downstream of the discontinuity is clearly a two-phase mixture. The normal and tangential components of the flow velocity are roughly equal, based upon the outer angle of the spray. On the other hand, the visible spray does not extend much beyond the tip of the discontinuity. This suggests that the flow at the end of the core is either bent through a larger angle as it crosses the discontinuity or has evaporated more fully across the discontinuity.

The normal shock location results shown in Figure 4.11 indicate that a shock wave, if present, would be found at a distance of 2.2 to 3 times the discontinuity radius. This corresponds to anywhere from 0.385 to 0.525 mm from the jet axis, depending on the injection temperature. In contrast to this, the shock waves observed by Kurschat et al. [1992] were found to lie at radial distances of roughly 10 to 100 times the nozzle radius. The explanation for this can be found in the fact that much higher injection pressure ratios (P_0/P_3) were utilized in their experiments. Upon injection into a near-vacuum environment, the CJ pressure (2) falls significantly above the ambient pressure (3) and the subsequent isentropic expansion from (2) to (2') occurs over a much larger radial distance. Figure 4.8 showed that the CJ and ambient pressures were very close together for the model presented here, leading to a relatively short isentropic expansion to the proposed shock wave. In the case of the near-

critical expansions studied by Athans [1995], shocks were also seen at distances on the order of 10 times the nozzle radius despite the fact that the injection chamber pressure was 1 bar. These results may be interpreted as qualitatively similar to those presented for the expansion from point *g* in Figure 4.1. For the rightmost data points of Figure 4.4, state (1) lies at a high pressure relative to the ambient condition, as does the CJ pressure (2). Again, the expansion from (2) to (2') occurs over a large radial distance and the non-dimensionalized shock location r_2/r_1 is roughly 12 (see Figure 4.6). Athans chose the superheat limit to represent state (1). Since this corresponds to very high pressures at near-critical temperatures, the equilibrium model can be expected to predict a shock wave at a location comparable to what was observed experimentally.

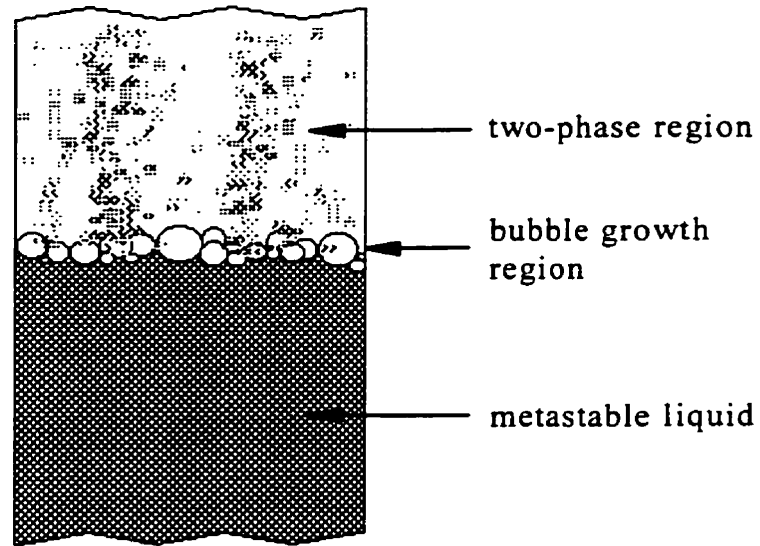
Returning to the shock location data of Figure 4.11, it can be said that these results are quantitatively different from those obtained experimentally by other researchers, primarily due to differences in experimental conditions. They are also not sustained by the photographic evidence of Sloss [1996]. If a shock wave was located very close to the evaporation discontinuity, it would lie in the region where a two phase flow is visible. Since a retrograde fluid will condense on adiabatic compression, a brightening of the droplet cloud would be expected at the predicted shock location. Nonetheless, it is possible that the shock location is underestimated due to the equilibrium and geometric assumptions of the complete flow model. The presence or absence of a shock wave in the single phase region further downstream could only be confirmed by interferometry or other techniques which allow visualization of the density fields in the flow. Therefore, it cannot be stated for certain whether or not a sonic condition is achieved on the downstream side of the discontinuity.

However, given that it would appear that the pressures used for state (1) in the model calculations of section 4.2 were too high, there is reason to suspect that a subsonic, non-equilibrium evaporating flow exists downstream of the discontinuity.

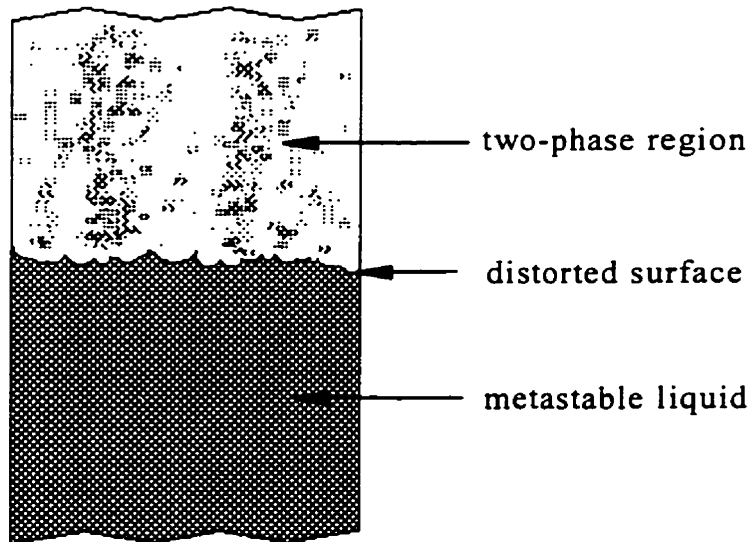
If state (2) is indeed a non-equilibrium mixture of superheated liquid and vapour, a question arises. How does one account for the presence of this liquid, considering that the liquid dodecane upstream of the discontinuity may have enough stored energy to undergo a complete adiabatic evaporation? The answer must lie in the mechanisms and structure of the evaporation discontinuity, which evidently is not a smooth liquid-vapour interface. Little can be said about the discontinuity structure from the images obtained by Sloss. However, the work of other researchers suggests some possible explanations for the observed behaviour. These will be considered briefly in the following section.

5.2. Evaporation Discontinuity Structure

In the context of describing the structure of the discontinuity, it is perhaps more appropriate to use the terminology “evaporation wave” in the sense that the evaporating region has finite thickness. Two studies which provide clear images of the wavefront region are the diaphragm burst experiments of Hill [1991], who used R12 and R114 as the test fluid, and Simões Moreira [1994], who used dodecane. The evaporation waves observed by these researchers were roughly planar in nature which allowed them to obtain pictures of the surface from a variety of angles. Figure 5.2 illustrates two possible interpretations of the structure of the evaporation waves seen in the pictures of Simões Moreira. The leading edge



(a)



(b)

Figure 5.2. Possible interpretations of the evaporation wave structure observed in diaphragm burst experiments.

of the wave was found to consist mostly of smooth, hemispherical bubble-like structures. The different interpretations arise because it is unclear whether these structures are complete, individual bubbles with liquid film caps or are in fact part of a single, distorted surface. Each possibility will be examined with reference to the present work.

5.2.1. Growing Bubble Layer

If the surface is composed of individual bubbles, then the propagation mechanism of the evaporation wave is the nucleation, growth and subsequent bursting of these bubbles, as shown in Figure 5.2 (a). Hill considered the question of how much of an evaporating bubble would be submerged in the surrounding liquid by examining the balance of static forces on an isolated bubble. The dimensionless Bond number is the appropriate parameter which characterizes the ratio of gravitational to surface tension forces. Based on a Bond number calculation, Hill estimated that the bubble film cap would be 10% of the total bubble surface area. However, the validity of this result is somewhat questionable considering that the analysis neglects the dynamic effects of evaporation. It is even more doubtful that this is applicable to vertical injection experiments, in which the liquid is not quiescent and the relative positions of the liquid and vapour phases are reversed.

The presence of individual bubbles requires that there be a source of nuclei. Homogeneous nucleation is ruled out because insufficient superheating was attained in any of the experiments, and in any case, this sort of nucleation would occur everywhere in the metastable liquid rather than in the vicinity of the wavefront. Consequently, a secondary nucleation hypothesis put forward by Mesler and Bellows [1988] was considered by both Hill

and Simões Moreira in the context of their experiments. According to this theory, the receding liquid film from a rupturing bubble forms beads which impact on the liquid surface. These beads or droplets entrain microscopic vapour nuclei which are carried below the surface. New bubbles then grow from these nuclei and rupture, producing a continuous cycle. Variations on the secondary nucleation theory have been proposed by other researchers, but all are essentially based upon the notion of droplets impacting on a liquid-vapour interface and entraining vapour nuclei.

There appears to be an ample supply of droplets which may cause secondary nucleation events in the photographs and videos taken by both Hill and Simões Moreira. When a bubble-like structure was seen to burst, adjacent bubbles structures were often observed to do so as well. The fragmentation of the interstitial liquid between the bubbles structures and the bubbles' (hypothetical) film caps produced an aerosol-like spray. Most of this was carried downstream, entrained by the outflowing vapour from the interface. However, instances in which some of this spray hit the liquid surface did occur.

This interpretation of the wave structure does provide a possible explanation for the presence of liquid downstream of the evaporation waves observed in the photographs taken by Sloss [1996]. Regardless of the fact that the liquid dodecane may be superheated to a state that has the potential for a complete, discontinuous evaporation, the dynamic effects of rupturing bubbles could certainly allow superheated liquid to cross the wavefront and subsequently evaporate. The Jakob number was consistently less than one in the experiments of Hill and Simões Moreira, so the liquid could not have evaporated completely and a two-phase equilibrium state was assumed to be achieved some distance behind the leading edge of

the wavefront. For injection-type experiments, however, there are other important qualitative differences which have implications for the proposed wave structure. Both Hill and Simões Moreira found that the scale of individual bubble-like structures decreased with increasing superheat. This is likely attributable to the decrease in surface tension with increasing temperature. Presumably, bubbles with a higher temperature at their interface would become unstable and burst at smaller radii. At the relatively low superheats of Hill's experiments, leading edge bubble structures were observed to grow to sizes in excess of 1 mm radius. Even at the highest initial temperatures achieved by Simões Moreira ($\approx 300^\circ\text{C}$), individual structures with radii as large as 0.15 mm can be discerned in the still photographs. Considering that the *maximum* discontinuity width seen in Sloss's injections was measured to be roughly 0.35 mm, individual bubble structures of this size are not plausible. Realistically, individual bubbles would have to be at least an order of magnitude smaller to produce the regular discontinuity shape observed.

A possible explanation for the ostensibly smaller bubble sizes is that the metastable liquid is moving. The estimated Reynolds number based on the nozzle exit diameter is on the order of 10^4 , indicating that the flow is turbulent. Combined with the fact that there must be considerable shearing at the interface due to tangential liquid motion, it is reasonable to expect that individual bubbles would burst at relatively small sizes. Additional sources of instability have been postulated for rapidly evaporating systems. These may effect the growth rates and form of individual bubbles, and also have been considered as a potential mechanism for the wave structure schematic shown in Figure 5.2 (b).

5.2.2. *Single Interface*

Both Hill and Simões Moreira hypothesized that interfacial instabilities may cause the observed wavefront structures. In particular, they considered the role the Landau mechanism of instability plays in destabilizing interfaces across which large density differences exist. First proposed as a destabilizing mechanism for laminar flame fronts, this theory was also applied to a rapidly evaporating surface by the original author (Landau and Lifshitz, [1959]). It also appears implicitly, along with other proposed destabilizing factors, in theoretical work on evaporation by Miller [1973] and Palmer [1976]. The essential quality of the instability hypothesis is that initial perturbations at the liquid-vapour interface become further amplified through their interaction with the evaporative mass flux. In order to produce the two-phase flow downstream of an evaporation wave, the instability must become sufficiently non-linear to distort the interface such that liquid is actually stripped away.

Experiments performed by Shepherd and Sturtevant [1982] and Frost and Sturtevant [1984] provide evidence of Landau instabilities influencing rapid evaporation. A bubble column apparatus was used to heat single, small droplets of isopentane, butane and ether to their respective superheat limit temperatures. In each case, a single bubble was observed to homogeneously nucleate inside the droplet and explosively vapourize the surrounding liquid. During the early stages of this process, small amplitude, short wavelength disturbances were observed on the surface of the growing bubble, giving it an appearance which the authors characterized as resembling “orange peel”. These disturbances subsequently developed into more extreme convolutions. This behaviour is markedly different from the smooth, spherical bubbles which occur in normal boiling. In addition, Shepherd and Sturtevant calculated the

evaporative mass flux implied by their measurements and found it to be two orders of magnitude larger than that predicted by the classical theory of bubble growth derived by Prosperetti and Plesset [1978]. Furthermore, the calculated effective density in the interior of the bubble was consistent with that of a two-phase mixture. Both of these results lend support to the idea that the instability allows some portion of the surrounding liquid to cross the evaporating front.

For the purposes of this discussion, some background on the classical bubble growth theory is necessary. According to classical theory, the growth of a stable vapour bubble can be divided into three regimes. Surface tension controls the rate of growth in the first stage, while the bubble is still on the same scale as a critical nucleation radius. After this, growth is limited by the inertia of the surrounding liquid and the bubble radius grows at a constant rate. The final stage is limited by the rate at which heat is conducted to the interface, and the interface decelerates producing asymptotic growth. In their linear stability analysis, Frost and Sturtevant [1984] found that the evaporating surface was stable during the first and last stages of bubble growth. However, they predicted that for the conditions of their experiment, the bubble would be unstable in the intermediate stage at certain perturbation wave numbers.

During this intermediate, unstable stage, the bubble size was too small for experimental corroboration, so it was proposed that the instability entered a non-linear, "saturated" phase which persisted as the bubbles grew to macroscopic size. Typical disturbances were observed to be from 20 to 40 μm in size. This is 2 to 4 times larger than the largest unstable wavelength predicted. This is also clearly much smaller than the scale of the bubble-like structures seen in the diaphragm burst experiments, an observation that led

Hill [1991] to question whether they are a manifestation of a global evaporative instability. However, he did not rule out the presence of local instabilities, because small scale roughening of a fraction of the smooth structures was occasionally observed. In the injection experiments of Sloss [1996], the size of perturbations on the wavefront is much smaller (see section 5.2.1) and therefore the Landau instability mechanism may provide an explanation for the spray downstream of the liquid core region. As the stability criteria depend on the ambient pressure, wavefront geometry and fluid properties, calculations for the experimental conditions are necessary in order to adequately address the issue. There is also reason to believe that the stability analysis may change for evaporation in a retrograde fluid, since it can occur at a molecular level without heat conduction. In other words, the stabilizing, thermally controlled stage of bubble growth of the classical theory may be absent, depending on the degree of superheating.

In summary, both the secondary nucleation hypothesis and the Landau instability hypothesis could account for the presence of liquid downstream of an evaporation wave, even if the Jakob number of the incoming flow is greater than one. Neither hypothesis can be definitively ruled out as a mechanism for the evaporation discontinuities seen in the injection experiments of Sloss [1996]. The presence of a finite wave structure also highlights some of the deficiencies of the evaporation discontinuity model. Neglecting surface tension effects in the model is a source of error because the local curvature of a distorted interface may be quite high. Furthermore, viscous dissipation within a growing bubble layer or near a distorted interface may be considerable. Therefore, treating the wave as a smooth, non-dissipative discontinuity in the flow represents a significant idealization.

6. CONCLUSIONS

6.1. Summary

A thermodynamic analysis of the injection of preheated dodecane through a converging nozzle was made. Specifically, the analysis was applied to the conditions of the injection experiments conducted by Sloss [1996] in which a standing evaporation wave was observed in the flow near the nozzle exit. This corresponded to experiments in which the fuel was preheated to temperatures between 303°C and 322°C. In each case, the fuel was expanded from an upstream pressure of 10 bar to an injection chamber pressure of 1 bar.

As a prelude to developing a model for the flow system, a study of various hydrocarbon equations of state was undertaken to determine which would most accurately represent the thermodynamic properties of dodecane. The equilibrium saturation properties predicted by each equation of state were tested against appropriate correlations recommended for this substance. In particular, percentage error curves were generated for saturation pressure and saturated liquid volume in order to quantitatively compare the equations of state. In addition, the accuracy of metastable liquid properties was assessed by comparing the liquid spinodal lines calculated by each equation with the kinetic limit of superheat obtained from homogeneous nucleation theory. It was found that many equations of state have been developed to represent saturation properties without considering the overall accuracy and thermodynamic consistency throughout P - v - T space. Although no single equation of state was clearly superior to the others, the modified Simonet-Behar-Rauzy (MSBR) equation (Jullian et al., [1989]) was considered to provide the best overall balance between accurate

metastable and equilibrium properties. The principal flaw of this equation of state is its inability to represent the region around the thermodynamic critical point. Should the need arise in the future for property data in this area, it is recommended that the modified Benedict-Webb-Rubin equation developed by Soave [1995] be used.

Using the MSBR equation of state as a source of thermodynamic property data, an injection flow model was developed and calculations were performed corresponding to the relevant experimental conditions. The injection flow model proposed was comprised of three stages. The first stage consisted of an isentropic expansion through the nozzle from a subcooled liquid state to a superheated liquid state. Subsequent flow beyond the nozzle exit was idealized as being purely radial to simplify the analysis. In accordance with this assumption, the second stage of the model became a transition to an equilibrium state across a cylindrical evaporation discontinuity. The discontinuity was described as a deflagration wave using the Rankine-Hugoniot equations. The sonic, Chapman-Jouguet (CJ) state and subsonic states were considered as possibilities for the flow exiting the downstream side of the discontinuity.

A stagnation boundary condition at an infinite distance from the nozzle axis was applied to the radial, outward flow from the discontinuity. As such, the model for this flow was different depending on whether a subsonic or sonic state was appropriate for the discontinuity downstream state. In the case of subsonic solutions, a straightforward isentropic flow to the stagnation state was proposed. For CJ solutions, the flow was predicted to overexpand with respect to the injection chamber pressure. A normal shock

transition from a supersonic to a subsonic flow followed this expansion. The subsonic flow was then taken to stagnate isentropically to the ambient pressure.

A general calculation was made to determine which of the two types of solution (subsonic or CJ) is valid for various metastable liquid states achievable by isentropic expansion through the nozzle. Subsonic solutions were found for states with pressures lying between 1 and 1.21 bar. The 1 bar solution corresponded to zero mass flux across the discontinuity. The mass flux approached the CJ mass flux for the 1.21 bar subsonic solution. CJ solutions were found for metastable liquid states with pressures below the saturation pressure and above 1.21 bar. According to the model, greater overexpansion resulted for higher pressures in this range. This increased both the calculated jump in pressure across the normal shock wave and the radial location of the shock wave.

Calculations specific to the experimental injections were made by selecting a single metastable liquid state for each injection temperature. This was accomplished by calculating the pressure at which the mass flow rate determined from an isentropic flow relation matched the experimental value. The pressure at each of these states was found to lie in the range for which CJ solutions were indicated. The CJ mass flux was calculated for each injection temperature and multiplied by an estimate of the discontinuity surface area obtained from photographs of the injections. The mass flow rate determined in this manner was on the same order of magnitude as the experimental values. However, it was clear that the model underestimated the true mass flow rates. Also, the model predicted that complete evaporation would be attained across the discontinuity, unlike the seemingly two-phase flow shown by the photographs. A calculation of the radial shock locations indicated that shock

waves should lie at distances between 0.385 and 0.525 mm from the jet axis, depending on the injection temperature. No qualitative evidence for the existence of shock waves this close to the evaporation discontinuity could be found in the photographs. Other researchers have observed shock waves in preheated injection flows at much greater distances from the nozzle exit. However, this is thought to be a result of the much larger injection pressure ratios used in their experiments. Combined with the shortfall in the mass flow rates and qualitative differences with the experimental observations, the shock location results inferred that the equilibrium model was inadequate to describe the flow. It appears that the flow downstream of the discontinuity may in fact be a subsonic, evaporating non-equilibrium flow.

Finally, existing theories of evaporation wave structure were examined in the context of both diaphragm burst and injection experiments. Specifically, the secondary nucleation and interfacial instability hypotheses identified by Hill [1991] were studied as possible explanations for the observed behaviour of the evaporation discontinuity. Neither hypothesis can be definitely disqualified as a mechanism for the evaporation waves photographically observed in injection style experiments. Further experimental and theoretical work is necessary to clarify the nature of the evaporation process.

6.2. Recommendations for Future Work

A number of suggestions for further research can be made. On the experimental side, much could be accomplished by modifications or additions to the existing experimental apparatus. Optics allowing the visualization of shock waves would determine conclusively whether or not sonic conditions are being achieved in the flow. A design providing variable

injection chamber pressures would permit experiments that could be directly compared to those performed by other researchers. If near-vacuum conditions are achieved, flows which more closely follow the radial expansion utilized in the flow model would likely result. It would also be interesting to examine the start-up behaviour which leads to the establishment of evaporation waves. This could be accomplished by transient measurement of flow properties and multiple photographs of a single injection. Experiments with different nozzle diameters would determine the effects of liquid flow velocity and nozzle surface area on the superheat required to initiate an evaporation discontinuity.

On the computational side, work could be done to extend the present flow model to incorporate non-equilibrium effects. A variety of two-fluid and single fluid models are available to describe non-equilibrium flows. These could be applied to the postulated evaporating, subsonic flow downstream of the discontinuity. To this end, some estimate of the distribution of droplet sizes and over all liquid mass fraction produced at the discontinuity is necessary. Experimental techniques allowing these items to be measured would be of great benefit. Further study into the mechanisms of the evaporation wave might also provide estimates of these quantities. As previously mentioned, it would be useful to calculate the range of wavelengths, if any, for which a surface in the form of the evaporation discontinuity is subject to Landau instability. A correlation might be proposed relating these wavelengths to droplet sizes downstream of the interface. Regardless of the model chosen for the evaporation wave structure, it must ultimately be coupled to the conservation equations for mass, momentum and energy transfer across the interfacial region.

References

- Alamgir, Md. and Lienhard, J.H. "Correlation of pressure undershoot during hot water depressurization." *Journal of Heat Transfer*, vol. 103, pp. 52-55, 1981.
- Athans, R.E. "The rapid expansion of a near-critical retrograde fluid." PhD Thesis, Rensselaer Polytechnic Institute, Troy, NY, 1995.
- Behar, E., Simonet, R. and Rauzy, E. "A new non-cubic equation of state." *Fluid Phase Equilibria*, vol. 21, pp. 237-255, 1985.
- Carey, V.P. Liquid-Vapour Phase Change Phenomena. Hemisphere Publishing Corporation, U.S.A., 1992.
- Chaves, H., Lang, H., Meier, G.E.A, and Speckmann, H.D. "Adiabatic phase transitions and wavesplitting in fluids of high specific heat." Flow of Real Fluids. Meier, G.E.A. and Obermeier, F. (eds.), Springer-Verlag, pp. 115-124, 1985.
- Chu, J.Z., Zuo, Y.X., and Guo, T.M. "Modification of the Kumar-Starling five-parameter cubic equation of state and extension to mixtures." *Fluid Phase Equilibria*, vol. 77, pp. 181-216, 1992.
- Cole, R. "Boiling nucleation." *Advances in Heat Transfer*, vol. 10, pp. 85-167, 1974.
- Das, P.K., Bhat, G.S. and Arakeri, V.H. "Investigations on the propagation of free surface boiling in a vertical superheated liquid column." *International Journal of Heat and Mass Transfer*, vol. 30, no. 4, pp. 631-638, 1987.
- Daubert, T.E. and Danner, R.P. Data Compilation Tables of Properties of Pure Compounds. New York, Design Institute of Physical Property Data, AIChE, 1985.
- Deligiannis, P. and Cleaver, J.W. "Determination of the heterogeneous nucleation factor during a transient liquid expansion." *International Journal of Multiphase Flow*, vol. 18, pp. 273-278, 1992.
- Detleff, G., Thompson, P.A., Meier, G.E.A. and Speckmann, H.D. "An experimental study of liquefaction shock waves." *Journal of Fluid Mechanics*, vol. 95, pp. 279-304, 1979.
- Fowles, G.R. "Vapor detonations in superheated fluids." Adiabatic Waves in Liquid-Vapor Systems. Meier, G.E.A. and Thompson, P.A. (eds.), Springer-Verlag, pp. 407-416, 1990.
- Friz, G. "Coolant ejection studies with analogy experiments." *Proc. Conf. on Safety Fuels and Core Design in Large Fast Power Reactors*, ANL-7120, pp.890-894, 1965.

Frost, D. and Sturtevant, B. "Effects of ambient pressure on the instability of a liquid boiling explosively at the superheat limit." *Journal of Heat Transfer*, vol. 108, pp. 418-424, 1986.

Grolmes, M.A. and Fauske, H.K. "Axial propagation of free surface boiling into superheated liquids in vertical tubes." *Proc. 5th Int. Heat Transfer Conf.*, Paper B1.7, vol. 4, pp. 30-34, 1974.

Hill L.G. and Sturtevant B. "An experimental study of evaporation waves in a superheated liquid." *Adiabatic Waves in Liquid-Vapor Systems*. Meier, G.E.A. and Thompson, P.A. (eds.), Springer-Verlag, pp. 25-37, 1990.

Hill, L.G. "An experimental study of evaporation waves in a superheated liquid." PhD Thesis, California Institute of Technology, Pasadena, CA, 1991.

Jullian, S., Barreau, A., Behar, E., and Vidal, J. "Application of the SBR equation of state to high molecular weight hydrocarbons." *Chemical Engineering Science*, vol. 44, no. 4 pp. 1001-1004, 1989.

Kurschat, Th., Chaves, H. and Meier, G.E.A. "Complete adiabatic evaporation of highly superheated liquid jets." *Journal of Fluid Mechanics*, vol. 236, pp. 43-59, 1992.

Labuntsov, D.A. and Avdeev, A.A. "Mechanism of flow blockage involving shock boiling of liquid." *Teplofizika Vysokikh Temperatur*, vol. 20, no. 1, pp. 88-95, 1982.

Landau, L.D. and Lifshitz, E.M. *Fluid Mechanics*, problem 2, p. 479. Pergamon, 1959.

Lee, B.I. and Kesler, M.G. "A generalized thermodynamic correlation based on three-parameter corresponding states." *AIChE Journal*, vol. 21, no. 3, pp. 510-527, 1975.

Lienhard, J.H. and Day, J.B. "The breakup of superheated liquid jets." *Journal of Basic Engineering*, Transactions of the ASME, vol. 92, Series D, pp. 515-552, 1970.

Lienhard, J.H. and Karimi, A. "Homogeneous nucleation and the spinodal line." *Journal of Heat Transfer*, vol. 103, pp. 61-64, 1981.

Mesler, R. and Bellows, W.S. "Explosive boiling: a chain reaction involving secondary nucleation." *Proc. ASME National Heat Transfer Conference*, HTD-vol. 96, pp. 487-491, 1988.

Miller, C.A. "Stability of moving surfaces in fluid systems with heat and mass transport." *AIChE Journal*, vol. 19, no. 5, pp. 909-915, 1973.

Miyatake, O., Tomimura, Y. and Fuji, T. "An experimental study of spray flash evaporation." *Desalination*, vol. 36, pp. 113-128, 1981.

Oza, R.D. and Sinnamon, J.F. "An experimental and analytic study of flash-boiling fuel injection." SAE paper 830590, 1984.

Palmer, H.J. "The hydrodynamic stability of rapidly evaporating liquids at reduced pressure." *Journal of Fluid Mechanics*, vol. 75, part 3, pp. 487-511, 1976.

Peter, E.H., Takimoto, A. and Hayashi, Y. "Flashing and shattering phenomena of superheated liquid jets." *JSME International Journal, Series B*, vol. 37, no. 2, pp. 313-321, 1994.

Peterson, R.J., Grewal, S.S. and El-Wakil, M.M. "Investigations of liquid flashing and evaporation due to sudden depressurization." *International Journal of Heat and Mass Transfer*, vol. 27, no. 2, pp. 301-310, 1984.

Prosperetti, A. and Plesset, M. "Vapour bubble growth in a superheated liquid." *Journal of Fluid Mechanics*, vol. 85, pp. 349-369, 1978.

Prugh, R.W. "Quantify BLEVE Hazards." *Chemical Engineering Progress*, vol. 87, no. 2, pp. 66-72, 1991.

Reid, R.C., Prausnitz, J.M. and Poling, B.E. The Properties of Gases and Liquids. 4th edn., McGraw-Hill, New York, 1987.

Senda, J., Hojyo, Y. and Fujimoto, H. "Modeling of atomization process in flash boiling spray." *Fuels & Lubricants Meeting & Exposition*, Baltimore, SAE paper 941925, 1994.

Shaver, R.D., Robinson Jr., R.L., and Gasem, K.A.M. "Modified SPHCT equation of state for improved predictions of equilibrium and volumetric properties of pure fluids." *Fluid Phase Equilibria*, vol. 112, pp. 223-248, 1995.

Shaver, R.D., Robinson Jr., R.L., and Gasem, K.A.M. "Solution algorithms and parameter sensitivity analysis for the SPHCT equation of state." *Fluid Phase Equilibria*, vol. 113, pp. 61-77, 1995.

Shepherd, J.E. and Sturtevant, B. "Rapid evaporation at the superheat limit." *Journal of Fluid Mechanics*, vol. 121, pp. 379-402, 1982.

Shepherd, J.E., McCahan, S. and Cho, J. "Evaporation wave model for superheated liquids." Adiabatic Waves in Liquid-Vapor Systems. Meier, G.E.A. and Thompson, P.A. (eds.), Springer-Verlag, pp. 3-12, 1990.

Simões Moreira, J.R. "Adiabatic evaporation waves." PhD Thesis, Rensselaer Polytechnic Institute, Troy, NY, 1994.

Simoneau, R.J. "Depressurization and two-phase flow of water containing high levels of dissolved nitrogen gas." NASA Technical Paper 1839, 1981.

Sloss, C.A. "An experimental study of preheated fuel injection through a nozzle." M.A.Sc. Thesis, University of Toronto, Toronto, ON, 1996.

Soave, G.S. "A noncubic equation of state for the treatment of hydrocarbon fluids at reservoir conditions." *Industrial & Engineering Chemical Research*, vol. 34, pp. 3981-3994, 1995.

Starling, K.E., Lee, L.L. and Brule, M.R. "Predicting thermodynamic properties for fossil-fuel chemicals." *Chemical Engineering*, pp. 155-164, Nov. 1979.

Terner, E. "Shock-tube experiments involving phase changes." *Industrial & Engineering Chemistry Process Design and Development*, vol. 1, no.1, pp. 84-86, 1962.

Thompson, P.A. and Sullivan, D.A. "On the possibility of complete condensation shock waves in retrograde fluids." *Journal of Fluid Mechanics*, vol. 70, pp. 639-649, 1975.

Thompson, P.A. and Meier, G.E.A. "Real gas dynamics of fluids with high specific heat." Flow of Real Fluids. Meier, G.E.A. and Obermeier, F. (eds.), Springer-Verlag, pp. 103-114, 1985.

Thompson, P.A., Carofano, G.C. and Kim, Y. "Shock waves and phase changes in a large-heat-capacity fluid emerging from a tube." *Journal of Fluid Mechanics*, vol. 166, pp. 57-92, 1986.

Thompson, P.A., Chaves, H., Meier, G.E.A., Kim, Y. and Speckmann, H.D. "Wave splitting in a fluid of large heat capacity." *Journal of Fluid Mechanics*, vol. 185, pp. 385-414. 1987.

Thompson, P.A. Compressible-Fluid Dynamics. Rensselaer Polytechnic Institute, 1988.

Twu, C.H., Coon, J.E. and Cunningham, J.R. "An approach for the extension of a 3-parameter equation of state to heavy hydrocarbons" *Fluid Phase Equilibria*, vol. 104, pp. 83-96, 1995.

Vargaftik, N.B. Handbook of Physical Properties of Liquids and Gases, 2nd ed. Hemisphere Publishing Corporation, U.S.A., 1975.

Williams, F.A. Combustion Theory, 2nd ed. Addison-Wesley Publishing Company, Inc., 1988.

APPENDIX A: DATA FROM FLOW MODEL COMPUTATIONS

This appendix provides numerical details of the subsonic and CJ solutions computed for various metastable liquid states (1) within the solution domain shown in Figure 4.1. The figure is repeated below as Figure A.1 for reference purposes. Also included in Figure A.1 are the (1) states calculated to correspond to the experimental injections (see Figure 4.9). These (1) states lie on the curve jk .

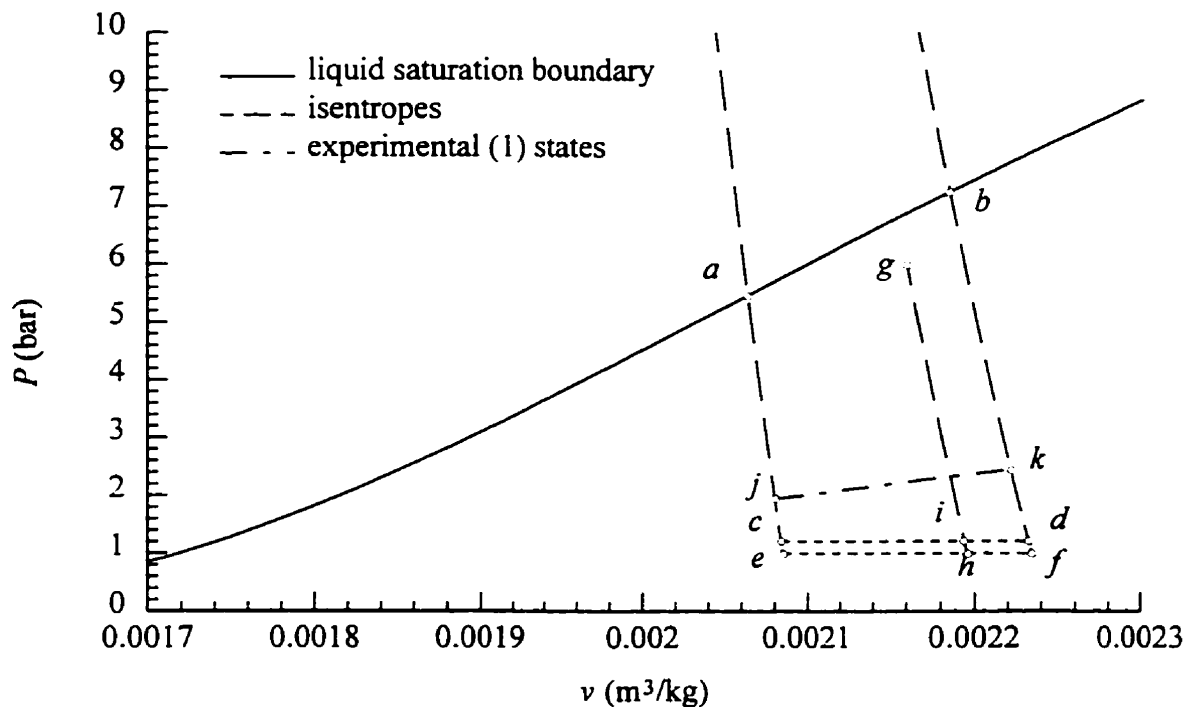


Figure A.1. Domain of possible (1) states achievable by isentropic expansion from the experimental (0) states. Region $abdc$: state (1) yields a CJ solution. Region $cdfe$: state (1) yields a subsonic solution. Curve jk : (1) states calculated using equation (4.3) and the experimental mass flow rates.

Table A.1. Subsonic solutions for (1) states lying between point h and a point just below i on the isentrope shown in Figure A.1.

State	Phase	P (bar)	T (K)	ν (m ³ /kg)	h (kJ/kg)	u (m/s)	Ja	x
0	subcooled liquid	10	590					
1 (h)	metastable liquid	1	588.74	0.002195	703.79	0	1.247	
2	superheated vapour	1	513.87	0.2383	703.79	0		
3	superheated vapour	1	513.89	0.2383				
0	subcooled liquid	10	590					
1	metastable liquid	1.05	588.75	0.002195	703.8	0.4475	1.230	
2	superheated vapour	0.946	513.27	0.2523	702.48	51.44		
3	superheated vapour	1	513.87	0.2383				
0	subcooled liquid	10	590					
1	metastable liquid	1.1	588.76	0.002195	703.81	0.6229	1.213	
2	superheated vapour	0.884	512.53	0.2705	700.86	76.78		
3	superheated vapour	1	513.88	0.2383				
0	subcooled liquid	10	590					
1	metastable liquid	1.15	588.77	0.002194	703.82	0.7490	1.196	
2	superheated vapour	0.806	511.54	0.2970	698.68	101.39		
3	superheated vapour	1	513.88	0.2383				

Table A.1. (continued)

State	Phase	P (bar)	T (K)	ν (m ³ /kg)	h (kJ/kg)	u (m/s)	Ja	x
0	subcooled liquid	10	590					
1	metastable liquid	1.2	588.78	0.002194	703.83	0.8448	1.180	
2	superheated vapour	0.677	509.68	0.3547	694.50	136.59		
3	superheated vapour	1	513.89	0.2383				
0	subcooled liquid	10	590					
1	metastable liquid	1.205	588.78	0.002194	703.83	0.8527	1.178	
2	superheated vapour	0.647	509.20	0.3714	693.41	144.37		
3	superheated vapour	1	513.89	0.2383				
0	subcooled liquid	10	590					
1	metastable liquid	1.207	588.78	0.002194	703.83	0.8557	1.178	
2	superheated vapour	0.624	508.81	0.3856	692.53	150.39		
3	superheated vapour	1	513.89	0.2383				

Table A.2. CJ solutions for (1) states lying between a point just above i and point g on the isentrope shown in Figure A.1.

State	Phase	P (bar)	T (K)	v (m ³ /kg)	h (kJ/kg)	u (m/s)	Ja	x
0	subcooled liquid	10	590					
1	metastable liquid	1.208	588.78	0.002194	703.83	0.8567	1.177	
2	superheated vapour	0.609	508.55	0.3952	691.93	154.33		
2'	superheated vapour	0.563	507.73	0.4276	690.05	166.07		
2''	superheated vapour	0.651	509.26	0.3693	693.55	143.44		
3	superheated vapour	1	513.89	0.2383				
0	subcooled liquid	10	590					
1	metastable liquid	1.25	588.78	0.002194	703.84	0.8869	1.164	
2	superheated vapour	0.630	508.60	0.3812	691.96	154.16		
2'	superheated vapour	0.422	504.42	0.5710	682.30	207.59		
2''	superheated vapour	0.759	510.90	0.3161	697.24	114.93		
3	superheated vapour	1	513.89	0.2383				
0	subcooled liquid	10	590					
1	metastable liquid	1.3	588.79	0.002193	703.86	0.9229	1.148	
2	superheated vapour	0.656	508.66	0.3658	692.00	153.96		
2'	superheated vapour	0.373	502.78	0.6457	678.41	225.60		
2''	superheated vapour	0.791	511.35	0.3029	698.25	105.84		
3	superheated vapour	1	513.89	0.2383				

Table A.2. (continued)

State	Phase	P (bar)	T (K)	ν (m ³ /kg)	h (kJ/kg)	u (m/s)	Ja	x
0	subcooled liquid	10	590					
1	metastable liquid	1.4	588.81	0.002192	703.88	0.9951	1.118	
2	superheated vapour	0.708	508.78	0.3383	692.09	153.56		
2'	superheated vapour	0.321	500.56	0.7494	673.08	248.19		
2''	superheated vapour	0.824	511.79	0.2907	699.24	96.29		
3	superheated vapour	1	513.90	0.2383				
0	subcooled liquid	10	590					
1	metastable liquid	1.8	588.87	0.002189	703.96	1.2854	1.007	
2	superheated vapour	0.916	509.26	0.2587	692.43	151.92		
2'	superheated vapour	0.238	495.29	1.0006	660.32	295.44		
2''	superheated vapour	0.872	512.44	0.2744	700.68	81.03		
3	superheated vapour	1	513.94	0.2383				
0	subcooled liquid	10	590					
1	metastable liquid	2.4	588.96	0.002185	704.10	1.7268	0.859	
2	superheated vapour	1.233	510.01	0.1890	692.94	149.35		
2'	superheated vapour	0.193	490.65	1.2243	649.08	331.71		
2''	superheated vapour	0.896	512.79	0.2667	701.49	72.25		
3	superheated vapour	1	513.99	0.2383				

Table A.2. (continued)

State	Phase	P (bar)	T (K)	v (m^3/kg)	h (kJ/kg)	u (m/s)	Ja	x
0	subcooled liquid	10	590					
1	metastable liquid	3	589.05	0.002180	704.23	2.1758	0.726	
2	superheated vapour	1.559	510.79	0.1469	693.48	146.62		
2'	superheated vapour	0.171	487.53	1.3758	641.53	354.12		
2''	superheated vapour	0.908	512.99	0.2631	701.94	67.72		
3	superheated vapour	1	514.04	0.2384				
0	subcooled liquid	10	590					
1	metastable liquid	4	589.19	0.002173	704.44	3.1278	0.524	
2	two-phase mixture	2.481	530.63	0.0755	698.55	108.65		0.82
2'	superheated vapour	0.155	484.68	1.5157	634.66	373.59		
2''	superheated vapour	0.917	513.18	0.2605	702.39	64.22		
3	superheated vapour	1	514.13	0.2384				
0	subcooled liquid	10	590					
1 (g)	metastable liquid	6	589.48	0.002160	704.88	5.9248	0.149	
2	two-phase mixture	4.540	564.17	0.0216	703.15	59.13		0.41
2'	superheated vapour	0.143	482.35	1.6352	629.06	389.45		
2''	superheated vapour	0.924	513.43	0.2588	703.00	61.65		
3	superheated vapour	1	514.30	0.2385				

Table A.3. Subsonic solutions for (1) states lying at the points *c*, *d*, *e* and *f* in Figure A.1.

State	Phase	<i>P</i> (bar)	<i>T</i> (K)	<i>v</i> (m ³ /kg)	<i>h</i> (kJ/kg)	<i>u</i> (m/s)	<i>Ja</i>	<i>x</i>
0	subcooled liquid	10	576					
1 (<i>c</i>)	metastable liquid	1.206	575.05	0.002084	656.25	0.8291	0.991	
2	superheated vapour	0.631	490.05	0.3654	645.68	145.38		
3	superheated vapour	1	495.00	0.2279				
0	subcooled liquid	10	594					
1 (<i>d</i>)	metastable liquid	1.207	592.67	0.002232	717.67	0.8655	1.232	
2	superheated vapour	0.626	514.26	0.3885	706.33	150.63		
3	superheated vapour	1	519.29	0.2412				
0	subcooled liquid	10	576					
1 (<i>e</i>)	metastable liquid	1	575.03	0.002085	656.20	0	1.064	
2	superheated vapour	1	494.98	0.2279	656.20	0		
3	superheated vapour	1	494.98	0.2279				
0	subcooled liquid	10	594					
1 (<i>f</i>)	metastable liquid	1	592.63	0.002234	717.63	0	1.301	
2	superheated vapour	1	519.27	0.2412	717.63	0		
3	superheated vapour	1	519.27	0.2412				

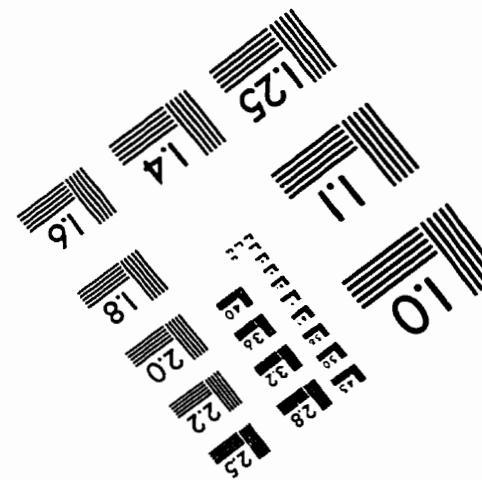
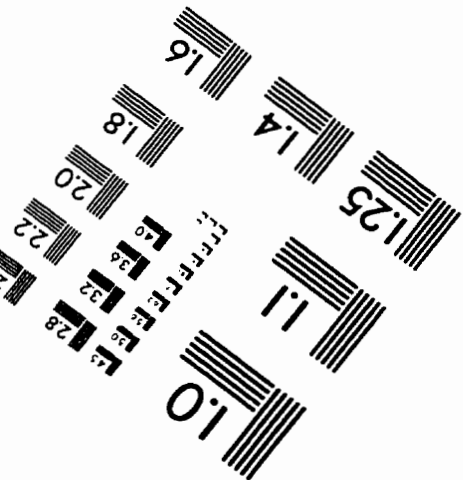
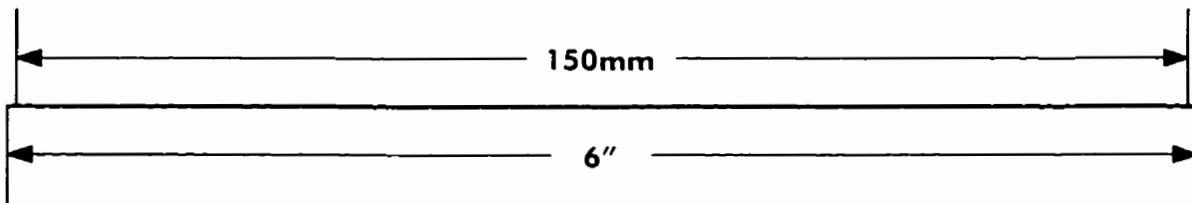
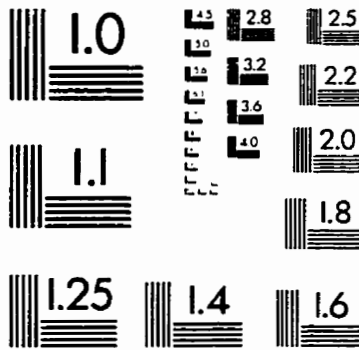
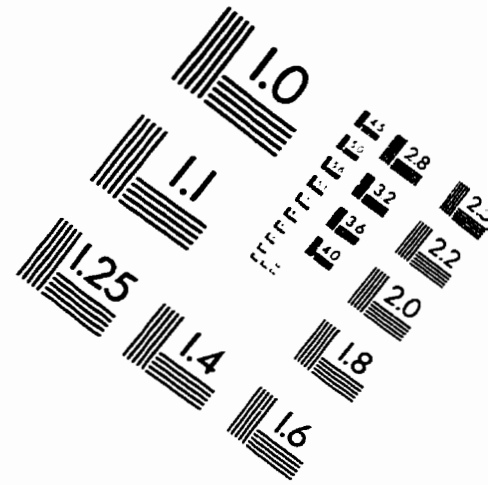
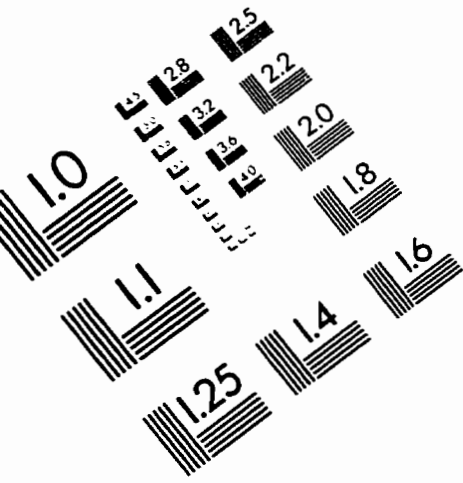
Table A.4. CJ solutions for (1) states lying along the curve jk shown in Figure A.1.

State	Phase	P (bar)	T (K)	v (m ³ /kg)	h (kJ/kg)	u (m/s)	Ja	x
0	subcooled liquid	10	576.15					
1 (j)	metastable liquid	1.941	575.28	0.002081	656.90	1.3502	0.773	
2	superheated vapour	0.993	490.86	0.2273	646.03	147.50		
2'	superheated vapour	0.225	475.46	1.019	612.06	299.47		
2''	superheated vapour	0.880	493.86	0.2603	653.98	76.49		
3	superheated vapour	1	495.26	0.2281				
0	subcooled liquid	10	580.15					
1	metastable liquid	2.045	579.24	0.002109	670.40	1.4341	0.803	
2	superheated vapour	1.047	496.37	0.2178	659.43	148.14		
2'	superheated vapour	0.216	479.96	1.0719	622.95	308.07		
2''	superheated vapour	0.885	499.33	0.2622	667.565	75.35		
3	superheated vapour	1	500.67	0.2310				
0	subcooled liquid	10	584.15					
1	metastable liquid	2.154	583.19	0.002138	684.00	1.5248	0.832	
2	superheated vapour	1.104	501.87	0.2086	672.93	148.78		
2'	superheated vapour	0.208	484.48	1.1245	633.95	316.41		
2''	superheated vapour	0.889	504.79	0.2642	681.24	74.33		
3	superheated vapour	1	506.08	0.2340				

Table A.4. (continued)

State	Phase	P (bar)	T (K)	ν (m ³ /kg)	h (kJ/kg)	u (m/s)	Ja	x
0	subcooled liquid	10	586.15					
1	metastable liquid	2.211	585.16	0.02154	690.84	1.5730	0.847	
2	superheated vapour	1.134	504.62	0.2041	679.73	149.09		
2'	superheated vapour	0.204	486.75	1.1509	639.48	320.49		
2''	superheated vapour	0.891	507.51	0.2652	688.11	73.86		
3	superheated vapour	1	508.78	0.2355				
0	subcooled liquid	10	590.15					
1	metastable liquid	2.329	589.10	0.002187	704.60	1.6745	0.878	
2	superheated vapour	1.195	510.12	0.1955	693.39	149.70		
2'	superheated vapour	0.197	491.30	1.2031	650.66	328.44		
2''	superheated vapour	0.894	512.97	0.2674	701.93	72.99		
3	superheated vapour	1	514.19	0.2385				
0	subcooled liquid	10	594.15					
1 (<i>k</i>)	metastable liquid	2.451	593.02	0.002223	718.47	1.7835	0.910	
2	superheated vapour	1.259	515.62	0.1873	707.18	150.32		
2'	superheated vapour	0.191	495.88	1.2549	661.98	336.13		
2''	superheated vapour	0.898	518.42	0.2696	715.87	72.22		
3	superheated vapour	1	519.60	0.2414				

IMAGE EVALUATION TEST TARGET (QA-3)



APPLIED IMAGE, Inc
 1653 East Main Street
 Rochester, NY 14609 USA
 Phone: 716/482-0300
 Fax: 716/288-5989

© 1993, Applied Image, Inc., All Rights Reserved